FACULTY OF ELECTRICAL ENGINEERING AND COMMUNICATION
department of radio electronics

EM FIELD CHARACTERIZATION OF PLANAR CIRCUITS: AN APPROACH BASED ON THE TIME-DOMAIN CONTOUR INTEGRAL METHOD

HABILITATION THESIS
HABILITAČNÍ PRÁCE

AUTHOR
AUTOR PRÁCE

MARTIN ŠTUMPF

CZECH REPUBLIC, BRNO 2017

Acknowledgments

In the first place I wish to express my thanks to Professor Adrianus T. de Hoop for many stimulating discussions and critical remarks, which, as I strongly believe, improved the quality of the thesis.

Further I desire to thank Professor Guy A. E. Vandenbosch for his continuous encouragement and valuable advices that help me to carry on with my research.

Finally I wish to thank Professor Zbyněk Raida for giving me the opportunity to develop my master thesis at the Institute for Fundamental Electrical Engineering and ElectroMagnetic Compatibility (IGET), Otto-von-Guericke University Magdeburg, where I got acquainted with EMC applications of the contour integral method. The latter would not be possible without the professional scientific supervision of Professor Marco Leone who has drawn my attention to this numerical method and to the field of EMC as a whole.

Much of the research work included in this thesis has received funding from the Czech Ministry of Education, Youth and Sports under project LD15005 of the COST CZ (LD) program and under grant LO1401 of the National Sustainability Program. The author takes this opportunity to gratefully acknowledge this financial support.

Preface

This thesis is intended to provide an introductory account of the time-domain contour integral method and its applications to the time-domain electromagnetic analysis of planar structures. The work is largely based on the contents of the following papers:

- M. Štumpf. The time-domain contour integral method – an approach to the analysis of double-plane circuits. *IEEE Transactions on Electromagnetic Compatibility*, vol. 56, no. 2, pp. 367–374, Apr. 2014.
- M. Štumpf. Analysis of dispersive power-ground structures using the time-domain contour integral method. *IEEE Transactions on Electromagnetic Compatibility*, vol. 57, no . 2, pp. 224–231, Apr. 2015.
- M. Štumpf. Modeling of electromagnetic fields in parallel-plane structures: a unified contour-integral approach. *Radioengineering*, [**invited**], Apr. 2017.
- M. Štumpf. Pulsed EM field radiation, mutual coupling, and reciprocity of thin planar antennas. *IEEE Transactions on Antennas and Propagation*, vol. 62, no. 8, pp. 3943–3950, Aug. 2014.
- M. Štumpf. Time-domain analysis of rectangular power-ground structures with relaxation. *IEEE Transactions on Electromagnetic Compatibility*, vol. 56, no. 5, pp. 1095–1102, Oct. 2014
- M. Štumpf. The pulsed EM plane-wave response of a thin planar antenna. *Journal of Electromagnetic Waves and Applications*, vol. 30, no. 9, pp. 1133–1146, May 2016.
- M. Štumpf. Time-domain mutual coupling between power-ground structures. In *Proceedings 2014 IEEE International Symposium on Electromagnetic Compatibility*. Raleigh, (NC, USA), 3–8 August 2014, pp. 240–243.
- M. Štumpf. The equivalent Thévenin-network representation of a pulse-excited power-ground structure. *IEEE Transactions on Electromagnetic Compatibility*, vol. 59, no. 1, pp. 249–255, Feb. 2017.

In order to translate this material to a coherent story, the papers have been supplemented with several new sections and appendices.

Contents

Acronyms

CIM Contour-Integral Method

EM ElectroMagnetic

EMC ElectroMagnetic Compatibility

EMI ElectroMagnetic Interference

FD Frequency Domain

FIT Finite-Integration Technique

MOT Marching-On in Time

PCB Printed-Circuit Board

PCBs Printed-Circuit Boards

PEC Perfect Electric Conductor

PMC Perfect Magnetic Conductor

TD Time Domain

TD-CIM Time-Domain Contour-Integral Method

UWB Ultra Wide Band

Chapter 1

Introduction

With the still increasing data rates on high-speed digital interconnection structures, two major concerns can be distinguished. At first, the need for low-cost engineering design calls for efficient modeling methodologies that enable a proper (i.e. space-time) ElectroMagnetic (EM) characterization of such structures. Secondly, the aspect of particular importance is the EM interference analysis that secure such systems' proper performance as well as smooth co-existence complying with the international regulations on ElectroMagnetic Interference (EMI).

A widely used building block of modern high-speed multilayered Printed-Circuit Boards (PCBs) and planar antennas is based on the parallel-plane structure. Since the pulsed-field characteristics of such a structure play the crucial role in the overall system behavior, TD analysis of its EM transmission and radiation properties is the main subject of this thesis. A conventional numerical method capable of analyzing planar circuits in the Frequency Domain (FD) is known as the Contour-Integral Method (CIM). The CIM was pioneered by Okoshi and Miyoshi for solving various problems in microwave engineering [69]. Since its introduction at the beginning of the 1970's, the method has been successfully applied to FD modeling of planar circuits [61, 62, 67, 68, 70], microstrip antennas [35, Sec. 9.3.3] and waveguiding structures [43, 84]. The main advantages of CIM lie in its low computational demands and high versatility enabling the straightforward handling of arbitrarily-shaped planar circuits and embedding of additional circuit elements. Accordingly, CIM is still preferable in numerical modeling and optimization of complex systems where full-wave electromagnetic solvers would require exceedingly high computational resources [28, 115].

Despite the still increasing interest in TD modeling of high-speed VLSI interconnects [2, 81], signal integrity issues on PCBs [3, 26] or UWB antennas [30], the corresponding *time-domain* CIM has not been described in a coher-

ent manner so far. The main purpose of this thesis, therefore, is to fill this gap and provide a unified description of the Time-Domain Contour-Integral Method (TD-CIM) (see [108]), with its applications to signal-transfer and EM interference analysis.

The standard CIM is based on the so-called cavity model [51]. Owing to its simplicity, it has been widely used at the time of onset of microstrip circuits and rendered many valuable insights into their transmission as well as radiation EM behavior. The cavity model is based on the assumption that the EM field within the microstrip structure does not vary across the dielectric slab and is fully confined within the structure enclosed with a vanishing tangential magnetic field along its rim (magnetic wall). The vertical component of the electric field is then taken into account only and the analysis is reduced to solving a two-dimensional boundary value problem that admits the closed-form eigenfunction expansion for simple shapes of the planar circuit [12, Sec. 4.14]. The assumption of the perfect-magnetic wall breaks down once the height of the circuit becomes comparable to the wavelength. In such a case the effects as fringing fields or/and surface waves (if exist) may gain in significant importance and one has to resort to a full-wave technique [59]. Although the cavity model as such does not radiate any energy, radiation losses may be accounted for by introducing the equivalent dielectric loss or by imposing impedance boundary conditions along the circuit periphery [34, Sec. 2.3].

The history of CIM traces back to the 1960's and its developments are associated especially with the field of acoustics. The early origins are connected with the solution of static potential problems described in papers of Jaswon [41] and Symm [93] and later introduced by Harrington et al. [37] in electrostatics. As far as time-dependent problems are concerned, three basic approaches may be distinguished:

- Time-stepping methods based on the finite-difference approximation of time derivatives;
- Integral-transform methods based on the Laplace or Fourier transform;
- Direct methods based on the time-dependent fundamental solution.

The first attempts to solve the time-dependent integral-equation formulations numerically are connected with the time-stepping approach and can be found in works of Friedman and Shaw [32] and Bennett and Weeks [7] for acoustics and electromagnetics, respectively. In their approach, a discretized integral equation (or a system of integral equations) is converted into a system of algebraic equations that is solved in an step-by-step updating manner known

as the Marching-On in Time (MOT) method. The time-stepping approach uses finite-difference approximations of pertaining time derivatives. Beside others, the most popular time-integration schemes are based on the Newmark, Houbolt or Wilson θ methods [95]. Although the MOT method may suffer from serious instabilities [99, Sec. 13.3], it has become popular for tackling the transient scattering problems and its development is still in progress (see [79], for example). The stability issues have been later avoided with the aid of conjugate-gradient approaches [85, 104] and the relaxation method [98, Chapter 3], but at the expense of higher computational demands.

The second class of numerical approaches leans heavily on the application of integral transforms with respect to time. The pioneering works employing the Laplace transform are those of Cruse and Rizzo [14, 15]. One of the main disadvantages of the transform-based methods is the need for the proper choice of parameters required by inversion techniques [29, Sec. 4.2]. The corresponding integral-equation methods based on the Fourier transform can be found in [66, 96], for instance. A formulation of the direct TD integral equation method for both 2D and 3D relaxation-free scalar wave equations has been proposed by Mansur and Brebia [53, 54]. In these initial studies, a TD weighted-residual form is the starting point for a numerical solution. More recent approaches are based on the convolution quadrature method [86] or on the symmetric Galerkin procedure [9]. For a detailed historical survey of the subject we refer the reader to the book of Dominguez [27].

The formulation of TD-CIM as formulated in this thesis is based on the reciprocity theorem of the time-convolution type [20, Sec. 28]. In the reciprocity theorem, one of the EM-field states represents the 'actual' state while the second one is the 'testing' (or 'computational') state. The problem formulation can be then envisaged as a 'weak' form of the corresponding boundary-value problem. In contrast to the three-dimensional integral-equation formulations that require discretization of the entire surface of a conducting surface [59], the CIM accounts for only its rim, which considerably reduces the solution space. On top of this, the corresponding space-time fundamental solution is known in closed (or semi-closed) form, which avoids the elaborate numerical evaluation of inverse-Fourier integrals [60, Chapter 8]. On the other hand, the applicability of TD-CIM is limited and lies in the range where the circuit's thickness is small with respect to the spatial support of the excitation pulse. The proposed TD-CIM may therefore find its wide applications in the fast modeling of pulse-shaped signal transfers via parallel-plane structures, in the TD analysis of arbitrarily-shaped planar circuits and antennas and in handling of related signal/power integrity and EMI issues.

1.1 Synopsis

In Chapter 2 a cavity model a planar circuit is described in terms of an initial-boundary value formulation and a reciprocity-based integral relation. The both formulations are applied throughout the thesis to modeling the pulsed-signal transfer over planar circuits. The final section describes the incorporation of an excitation port in the reciprocity-based integral-equation formulation. This part is supplemented with Appendix A where the relevant Green-function spatial singularities are handled analytically.

Chapter 3 describes a computational method for solving the reciprocity-integral relation for the case of a loss-free, instantaneously-reacting planar circuit. In order to validate TD-CIM-based numerical results, closed-form analytical expressions are derived for a rectangular circuit. A demo MATLAB® implementation of the introduced method is briefly given in Appendix B. Finally, the results are shown to agree very well with the ones evaluated using the (three-dimensional) Finite-Integration Technique (FIT).

The relation of the classic real-FD CIM formulation and the reciprocity relation from Chapter 3 is revealed in Chapter 4. In this chapter, two CIM-based numerical schemes are discussed. Namely, it is shown that the classic point-matching solution can be also interpreted as a special case of the pulse-matching solution to which the 1-point Gaussian quadrature is applied. Accuracy of sample numerical results is briefly discussed with the help of a closed-form analytical formula pertaining to a rectangular planar circuit.

A topic of special importance in signal integrity on high-speed PCBs is the incorporation of dissipation and relaxation mechanisms. A semi-analytical technique for TD analysis of rectangular planar circuits with relaxation is hence introduced in Chapter 5. The technique is based on a ray-like expansion and heavily leans on the numerical inversion of the Laplace transformation as detailed in Appendix G. The latter makes possible to account for general relaxation behavior. The relation of the ray-type and the standard eigenfunction expansions is discussed. Numerical results are evaluated for two types of the dielectric relaxation function and validated, again, with the help of FIT.

In Chapter 6 the incorporation of relaxation behavior in TD-CIM is investigated. Again, the proposed approach makes use of the numerical Laplace-transform inversion introduced in Appendix G. The extension in this direction thus enables us to analyze arbitrarily-shaped planar circuits showing general relaxation behavior. All the obtained results are compared with the corresponding ones evaluated using the FIT.

In order to analyze radiation properties of microstrip antennas or EMI issues related to PCBs, the pulsed radiation characteristics of arbitrarily-

shaped planar circuits are studied in Chapter 7. The comparison of TD-CIM-based and FIT-based results shows that TD-CIM may serve the purpose very well.

In Chapter 8 the computational model for efficient analysis of TD EM mutual coupling between arbitrarily-shaped planar circuits is developed with the aid of the reciprocity theorem of the time-convolution type. The interaction model makes possible to evaluate the induced pulsed-voltage response of a receiving planar circuit due to the impulsive electric-current excitation applied to a transmitting planar circuit. Sample numerical results show the considerable reduction of computational demands with respect to the referential FIT.

The reciprocity theorem of the time-convolution type can also be applied to link the pulsed EM radiation characteristics to the circuit's pulsed-voltage response to a plane wave while operating in the receiving state. This is exactly demonstrated in Chapter 9, where the relevant self-reciprocity relation concerning a general planar circuit is derived. In this chapter it is demonstrated that such a relation can be very useful for benchmarking numerical EM solvers.

The reciprocity analysis is further generalized to the N-port case in Chapter 10. In this chapter it is shown that the systematic use of the reciprocity theorem leads to the Kirchhoff-type network representation of an N-port planar circuit. The equivalent Thévenin circuit of a 2-port planar circuit is then discussed in detail. An application of the equivalent-circuit representation is finally demonstrated on sample numerical calculations of the pulsed EM radiation characteristics of a 2-port planar circuit using TD-CIM and FIT.

Chapter 11 introduces reciprocity-based closed-form expressions for the evaluation of pulsed EM-field radiated susceptibility concerning a planar circuit. Specifically, the derived relations express the pulsed voltage response of a planar structure to an external impulsive EM plane wave via a one-dimensional contour integral. In addition to the high computational efficiency of the introduced approach, the derived TD integral representations provide physical insights into the dominant (space-time) EM-coupling mechanism. Again, the formulated computational model is validated with the aid of the referential FIT.

1.2 Basic conventions

The localize a point in a Cartesian space $\mathbb{R}^3$, the orthogonal right-handed Cartesian reference frame is employed. The spatial reference frame is defined with respect to the origin O and the three mutually perpendicular base

vectors $\{\boldsymbol{i}_1, \boldsymbol{i}_2, \boldsymbol{i}_3\}$ of unit length each; they form in the indicated order, a right-handed system. The position vector is $\boldsymbol{x} = x_1\boldsymbol{i}_1 + x_2\boldsymbol{i}_2 + x_3\boldsymbol{i}_3$. The time coordinate is denoted by t.

Except for the chapters where the three-dimensional radiation characteristics and reciprocity come into the play (e.g. Ch. 7, 8, 9 and 11), the EM field quantities in the problem configurations are independent along the vertical direction $\boldsymbol{i}_3$. As a consequence, it is convenient to decompose all field quantities along the horizontal plane (parallel with respect to $x_3 = 0$) and along the vertical direction. Then all symbols associated with the two-dimensional Cartesian vectors with respect to $\{\boldsymbol{i}_1, \boldsymbol{i}_2\}$ are typeset in bold-face Romain or bold-face Greek. The corresponding position vector, for example, then just reads

$$\boldsymbol{x} = x_1\boldsymbol{i}_1 + x_2\boldsymbol{i}_2 \tag{1.1}$$

Throughout the thesis, light-faced Roman or Greek symbols stand for scalars. Latin and Greek subscripts stand for $\{1, 2, 3\}$ and $\{1, 2\}$, respectively. The spatial differentiation with respect to x_m is denoted as ∂_m for each $m = \{1, 2, 3\}$. For example, let $\boldsymbol{\kappa}$ be a Cartesian vector which is differentiable with respect spatial coordinates x_m. Then κ_μ denotes a component of $\boldsymbol{\kappa}$ for each $\mu = \{1, 2\}$, whose derivatives with spatial coordinates $\partial_m\boldsymbol{\kappa}$ are again vector functions with components $\partial_m\kappa_\mu$. The only exceptions are ∂_t that is reserved for the partial differentiation with respect to time and ∂_ν that denotes the directional derivative along $\boldsymbol{\nu}$. The dot product and the cross product of two vectors are denoted by $\cdot$ and $\times$, respectively.

All investigated problem configurations are supposed to be time invariant. To tackle such problems we preferably apply the *one-sided Laplace transformation* with respect to time accounting for the property of causality. The one-sided Laplace transformation of some bounded physical quantity is defined as

$$\hat{u}(\boldsymbol{x}, s) = \int_{t=0}^{\infty} \exp(-st)u(\boldsymbol{x}, t)\mathrm{d}t \tag{1.2}$$

with $u(\boldsymbol{x}, t) = 0$ for $t < 0$. Here, the transformation parameter $s \in \mathbb{C}$ (complex frequency) is chosen to have a positive real part, large enough to ensure the convergence of the Laplace integral. The corresponding time convolution of two transient space-time functions $u_1 = u_1(\boldsymbol{x}, t)$ and $u_2 = u_2(\boldsymbol{x}, t)$ defined on $t \in \mathbb{R}$ is given as

$$\begin{aligned}(u_1 * u_2)(\boldsymbol{x}, t) &= \int_{\tau\in\mathbb{R}} u_1(\boldsymbol{x}, \tau)u_2(\boldsymbol{x}, t-\tau)\mathrm{d}\tau \\ &= \int_{\tau\in\mathbb{R}} u_1(\boldsymbol{x}, t-\tau)u_2(\boldsymbol{x}, \tau)\mathrm{d}\tau = (u_2 * u_1)(\boldsymbol{x}, t)\end{aligned} \tag{1.3}$$

which shows the commutative properties of the time convolution. Other basic properties of the convolution are (1) linearity; (2) associative property; (3) distributive property. Applying the Laplace transformation to Eq. (1.3) yields the *convolution theorem*

$$(u_1 * u_2)(\boldsymbol{x}, t) = \mathcal{L}^{-1}[\hat{u}_1(\boldsymbol{x}, s)\hat{u}_2(\boldsymbol{x}, s)] \tag{1.4}$$

where the symbol $\mathcal{L}^{-1}(.)$ represents the inverse Laplace transformation. The convolution theorem only makes sense if there exists a strip in the complex s-plane in which the definition integrals for $\hat{u}_1(\boldsymbol{x}, s)$ and $\hat{u}_2(\boldsymbol{x}, s)$ converge simultaneously [20, Appendix B]. Finally, the time integration operator is defined as

$$\mathbf{I}_t\, u(\boldsymbol{x}, t) = \int_{\tau=-\infty}^{t} u(\boldsymbol{x}, \tau)\mathrm{d}\tau \tag{1.5}$$

All EM quantities are, in accordance with the international conventions, expressed in SI units (The International System of Units) [20, General Introduction].

Chapter 2

Basic formulation

The main purpose of this chapter is to present two basic formulations for TD modeling of thin planar circuits. Namely, we describe a boundary-value formulation with the corresponding eigenfunction expansion and an integral-equation formulation based on the reciprocity theorem of the time-convolution type. As will become clear later, the former formulation is useful for validation purposes while the latter serves as the point of departure for TD-CIM.

In accordance with the definition given by Okoshi [67, Sec. 1.1.4], the planar circuit is defined here as a parallel-plane circuit whose thickness is negligible with respect to the spatial support of the excitation pulse. It is shown that under this condition, the excited EM field does not vary across the slab and the problem boils down to solving the (transverse magnetic) set of EM-field equations. The field equations, supplemented with the relevant boundary, initial and causality conditions, are then solved on a bounded surface domain. The problem may be thus formulated as an initial-boundary value problem and solved, when possible, with the help of conventional methods such as the separation of variable technique or the method of images. Unfortunately, application of these methods is very limited and allows to analyze circuits of elementary shapes only such as rectangles, circles and triangles, for instance. A way to circumvent this limitation is to approach the problem via the contour-integral formulation based on the reciprocity theorem of the time-convolution type. Computational implementations of the latter formulation is exactly the main purpose of this thesis.

The present chapter is organized as follows. At first, the EM field equations together with the accompanying boundary and initial conditions are introduced. Secondly, the complex-frequency domain boundary value problem is formulated and solved in Sec. 2.1.1. Here, the solution is written out in terms of the classical eigenfunction expansion also known as the double-

summation formula. In this section we define the transmission impedance – a parameter that turns out to be proportional to a double integral of the relevant fundamental solution. Subsequently, the reciprocity-based integral-equation formulation is introduced in Sec. 2.1.2. Its relation with the boundary-value formulation is briefly sketched in the following Sec. 2.1.3. Finally, modeling strategies concerning the embedding of excitation ports is described in Sec. 2.1.4.

2.1 2D model of a planar circuit

We shall analyze the planar circuit shown in Fig. 2.1. Such a planar structure consists of a homogeneous layer that is sandwiched between two PEC planes of vanishing thickness, i.e. the upper plane (also called as the power plane or the patch) Ω and the bottom plane (or the ground plane). The EM properties of the slab are specified by its (Boltzmann-type) dielectric relaxation function $\kappa = \kappa(t)$ and magnetic permeability $\mu = \mu_0$. Its thickness is d. The dielectric relaxation function is supposed to be causal in its EM behavior. In the case of an instantaneously reacting slab the dielectric relaxation function is impulsive, i.e. $\kappa(t) = \epsilon\delta(t)$, and is proportional to electric permittivity ϵ. The corresponding EM wave speed is then $c = (\epsilon\mu)^{-1/2} > 0$. The structure is activated by a prescribed electric-current surface density along a section of circuit's periphery $\partial\Omega$ (i.e. boundary contour) or/and by a vertical electric-current density injected into the conducting patch Ω.

To arrive at EM field equations describing the *actual* field within the planar circuit under the thin-slab approximation we write the field quantities in their Taylor expansions around $x_3 = 0$. After retaining only the lowest-order (x_3-independent) terms we end up with the transverse-magnetic (with

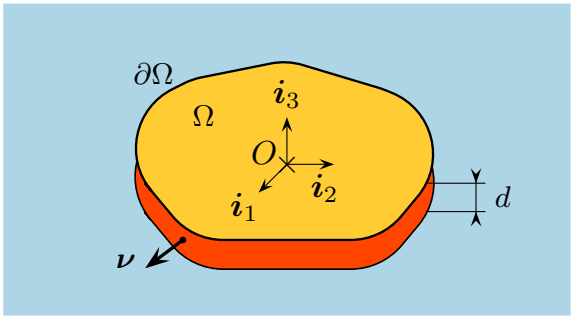

Figure 2.1: Planar circuit. Taken from [108], with permission from IEEE, © 2014 IEEE.

respect to x_3) system of equations, i.e.

$$-\partial_1 H_2 + \partial_2 H_1 + \kappa * \partial_t E_3 = -J_3 \tag{2.1}$$

$$\partial_2 E_3 + \mu \partial_t H_1 = 0 \tag{2.2}$$

$$-\partial_1 E_3 + \mu \partial_t H_2 = 0 \tag{2.3}$$

for $\boldsymbol{x} \in \Omega$ and $t > 0$. The initial values of the EM field components are assumed to be zero

$$\{E_3, \boldsymbol{H}\}(\boldsymbol{x}, 0) = \{0, \boldsymbol{0}\} \tag{2.4}$$

for all $\boldsymbol{x} \in \Omega \cup \partial\Omega$. Along the circuit periphery we may prescribe the excitation electric-current surface density via the boundary-excitation condition

$$(\boldsymbol{i}_3 \times \boldsymbol{\nu}) \cdot \boldsymbol{H}(\boldsymbol{x} + \delta\boldsymbol{\nu}, t) = \boldsymbol{\nu}(\boldsymbol{x}) \cdot \partial\boldsymbol{J}(\boldsymbol{x} + \delta\boldsymbol{\nu}, t) \quad \text{as } \delta \downarrow 0 \tag{2.5}$$

for all $\boldsymbol{x} \in \partial\mathcal{S}$ and $t > 0$. Here, $\mathrm{supp}[\partial\boldsymbol{J}(\boldsymbol{x}, t)] = \partial\mathcal{S} \subset \partial\Omega$ and $\boldsymbol{\nu}$ is the unit vector normal to $\partial\Omega$ pointing away from Ω. The classical resonator model assumes the vanishing tangential magnetic field along a source-free part of the (magnetic-wall) boundary

$$(\boldsymbol{i}_3 \times \boldsymbol{\nu}) \cdot \boldsymbol{H}(\boldsymbol{x} + \delta\boldsymbol{\nu}, t) = 0 \quad \text{as } \delta \downarrow 0 \tag{2.6}$$

for all $\boldsymbol{x} \in \partial\Omega/\partial\mathcal{S}$ and $t > 0$. Equations (2.1)–(2.6) constitute an initial-boundary value problem whose solution is the main subject of the following chapters. In the vertical electric current density J_3 introduced in Eq. (2.1) we may distinguish between the external (or active) part describing the action of the source port and the induced (or passive) part describing the current flowing through an element connected between the PEC plates of the circuit. The latter can be viewed as an equivalent contrast-source volume density producing the scattered field and is hence field-dependent.

The system of field equations (2.1)–(2.6) represent the starting point for developments that follow. Namely, we shall further distinguish between a boundary-value and a CIM formulation. While the latter will serve for modeling of arbitrarily-shaped planar circuits, the former formulation will become useful for analytical description of planar circuits having a simple shape (e.g. rectangular circuit).

2.1.1 Boundary-value formulation

Let us consider the planar structure with the perfect open boundary (cf. Eq. (2.6)) that is excited by the vertical electric-current volume density J_3.

Upon applying the Laplace transformation to Eqs. (2.1)–(2.3) with (2.4) and (2.6) we may formulate the following boundary-value problem, i.e.

$$(\partial_1^2 + \partial_2^2 - \hat{\gamma}^2)\hat{E}_3 = s\mu\hat{J}_3 \quad \text{in } \Omega \tag{2.7}$$

$$\partial_\nu \hat{E}_3 = 0 \quad \text{on } \partial\Omega \tag{2.8}$$

where $\hat{\gamma} = \hat{\gamma}(s)$ is the propagation coefficient that is equal to $\hat{\gamma} = s/c$ for an instantaneously-reacting, loss-free planar circuit. Recall that ∂_ν denotes the directional derivative taken along the normal vector $\boldsymbol{\nu}$ (see Sec. 1.2). The problem can be solved using Green's function that satisfies the same boundary condition along $\partial\Omega$ as the unknown electric field strength, i.e.

$$(\partial_1^2 + \partial_2^2 - \hat{\gamma}^2)\hat{G} = -\delta(\boldsymbol{x} - \boldsymbol{x}^S) \quad \text{in } \Omega \tag{2.9}$$

$$\partial_\nu \hat{G} = 0 \quad \text{on } \partial\Omega \tag{2.10}$$

which implies the linear relation between the source and the vertical electric field

$$\hat{E}_3(\boldsymbol{x}^S, s) = -s\mu \int_{\boldsymbol{x}\in\Omega^S} \hat{G}(\boldsymbol{x}|\boldsymbol{x}^S, s)\hat{J}_3(\boldsymbol{x}, s)\mathrm{d}A(\boldsymbol{x}) \tag{2.11}$$

for $\boldsymbol{x}^S \in \Omega$, $\Omega^S = \mathrm{supp}(\hat{J}_3) \subset \Omega$. The introduced Green's function can be represented using (a complete set of) eigenfunctions that satisfy

$$(\partial_1^2 + \partial_2^2 + k_{mn}^2)\psi_{mn} = 0 \quad \text{in } \Omega \tag{2.12}$$

$$\partial_\nu \psi_{mn} = 0 \quad \text{on } \partial\Omega \tag{2.13}$$

It can be shown that for (2.12)–(2.13) the eigenvalues k_{mn}^2 are always real-valued, the corresponding eigenfunctions can be normalized to satisfy the orthonormality condition

$$\int_{\boldsymbol{x}\in\Omega} \psi_{mp}\psi_{nq}\mathrm{d}A(\boldsymbol{x}) = \delta_{m,n}\delta_{p,q} \tag{2.14}$$

and form a complete set enabling us to expand the Green's function in a series

$$\hat{G}(\boldsymbol{x}|\boldsymbol{x}^S, s) = \sum_{m,n} \hat{A}_{mn}(s)\psi_{mn}(\boldsymbol{x}) \tag{2.15}$$

The expansion coefficients are found upon substituting Eq. (2.15) in Eq. (2.9) and integrating the result multiplied by ψ_{pq} over Ω. Taking into account the orthonormality condition we finally arrive at

$$\hat{G}(\boldsymbol{x}|\boldsymbol{x}^S, s) = \sum_{m,n} \frac{\psi_{mn}(\boldsymbol{x})\psi_{mn}(\boldsymbol{x}^S)}{\hat{\gamma}^2 + k_{mn}^2} \tag{2.16}$$

The Green-function method may be applied to describe pulsed EM transmission between source and receiver ports of a planar circuit. To this end, the electric current applied to the excitation port is written as

$$\hat{I}(s) = \int_{\boldsymbol{x}\in\Omega^S} \hat{J}_3(\boldsymbol{x}, s)\mathrm{d}A(\boldsymbol{x}) \tag{2.17}$$

where Ω^S is the domain occupied by the excitation port. Similarly, the probed voltage at the receiving port is expressed as

$$\hat{V}(s) = -\frac{d}{|\Omega^P|}\int_{\boldsymbol{x}\in\Omega^P} \hat{E}_3(\boldsymbol{x}, s)\mathrm{d}A(\boldsymbol{x}) \tag{2.18}$$

where Ω^P is the domain occupied by the receiving port and $|\Omega^P|$ denotes its surface area. Consequently, the probed voltage $\hat{V}(s)$ can be related to the electric-current density according to

$$\hat{V}(s) = \frac{s\mu d}{|\Omega^P|}\int_{\boldsymbol{x}^S\in\Omega^P} \mathrm{d}A(\boldsymbol{x}^S)\int_{\boldsymbol{x}\in\Omega^S} \hat{G}(\boldsymbol{x}|\boldsymbol{x}^S, s)\hat{J}_3(\boldsymbol{x}, s)\mathrm{d}A(\boldsymbol{x}) \tag{2.19}$$

from which the s-domain transfer impedance follows, i.e.

$$\hat{Z}(s) = \frac{\hat{V}(s)}{\hat{I}(s)} = \frac{s\mu d}{|\Omega^P|\cdot|\Omega^S|}\int_{\boldsymbol{x}^S\in\Omega^P} \mathrm{d}A(\boldsymbol{x}^S)\int_{\boldsymbol{x}\in\Omega^S} \hat{G}(\boldsymbol{x}|\boldsymbol{x}^S, s)\mathrm{d}A(\boldsymbol{x}) \tag{2.20}$$

where we have assumed the constant distribution of the source electric-current density over the surface of the port. For a number of special cases eigenfunctions ψ_{mn} and hence the integration in Eq. (2.20) admit analytical representations. Finally, the pulsed voltage at $\boldsymbol{x}\in\Omega^P$ due to the action of the source at $\boldsymbol{x}\in\Omega^S$ follows from the time convolution of the excitation electric-current pulse with the TD counterpart of the transmission impedance, i.e.

$$\mathcal{V}(t) = \mathcal{Z}(t) * \mathcal{I}(t) \tag{2.21}$$

The time convolution can be for special cases calculated analytically, which will later serve for the validation of TD-CIM introduced in Chapter 3.

2.1.2 Reciprocity-based integral formulation

As the point of departure for the transient analysis of arbitrarily-shaped planar circuits we take the reciprocity theorem of the time-convolution type [20, Sec. 28.2]. For later convenience we further proceed with our analysis in the complex-FD (see Sec. 1.2). Then taking into the account the zero

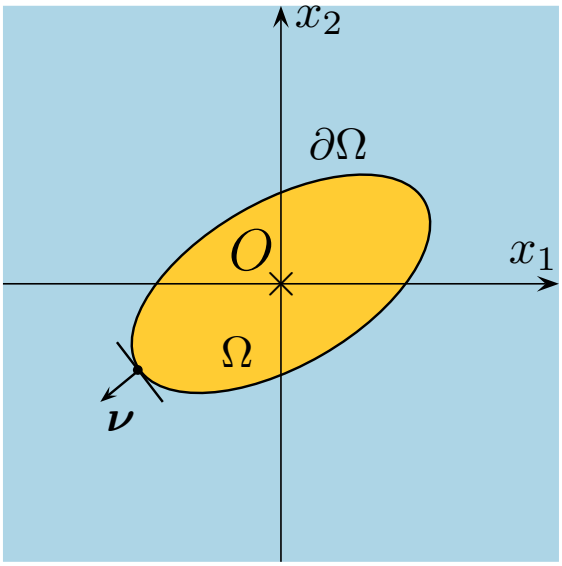

Figure 2.2: Bounded domain to which the reciprocity theorem is applied.

initial conditions (2.4), the actual wave field satisfies the (complex-FD) field equations (cf. Eqs. (2.1)–(2.3))

$$-\partial_1 \hat{H}_2 + \partial_2 \hat{H}_1 + s\hat{\epsilon}\hat{E}_3 = -\hat{J}_3 \tag{2.22}$$

$$\partial_2 \hat{E}_3 + s\mu\hat{H}_1 = 0 \tag{2.23}$$

$$-\partial_1 \hat{E}_3 + s\mu\hat{H}_2 = 0 \tag{2.24}$$

for all $\boldsymbol{x} \in \Omega$. To arrive at a weak formulation of the formulated problem, let us consider a causal *testing* (B) wave field that satisfies the following complex-FD equations

$$-\partial_1 \hat{H}_2^B + \partial_2 \hat{H}_1^B + s\hat{\epsilon}\hat{E}_3^B = -\hat{J}_3^B \tag{2.25}$$

$$\partial_2 \hat{E}_3^B + s\mu\hat{H}_1^B = 0 \tag{2.26}$$

$$-\partial_1 \hat{E}_3^B + s\mu\hat{H}_2^B = 0 \tag{2.27}$$

for all $\boldsymbol{x} \in \mathbb{R}^2$. Note that the contrast in the EM properties between the both states is assumed to be zero and the condition of causality is replaced by the requirement of boundedness along the 'sphere at infinity'. Upon combining Eqs. (2.22)–(2.24) with Eqs. (2.25)–(2.27) we then arrive at the *local interaction quantity*

$$\partial_1 \left(\hat{E}_3 \hat{H}_2^B - \hat{E}_3^B \hat{H}_2 \right) - \partial_2 \left(\hat{E}_3 \hat{H}_1^B - \hat{E}_3^B \hat{H}_1 \right) = \hat{E}_3 \hat{J}_3^B - \hat{E}_3^B \hat{J}_3 \tag{2.28}$$

$\boldsymbol{x} \in \Omega$. In the next step the local interaction quantity is integrated over the surface of the patch Ω (see Fig. 2.2) and with the aid of Gauss' theorem its *global form* is found

$$\begin{aligned}
&\chi_\Omega(\boldsymbol{x}^S) \int_{\boldsymbol{x}\in\Omega} \hat{E}_3(\boldsymbol{x}, s)\hat{J}_3^B(\boldsymbol{x}|\boldsymbol{x}^S, s)\mathrm{d}A(\boldsymbol{x}) \\
&\qquad - \int_{\boldsymbol{x}\in\partial\Omega} \hat{E}_3(\boldsymbol{x}, s)\boldsymbol{\nu}(\boldsymbol{x}) \cdot \partial\hat{\boldsymbol{J}}^B(\boldsymbol{x}|\boldsymbol{x}^S, s)\mathrm{d}l(\boldsymbol{x}) \\
&= \int_{\boldsymbol{x}\in\Omega} \hat{E}_3^B(\boldsymbol{x}|\boldsymbol{x}^S, s)\hat{J}_3(\boldsymbol{x}, s)\mathrm{d}A(\boldsymbol{x}) \\
&\qquad - \int_{\boldsymbol{x}\in\partial\Omega} \hat{E}_3^B(\boldsymbol{x}|\boldsymbol{x}^S, s)\boldsymbol{\nu}(\boldsymbol{x}) \cdot \partial\hat{\boldsymbol{J}}(\boldsymbol{x}, s)\mathrm{d}l(\boldsymbol{x}) \qquad (2.29)
\end{aligned}$$

where $\chi_\Omega(\boldsymbol{x})$ is the characteristic function $\chi_\Omega(\boldsymbol{x}) = \{1, 1/2, 0\}$ for $\boldsymbol{x} \in \{\Omega, \partial\Omega, \Omega'\}$ (Ω' denotes the complement of Ω in $\mathbb{R}^2$). Note that the second term on the right-hand side of Eq. (2.29) is zero for a planar circuit having the perfect magnetic wall along its boundary $\partial\Omega$ (see Eq. (2.6)). Following Eqs. (2.25)–(2.27), the test wave fields are linearly related to their source via

$$\hat{E}_3^B(\boldsymbol{x}|\boldsymbol{x}^S, s) = -s\mu \int_{\boldsymbol{x}^T\in\mathbb{R}^2} \hat{G}_\infty[r(\boldsymbol{x}|\boldsymbol{x}^T), s]\hat{J}_3^B(\boldsymbol{x}^T|\boldsymbol{x}^S, s)\mathrm{d}A(\boldsymbol{x}^T) \qquad (2.30)$$

$$\partial\hat{J}_\kappa^B(\boldsymbol{x}|\boldsymbol{x}^S, s) = -\int_{\boldsymbol{x}^T\in\mathbb{R}^2} \partial_\kappa\hat{G}_\infty[r(\boldsymbol{x}|\boldsymbol{x}^T), s]\hat{J}_3^B(\boldsymbol{x}^T|\boldsymbol{x}^S, s)\mathrm{d}A(\boldsymbol{x}^T) \qquad (2.31)$$

where $\hat{G}_\infty(r, s)$ is the bounded fundamental solution of the two-dimensional (modified) Helmholtz equation in $\mathbb{R}^2$ and

$$r(\boldsymbol{x}|\boldsymbol{x}^T) = |\boldsymbol{x} - \boldsymbol{x}^T| \qquad (2.32)$$

is the Eucledian distance between the points specified by position (two-dimensional) vectors $\boldsymbol{x}$ and $\boldsymbol{x}^T$. To get a boundary-contour relation, the testing surface electric current density is applied to the periphery of the circuit

$$\hat{J}_3^B(\boldsymbol{x}|\boldsymbol{x}^S, s) = \partial\hat{J}_3^B(\boldsymbol{x}|\boldsymbol{x}^S, s)\delta(\boldsymbol{x} - \boldsymbol{x}^S) \qquad (2.33)$$

where $\delta(\boldsymbol{x}-\boldsymbol{x}^S)$ being the Dirac delta distribution operative along $\boldsymbol{x}^S \in \partial\Omega$. In this way we get the following reciprocity relation

$$\begin{aligned}\tfrac{1}{2}\int_{\boldsymbol{x}\in\partial\Omega} &\hat{E}_3(\boldsymbol{x},s)\partial\hat{J}_3^B(\boldsymbol{x}|\boldsymbol{x}^S,s)\mathrm{d}l(\boldsymbol{x}) \\ &- \int_{\boldsymbol{x}\in\partial\Omega} \hat{E}_3(\boldsymbol{x},s)\boldsymbol{\nu}(\boldsymbol{x})\cdot\partial\hat{\boldsymbol{J}}^B(\boldsymbol{x}|\boldsymbol{x}^S,s)\mathrm{d}l(\boldsymbol{x}) \\ = \int_{\boldsymbol{x}\in\Omega} &\hat{E}_3^B(\boldsymbol{x}|\boldsymbol{x}^S,s)\hat{J}_3(\boldsymbol{x},s)\mathrm{d}A(\boldsymbol{x}) \\ &- \int_{\boldsymbol{x}\in\partial\Omega} \hat{E}_3^B(\boldsymbol{x}|\boldsymbol{x}^S,s)\boldsymbol{\nu}(\boldsymbol{x})\cdot\partial\hat{\boldsymbol{J}}(\boldsymbol{x},s)\mathrm{d}l(\boldsymbol{x}) \end{aligned} \tag{2.34}$$

with

$$\hat{E}_3^B(\boldsymbol{x}|\boldsymbol{x}^S,s) = -s\mu\int_{\boldsymbol{x}^T\in\partial\Omega}\hat{G}_\infty[r(\boldsymbol{x}|\boldsymbol{x}^T),s]\partial\hat{J}_3^B(\boldsymbol{x}^T|\boldsymbol{x}^S,s)\mathrm{d}l(\boldsymbol{x}^T) \tag{2.35}$$

$$\partial\hat{J}_\kappa^B(\boldsymbol{x}|\boldsymbol{x}^S,s) = -\int_{\boldsymbol{x}^T\in\partial\Omega}\partial_\kappa\hat{G}_\infty[r(\boldsymbol{x}|\boldsymbol{x}^T),s]\partial\hat{J}_3^B(\boldsymbol{x}^T|\boldsymbol{x}^S,s)\mathrm{d}l(\boldsymbol{x}^T) \tag{2.36}$$

Reciprocity relation (2.34) with Eqs. (2.35)–(2.36) serves as the basis for TD-CIM. This method yields the electric-field space-time distribution along the circuit boundary $\partial\Omega$, which is sufficient to characterize the planar circuit at hand. In particular, the superposition of the resulting field distribution along $\partial\Omega$ results in the field within circuit's domain Ω. The corresponding expression directly follows again from Eq. (2.29) along with the magnetic-wall boundary condition (2.5), i.e.

$$\begin{aligned}\hat{E}_3(\boldsymbol{x}^S,s) = -s\mu &\int_{\boldsymbol{x}\in\Omega}\hat{G}_\infty[r(\boldsymbol{x}|\boldsymbol{x}^S),s]\hat{J}_3(\boldsymbol{x},s)\mathrm{d}A(\boldsymbol{x}) \\ &- \int_{\boldsymbol{x}\in\partial\Omega}\hat{E}_3(\boldsymbol{x},s)\partial_\nu\hat{G}_\infty[r(\boldsymbol{x}|\boldsymbol{x}^S),s]\mathrm{d}l(\boldsymbol{x})\end{aligned} \tag{2.37}$$

for $\boldsymbol{x}^S \in \Omega$, where we have let $\hat{J}_3^B(\boldsymbol{x}|\boldsymbol{x}^S,s) = \delta(\boldsymbol{x}-\boldsymbol{x}^S)$. Obviously, the first term on the right-hand side can be interpreted as the primary field due to the excitation port whose action is accounted for by $\hat{J}_3$, while the second term represents the superposition of secondary contributions emanating from the circuit rim. It should be stressed that Eq. (2.37) is not an integral equation to solve but rather a formula to be evaluated for the (known) excitation and the field distribution on $\partial\Omega$. A numerical example concerning the superposition integral can be found in Sec. 6.2.1.

2.1.3 An alternative formulation

Yet another formulation that shows a relation between the boundary-value and reciprocity-based formulations may be studied. To this end, let the testing field satisfies the complex-FD field equations (2.25)–(2.27) for all $\boldsymbol{x} \in \Omega$ with the magnetic-wall boundary condition, i.e.

$$(\boldsymbol{i}_3 \times \boldsymbol{\nu}) \cdot \hat{\boldsymbol{H}}^B(\boldsymbol{x} + \delta\boldsymbol{\nu}, s) = 0 \quad \text{as } \delta \downarrow 0 \tag{2.38}$$

for all $\boldsymbol{x} \in \partial\Omega$. Further, without loss of generality, let us assume that the circuit is activated via a vertical electric-current port only, i.e. with no current injected into the circuit's rim. Taking into account that the actual field state remains the same as in Sec. 2.1, the corresponding global reciprocity relation reads (cf. Eq. (2.29))

$$\int_{\boldsymbol{x}\in\Omega} \hat{E}_3(\boldsymbol{x}, s)\hat{J}_3^B(\boldsymbol{x}|\boldsymbol{x}^S, s)\mathrm{d}A(\boldsymbol{x}) = \int_{\boldsymbol{x}\in\Omega} \hat{E}_3^B(\boldsymbol{x}|\boldsymbol{x}^S, s)\hat{J}_3(\boldsymbol{x}, s)\mathrm{d}A(\boldsymbol{x}) \tag{2.39}$$

with

$$\hat{E}_3^B(\boldsymbol{x}|\boldsymbol{x}^S, s) = -s\mu \int_{\boldsymbol{x}^T\in\Omega} \hat{G}[r(\boldsymbol{x}|\boldsymbol{x}^T), s]\hat{J}_3^B(\boldsymbol{x}^T|\boldsymbol{x}^S, s)\mathrm{d}A(\boldsymbol{x}^T) \tag{2.40}$$

$$\partial\hat{J}_\kappa^B(\boldsymbol{x}|\boldsymbol{x}^S, s) = -\int_{\boldsymbol{x}^T\in\Omega} \partial_\kappa\hat{G}[r(\boldsymbol{x}|\boldsymbol{x}^T), s]\hat{J}_3^B(\boldsymbol{x}^T|\boldsymbol{x}^S, s)\mathrm{d}A(\boldsymbol{x}^T) \tag{2.41}$$

where the Green's function satisfies the boundary-value problem defined in (2.9) and (2.10). Obviously, for a spatially concentrated point source

$$\hat{J}_3^B(\boldsymbol{x}|\boldsymbol{x}^S, s) = \hat{I}^B(s)\delta(\boldsymbol{x} - \boldsymbol{x}^S) \tag{2.42}$$

with the Dirac distribution operative at $\boldsymbol{x}^S \in \Omega$ one arrives back at the field representation (2.11) provided that we invoke the condition that the resulting relation has to hold for arbitrary values of $\hat{I}^B(s)$.

2.1.4 Modeling of excitation ports

Microstrip-line feeds and vertical ports are the most common means for exciting EM fields in planar circuits. Accordingly, in this section we describe a way how these ports can be implemented in CIM-based techniques. An example of the circuit with a microstrip excitation port on the circuit periphery (PORT 1), a vertical excitation port (PORT 2), and two observation probes (PROBE 1 and PROBE 2) is shown in Fig. 2.3.

Let us first describe the excitation port activated by the electric-current surface density according to the excitation condition (2.5). Along (relatively

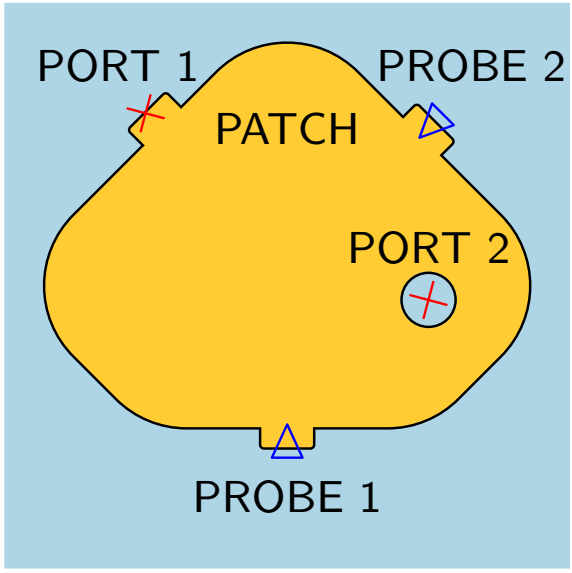

Figure 2.3: Planar circuit with its excitation ports and measurement probes.

small) line elements of the port's periphery, we assume the constant electric-current distribution (see Fig. 2.4). For the normal component of the excitation current injected *into* a line element $\triangle\Omega^{[P]} \subset \partial\Omega$ we write

$$\boldsymbol{\nu}(\boldsymbol{x}) \cdot \partial\hat{\boldsymbol{J}}(\boldsymbol{x}, s) = -\hat{I}(s)\Pi^{[P]}(\boldsymbol{x})/|\triangle\Omega^{[P]}| \tag{2.43}$$

where $\hat{I}(s)$ is the electric current applied to the excitation segment, $\Pi^{[P]}(\boldsymbol{x})$ is the rectangular function defined as

$$\Pi^{[P]}(\boldsymbol{x}) = \begin{cases} 1 & \text{if } \boldsymbol{x} \in \triangle\Omega^{[P]} \\ 0 & \text{elsewhere} \end{cases} \tag{2.44}$$

and $|\triangle\Omega^{[P]}|$ denotes the length of the excitation segment. In Eq. (2.43) one has to take care of the orientation of the injected current. In this respect it is worth to note that the right-hand side of Eq. (2.34) shows equivalence between the vertical and horizontal excitation current densities in the formulated two-dimensional model (see also [35, Sec. 9.3.1]). This implies that in the two-dimensional model it does not make sense to strictly distinguish between the action of the vertical electric-current density J_3 and the horizontal electric-current density $-\boldsymbol{\nu} \cdot \partial\boldsymbol{J}$ injected into the circuit periphery $\partial\Omega$. Upon combining the second term on the right-hand side of Eq. (2.34) with

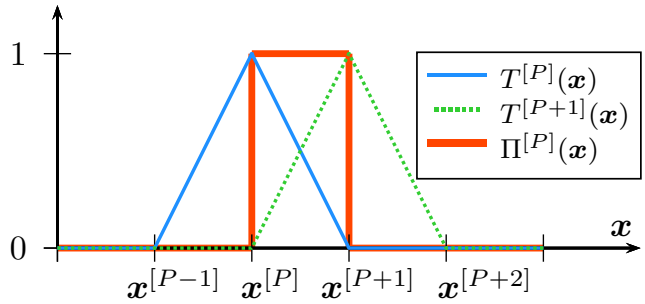

Figure 2.4: Modeling of the injected excitation current over a line element.

Eqs. (2.35) and (2.43) we finally arrive at

$$\left[-s\mu\hat{I}(s)/|\triangle\Omega^{[P]}|\right]\int_{\boldsymbol{x}^T\in\partial\Omega}\partial\hat{J}_3^B(\boldsymbol{x}^T|\boldsymbol{x}^S,s)\int_{\boldsymbol{x}\in\triangle\Omega^{[P]}}\hat{G}_\infty[r(\boldsymbol{x}|\boldsymbol{x}^T),s]\mathrm{d}l(\boldsymbol{x})\mathrm{d}l(\boldsymbol{x}^T) \tag{2.45}$$

The integrals in Eq. (2.45) do not present any difficulties except for overlapping discretization segments where the Green's function shows the logarithmic singularity at $\boldsymbol{x}=\boldsymbol{x}^T$. In such a case, one can use the generic integral given in Appendix A to evaluate the inner integral. Since the testing source density $\hat{J}_3^B$ is assumed to be a piecewise linear function composed of $T^{[m]}(\boldsymbol{x})$ (see Fig. 2.4), the outer integral over $\boldsymbol{x}^T$ easily follows.

Alternatively, one may avoid the singularity by assuming a vertical port of the circular cross-section whose boundary contour does not belong to $\partial\Omega$. The starting point now is the first term on the right-hand side of Eq. (2.34) with Eq. (2.35), i.e.

$$(-s\mu/2\pi)\int_{\boldsymbol{x}^T\in\partial\Omega}\partial\hat{J}_3^B(\boldsymbol{x}^T|\boldsymbol{x}^S,s)\int_{\boldsymbol{x}\in\Omega^Q}\hat{J}_3(\boldsymbol{x},s)\mathrm{K}_0[\hat{\gamma}(s)r(\boldsymbol{x}|\boldsymbol{x}^T)]\mathrm{d}A(\boldsymbol{x})\mathrm{d}l(\boldsymbol{x}^T) \tag{2.46}$$

where $\mathrm{K}_0(x)$ is the modified Bessel function of the second kind and the zeroth order that represents the (bounded) fundamental solution of the modified Helmholtz equation in $\mathbb{R}^2$ [58, Sec. 11.2] (see also Sec. 2.1.1). In Eq. (2.46), $\Omega^Q=\mathrm{supp}[\hat{J}_3(\boldsymbol{x},s)]\subset\Omega$ is the support of the excitation vertical electric-current volume density. Now, if we assume that Ω^Q is a circular domain whose radius ρ is sufficiently small with respect to the spatial support of the excitation electric-current pulse, we may approximately take

$$\hat{J}_3(\boldsymbol{x},s)\simeq\hat{I}(s)/\pi\rho^2\quad\text{for }\boldsymbol{x}\in\Omega^Q \tag{2.47}$$

Consequently, with the aid of the addition theorems for Bessel functions (see [92, Sec. 6.11] and [1, (9.6.3), (9.6.4)]), the inner integral can be evaluated analytically, i.e.

$$\frac{1}{\pi\rho^2}\frac{1}{2\pi}\int_{\boldsymbol{x}\in\Omega^Q}\mathrm{K}_0[\hat{\gamma}(s)r(\boldsymbol{x}|\boldsymbol{x}^T)]\mathrm{d}A(\boldsymbol{x}) = \frac{1}{\pi}\,\frac{1}{\hat{\gamma}(s)\rho}\,\mathrm{I}_1[\hat{\gamma}(s)\rho]\mathrm{K}_0[\hat{\gamma}(s)r(\boldsymbol{x}^C|\boldsymbol{x}^T)] \tag{2.48}$$

where $\boldsymbol{x}^T \in \partial\Omega$ and $\boldsymbol{x}^C \in \Omega$ gives the center of the circular excitation-port domain. Upon collecting the results and using the limit $\lim_{x\downarrow 0}\mathrm{I}_1(x)/x = 1/2$, the interaction integral (2.46) can be finally simplified to

$$\Big[-s\mu\hat{I}(s)/2\pi\Big]\int_{\boldsymbol{x}^T\in\partial\Omega}\partial\hat{J}_3^B(\boldsymbol{x}^T|\boldsymbol{x}^S,s)\mathrm{K}_0[\hat{\gamma}(s)r(\boldsymbol{x}^C|\boldsymbol{x}^T)]\mathrm{d}l(\boldsymbol{x}^T) \tag{2.49}$$

Since the circular port is placed in domain Ω occupied by the conducting plates, it is clear that the logarithmic singularity is in Eq. (2.49) avoided. The second way, on the other hand, is limited to the excitation ports of the circular cross-section. Illustrative MATLAB® implementations of the described TD-CIM excitation ports can be found in Sec. B.3.

2.2 Conclusions

It has been demonstrated that a planar circuit can be analyzed with the aid of the eigenfunction-expansion method and the reciprocity-based contour-integral formulation. Since the former approach yields closed-form analytical solutions for generic circuit shapes, this method is suitable for validating computational techniques such as TD-CIM. Owing to the fact that any numerical modeling of EM field excitation mechanisms has the decisive impact on the proper evaluation of a planar circuit, a great deal of attention has been paid to the embedding of its excitation ports. The introduced formulations provide the solid basis for the subsequent chapter where TD-CIM is described in detail.

Chapter 3

Instantaneously-reacting planar circuits

The present chapter[1] provides a numerical procedure for solving the contour-integral reciprocity relation in TD for the case of a loss-free, instantaneously reacting planar circuit [108]. Without loss of generality, we assume that the planar circuit is excited by the electric-current surface density injected into its periphery. Owing to the equivalence noted in Sec. 2.1.4, the vertical excitation port may be modeled along the same lines. Since the loss-free section of the circuit's rim constitutes the perfect magnetic wall with the vanishing tangential component of the magnetic field strength, such a structure cannot in principle radiate and may be thus viewed as a closed resonator.

It turns out that the proposed approach leads to a system of algebraic equations that is solvable in an updating step-by-step manner. Within the tested input parameters it was observed that the resulting numerical scheme is stable provided that the relevant matrix elements are evaluated accurately enough to prevent from the error-accumulation instabilities (see [99]). The proposed technique thus makes possible to investigate the pulse-shaped signal transfer between source and receiver ports placed along the periphery of an arbitrarily-shaped planar circuit.

The following sections are organized as follows. The chapter starts with the numerical solution of the reciprocity-based contour-integral relation. In order to validate the numerical results, an analytical closed-form solution is constructed for a rectangular circuit in Sec. 3.2. The closed-form solution is based on the eigenfunction expansion as given in Sec. 2.1.1. Finally, sample numerical calculations are presented in Sec. 3.3. Here, the introduced com-

[1]This chapter is largely based on Reference [108]. Adapted with permission from IEEE, © 2014 IEEE.

putational procedure is validated using the analytical eigenfunction-based expressions and with the aid of FIT.

3.1 Numerical solution of the reciprocity formulation

With the help of the bounded fundamental solution of the modified Helmholtz equation in $\mathbb{R}^2$ [58, Sec. 11.2], Eqs. (2.34)–(2.36) lead to

$$\begin{aligned}
&\int_{\boldsymbol{x}\in\partial\Omega} \hat{E}_3(\boldsymbol{x},s)\partial\hat{J}_3^B(\boldsymbol{x}|\boldsymbol{x}^S,s)\mathrm{d}l(\boldsymbol{x}) \\
&= (s/c\pi)\int_{\boldsymbol{x}\in\partial\Omega} \hat{E}_3(\boldsymbol{x},s)\int_{\boldsymbol{x}^T\in\partial\Omega} \mathrm{K}_1\left[sr(\boldsymbol{x}|\boldsymbol{x}^T)/c\right] \\
&\qquad\qquad \partial\hat{J}_3^B(\boldsymbol{x}^T|\boldsymbol{x}^S,s)\cos[\theta(\boldsymbol{x}|\boldsymbol{x}^T)]\mathrm{d}l(\boldsymbol{x}^T)\mathrm{d}l(\boldsymbol{x}) \\
&+(s\mu/\pi)\int_{\boldsymbol{x}\in\partial\mathcal{S}} \boldsymbol{\nu}(\boldsymbol{x})\cdot\partial\hat{\boldsymbol{J}}(\boldsymbol{x},s)\int_{\boldsymbol{x}^T\in\partial\Omega} \mathrm{K}_0\left[sr(\boldsymbol{x}|\boldsymbol{x}^T)/c\right] \\
&\qquad\qquad \partial\hat{J}_3^B(\boldsymbol{x}^T|\boldsymbol{x}^S,s)\mathrm{d}l(\boldsymbol{x}^T)\mathrm{d}l(\boldsymbol{x})
\end{aligned} \tag{3.1}$$

for $\boldsymbol{x}^S \in \partial\Omega$, with $\partial\mathcal{S} \subset \partial\Omega$ and $\cos(\theta) = \partial_\nu r$. Although the reciprocity-based relation (3.1) will be numerically solved in TD, it is convenient to perform a few next steps in complex-FD. As to the problem discretization, the time coordinate $\{t \in \mathbb{R}; t > 0\}$ is discretized in NT instants with the constant time step $\triangle t$

$$\mathcal{T} = \{t_k \in \mathbb{R}; t_k = k\triangle t, \triangle t > 0, k = 1, ..., NT\} \tag{3.2}$$

and the circuit periphery $\partial\Omega$ is discretized into N disjoint line segments

$$\partial\Omega \simeq \cup_{m=1}^{N} \triangle\Omega^{[m]} \tag{3.3}$$

and $|\triangle\Omega^{[m]}| = |\boldsymbol{x}^{[m+1]} - \boldsymbol{x}^{[m]}|$ is the length of the m-th segment and $\boldsymbol{x}^{[m]}$ is the position vector of the m-th discretization node. The approximation of the circuit periphery by straight-line segments is shown in Fig. 3.1. In the next step, the electric field strength is expanded piecewise linearly both in space and time, i.e.

$$\hat{E}_3(\boldsymbol{x},s) = \sum_{m=1}^{N}\sum_{k=1}^{NT} e_{[k]}^{[m]} T^{[m]}(\boldsymbol{x})\hat{T}_{[k]}(s) \tag{3.4}$$

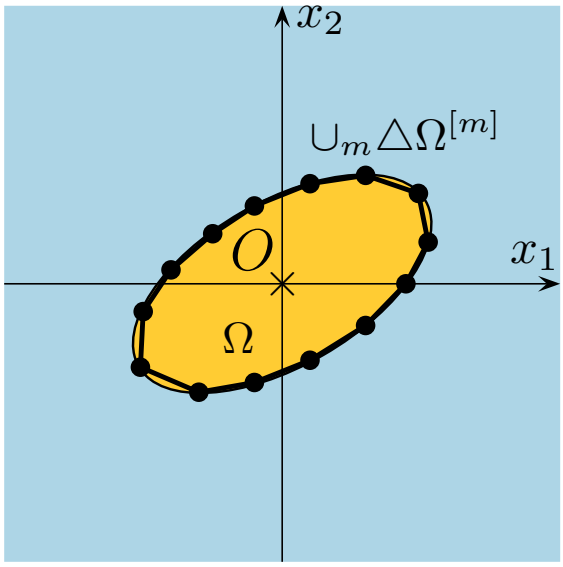

Figure 3.1: Boundary contour and its approximation by straight-line segments. From [108], adapted with permission from IEEE, © 2014 IEEE.

where $e_{[k]}^{[m]}$ is the yet unknown coefficient, $T^{[m]}(\boldsymbol{x})$ is the triangular function associated with the m-th node along $\partial\Omega$

$$T^{[m]}(\boldsymbol{x}) = \begin{cases} \left(\boldsymbol{x} - \boldsymbol{x}^{[m-1]}\right) / |\triangle\Omega^{[m-1]}| & \text{if } \boldsymbol{x}^{[m-1]} \leq \boldsymbol{x} \leq \boldsymbol{x}^{[m]} \\ \left(\boldsymbol{x}^{[m+1]} - \boldsymbol{x}\right) / |\triangle\Omega^{[m]}| & \text{if } \boldsymbol{x}^{[m]} \leq \boldsymbol{x} \leq \boldsymbol{x}^{[m+1]} \end{cases} \tag{3.5}$$

for all $m = \{1, \cdots, N\}$ and $\hat{T}_{[k]}(s)$ is the complex-FD counterpart of the temporal triangle function (see Appendix E.1)

$$T_{[k]}(t) = \begin{cases} 1 - k + t/\triangle t & \text{if } k - 1 \leq t/\triangle t \leq k \\ 1 + k - t/\triangle t & \text{if } k \leq t/\triangle t \leq k + 1 \end{cases} \tag{3.6}$$

for all $k = \{1, \cdots, NT\}$. The testing surface current density is taken to be piecewise linear in space and its complex-FD counterpart at the S-th node is

$$\partial\hat{J}_3^B(\boldsymbol{x}|\boldsymbol{x}^S, s) = \hat{j}_3^{[S]}(s) T^{[S]}(\boldsymbol{x}) \tag{3.7}$$

for all $S = \{1, \cdots, N\}$ and where we take $\hat{j}_3^{[S]}(s) = 1$ which corresponds to the 'point matching' in time. The injected electric-current surface density is assumed to be constant over segments modeling the excitation port. Substituting of Eqs. (3.4) and (3.7) into a discretized form of Eq. (3.1) we end up

with the system of algebraic equations

$$\left(\boldsymbol{I}-\boldsymbol{Q}_{[0]}\right)\,\cdot\,\boldsymbol{E}_{[p]}=\sum_{k=1}^{p-1}\boldsymbol{Q}_{[p-k]}\,\cdot\,\boldsymbol{E}_{[k]}+\boldsymbol{F}_{[p]} \tag{3.8}$$

that can be solved in a step-by-step manner for all $p=\{1,\cdots,NT\}$. Here, $\boldsymbol{E}_{[p]}$ is a 2D-array of $[N\times NT]$ unknown coefficients at $t_p=p\triangle t$, $\boldsymbol{I}$ is a three-diagonal $[N\times N]$ 2D-array with elements

$$\begin{aligned}(\boldsymbol{I})_{S,m}&=\left(\triangle\Omega^{[S-1]}/6\right)\delta_{S-1,m}\\&\quad+\left(\triangle\Omega^{[S-1]}/3+\triangle\Omega^{[S]}/3\right)\delta_{S,m}+\left(\triangle\Omega^{[S]}/6\right)\delta_{S+1,m}\end{aligned} \tag{3.9}$$

and $\boldsymbol{Q}_{[p-k]}$ is a time-dependent $[N\times N\times NT]$ 3D-array whose elements are given as

$$\begin{aligned}(\boldsymbol{Q}_{[p-k]})_{S,m}=\frac{1}{\pi c\triangle t}\int_{\boldsymbol{x}^T\in\partial\Omega}T^{[S]}(\boldsymbol{x}^T)\int_{\boldsymbol{x}\in\partial\Omega}T^{[m]}(\boldsymbol{x})\\\Psi[r(\boldsymbol{x}|\boldsymbol{x}^T),(p-k)\triangle t]\cos[\theta(\boldsymbol{x}|\boldsymbol{x}^T)]\mathrm{d}l(\boldsymbol{x})\mathrm{d}l(\boldsymbol{x}^T)\end{aligned} \tag{3.10}$$

for all $S=\{1,\cdots,N\}$, $m=\{1,\cdots,N\}$ and $t\in\mathcal{T}$. The excitation is accounted for via an $[N\times NT]$ 2D-array $\boldsymbol{F}_{[p]}$ whose elements read

$$(\boldsymbol{F}_{[p]})_S=\frac{1}{\pi|\partial\mathcal{S}|}\int_{\boldsymbol{x}^T\in\partial\Omega}T^{[S]}(\boldsymbol{x}^T)\int_{\boldsymbol{x}\in\partial\mathcal{S}}\Phi[r(\boldsymbol{x}|\boldsymbol{x}^T),p\triangle t]\mathrm{d}l(\boldsymbol{x})\mathrm{d}l(\boldsymbol{x}^T) \tag{3.11}$$

for all $S=\{1,\cdots,N\}$ and all $t\in\mathcal{T}$, where $|\partial\mathcal{S}|$ denotes the arc length of $\partial\mathcal{S}\subset\partial\Omega$. The time-dependent functions in Eqs. (3.10) and (3.11) are

$$\Psi(r,t)=\psi(r,t+\triangle t)-2\psi(r,t)+\psi(r,t-\triangle t) \tag{3.12}$$

$$\psi(r,t)=(c^2t^2/r^2-1)^{1/2}\mathrm{H}(t-r/c) \tag{3.13}$$

$$\Phi(r,t)=-\mu\partial_t\mathcal{I}(t)*(t^2-r^2/c^2)^{-1/2}\mathrm{H}(t-r/c) \tag{3.14}$$

where $\mathcal{I}(t)$ is the source signature of the electric current injected into the circuit periphery and $\mathcal{I}(t)=0$ for $t<0$. It is worth noting that the source signature must be smooth enough to get an integrable singularity in Eq. (3.14) as $r\downarrow 0$. For piecewise constant/linear excitation signatures such as the rectangular or trapezoidal pulses, the time-integrated equivalent of the reciprocity relation (3.1) seems to be the shortest way to circumvent the limitation. The spatial singularity as $\boldsymbol{x}$ approaches $\boldsymbol{x}^T$ must be carefully handled via the limiting analytical procedure [120]. To this end, it is convenient to start over with Eq. (3.1) and use a small-argument expansion of the modified Bessel function [1, Eq. (9.6.13)]

$$\mathrm{K}_0(x)=\ln(2/x)-\gamma+\mathcal{O}(x^2)\text{ as }x\downarrow 0 \tag{3.15}$$

where γ is Euler's constant. The corresponding integrals of the logarithmic function and its normal derivative are evaluated in Appendix A. As is shown, the latter integral gives a zero contribution for the self-coupling terms in Eq. (3.10). Since the 2D-arrays on the left-hand side of Eq. (3.8) do not depend on time, the matrix inversion is needed only once. Moreover, if $c\triangle t < \min_{S,m}[r(\boldsymbol{x}|\boldsymbol{x}^T)]$, then all elements of $\boldsymbol{Q}_{[0]}$ are zero and only the three-diagonal matrix inversion is required. For this case, efficient algorithms do exist (e.g. [38, Sec. 1.5]). More details on implementation aspects along with the corresponding demo MATLAB® codes can be found in Appendix B.

Finally note that under certain circumstances it may happen that in the effort to keep the left-hand side of Eq. (3.8) as simple as possible, a smoother temporal expansion is necessary. For such a case, several suitable expansion functions are given in Appendix E. The use of the the quadratic expansion functions $B_{[k]}(t)$ (see Sec. E.2), for instance, yields

$$\begin{aligned}\Psi(r,t) &= \psi(r,t+\triangle t) - 2\psi(r,t+\triangle t/2) \\ &\quad + 2\psi(r,t-\triangle t/2) - \psi(r,t-\triangle t) \qquad (3.16)\\ \psi(r,t) &= (2t/\triangle t)\left(c^2t^2/r^2-1\right)^{1/2}\mathrm{H}(t-r/c) \\ &\quad - (2r/c\triangle t)\ln\left[ct/r+\left(c^2t^2/r^2-1\right)^{1/2}\right]\mathrm{H}(t-r/c) \qquad (3.17)\end{aligned}$$

which simply replace Eqs. (3.12) and (3.13), respectively.

3.2 Analytical solutions based on the eigenfunction expansion

The main concern of this section is to provide analytical closed-form solutions that will serve for validation of TD-CIM. To this end we analyze a planar circuit of the rectangular shape for which the eigenfunction expansion (2.16) is well-known in closed form.

At first let us assume a rectangular circuit of dimensions $L \times W$ that is excited by a microstrip port placed along the circuit periphery $\partial\Omega^S = \{\boldsymbol{x} \in \mathbb{R}^2; T - P/2 \le x_1 \le T + P/2, x_2 = 0\}$ (see Fig. 3.2a). Then for the receiving probe of the rectangular shape $\Omega^P = \{\boldsymbol{x} \in \mathbb{R}^2; x_1^P - W_1^P/2 \le x_1 \le x_1^P + W_1^P/2, x_2^P - W_2^P/2 \le x_2 \le x_2^P + W_2^P/2\}$, Eq. (2.20) with the integrations taken over $\partial\Omega^S$ and Ω^P leads to the following complex-FD transfer impedance

$$\hat{Z}(s) = \frac{s\mu d}{LW}\sum_{m=0}^{\infty}\sum_{n=0}^{\infty}\frac{e_m^2 e_n^2}{k_m^2+k_n^2+s^2/c^2}F_{mn}^S F_{mn}^P \qquad (3.18)$$

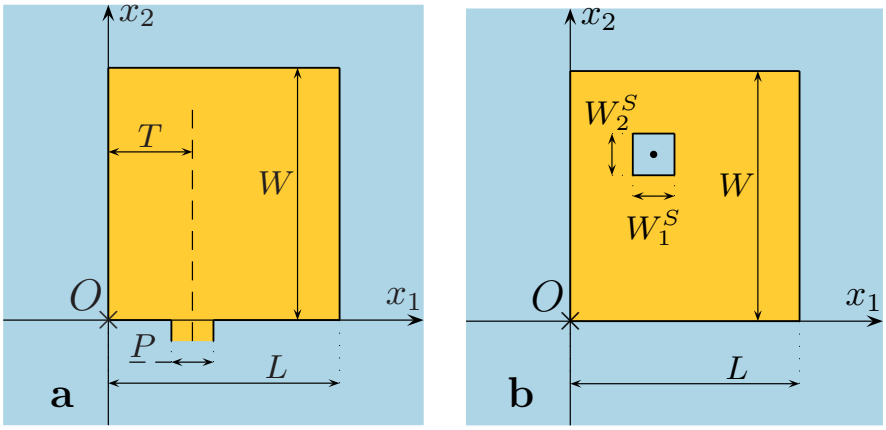

Figure 3.2: Rectangular planar circuits excited via a (a) microstrip-line source; (b) vertical-probe source. From [108], adapted with permission from IEEE, © 2014 IEEE.

where

$$F_{mn}^S = \cos(k_m T)\mathrm{sinc}(k_m P/2) \tag{3.19}$$

$$F_{mn}^P = \cos(k_m x_1^P)\cos(k_n x_2^P)\mathrm{sinc}(k_m W_1^P/2)\mathrm{sinc}(k_n W_2^P/2) \tag{3.20}$$

with $e_m = 1$ for $m = 0$ and $e_m = \sqrt{2}$ for $m \neq 0$ and $k_m = m\pi/L$ and $k_n = n\pi/W$. Here, the results of Sec. 2.1.1 are used. Note that a probe of vanishing dimensions can be handled via a limiting process. For a point probe, for instance, we get

$$F_{mn}^P = \cos(k_m x_1^P)\cos(k_n x_2^P) \tag{3.21}$$

as $W_1^P \downarrow 0$ and $W_2^P \downarrow 0$. The TD counterpart of $\hat{Z}(s)$ can be found by applying the inverse Laplace transform to the terms in the sum of Eq. (3.18). With the help of [1, Eqs. (29.3.1),(29.3.16)] we find

$$\mathcal{Z}(t) = \frac{d}{LW}\frac{1}{\epsilon}\sum_{m=0}^{\infty}\sum_{n=0}^{\infty} e_m^2 e_n^2 \cos[ct(k_m^2 + k_n^2)^{1/2}]\mathrm{H}(t)F_{mn}^S F_{mn}^P \tag{3.22}$$

As the second example we take the rectangular circuit excited by a vertical excitation port placed on the patch Ω (see Fig. 3.2b). In such a case, the excitation port occupies a rectangular domain $\Omega^S = \{\boldsymbol{x} \in \mathbb{R}^2; x_1^S - W_1^S/2 \leq x_1 \leq x_1^S + W_1^S/2, x_2^S - W_2^S/2 \leq x_2 \leq x_2^S + W_2^S/2\}$. Again, the TD impedance follows from Eq. (3.22) with (3.20) in which F_{mn}^S is modified accordingly

$$F_{mn}^S = \cos(k_m x_1^S)\cos(k_n x_2^S)\mathrm{sinc}(k_m W_1^S/2)\mathrm{sinc}(k_n W_2^S/2) \tag{3.23}$$

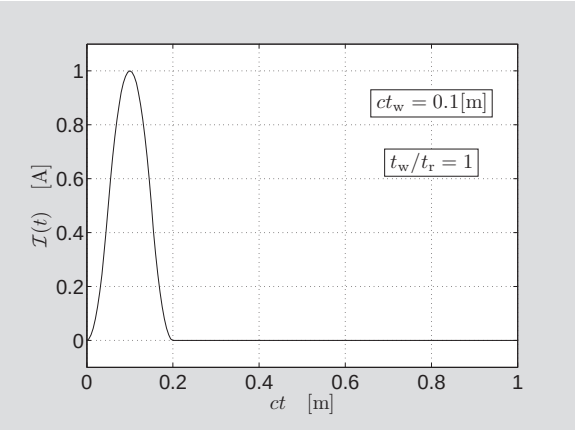

Figure 3.3: The bell-shaped excitation signature. Taken from [108] with permission from IEEE, © 2014 IEEE.

Finally, the transient voltage $\mathcal{V}(t)$ at the position of the probe due to the impulsive source $\mathcal{I}(t)$ can be found with the help of the time convolution in Eq. (2.21).

3.3 Validation of numerical results

In this section we analyze the loss-free rectangular planar circuits whose configurations are shown in Fig. 3.2. In the both cases we consider the planar circuit of dimensions $L = 0.1\,[\mathrm{m}]$ and $W = 0.2\,[\mathrm{m}]$ with the dielectric filling of thickness $d = 1.50\,[\mathrm{mm}]$ showing the electric permittivity $\epsilon = 2.0\,\epsilon_0$ and magnetic permeability $\mu = \mu_0$. The corresponding EM wave speed in the dielectric layer is $c = (\epsilon\mu)^{-1/2}$.

The circuits are excited using the bell-shaped pulse being defined in Appendix D with the amplitude $A = 1.0\,[\mathrm{A}]$ and with the pulse time width $ct_{\rm w} = 0.10\,[\mathrm{m}]$ (see Fig. 3.3). Note that the thin-layer assumption $ct_{\rm w} \gg d$ is then satisfied. The transient voltage responses are observed within the finite time window $\{0 \leq ct \leq 3.0\}\,[\mathrm{m}]$. For the numerical solution, the circuit periphery is divided into the line segments of length $|\triangle\Omega^{[n]}| = 0.02\,[\mathrm{m}]$, which corresponds to a fifth of the excitation pulse spatial support $ct_{\rm w}$. The spatial integrals in Eqs. (3.10) and (3.11) are evaluated using the 12-point Gauss-Legendre quadrature [1, (25.4.30)]. As the reference solution we use Eq. (3.22), where the number of terms is truncated as $m = \{0, \ldots, M\}$ and $n = \{0, \ldots, N\}$, with $M = N = 1000$.

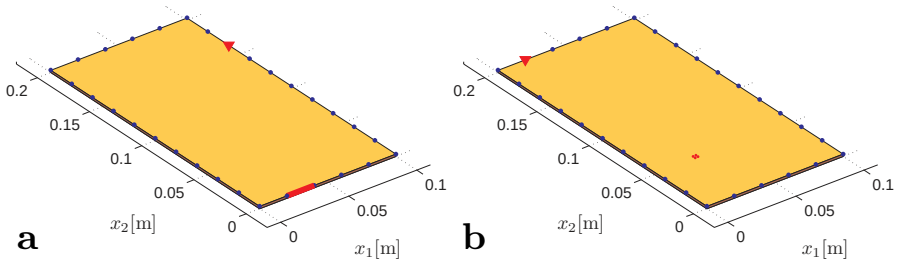

Figure 3.4: Computational models of the analyzed rectangular circuits with probes (the solid triangles on the circuit peripheries); (a) a microstrip port feeding (the bold line); (b) a vertical port (the dots on the patch).

3.3.1 Rectangular circuit fed by a microstrip port

In the first example we analyze the pulse propagation over the circuit excited by the microstrip port with the parameters $T = 0.03\,[\mathrm{m}]$ and $P = 0.02\,[\mathrm{m}]$. The pulsed voltage is observed along an edge of the circuit at a discretization point placed at $\{x_1^P, x_2^P\} = \{0.1, 0.16\}\,[\mathrm{m}]$ with $W_1^P \downarrow 0$ and $W_2^P \downarrow 0$ (see Fig. 3.4a).

The pulse shape found via TD-CIM is compared with the analytical solution evaluated using the truncated modification of Eq. (3.22) with Eqs. (3.19), (3.21) and (2.21). The corresponding results are shown in Fig. 3.5a. Despite the coarse spatial discretization, the resulting pulse shapes agree very well.

3.3.2 Rectangular circuit fed by a vertical port

As the second example we observe the pulse propagation over the circuit excited by a vertical port having the rectangular cross section placed at $\{x_1^S, x_2^S\} = \{0.03, 0.05\}\,[\mathrm{m}]$ with $W_1^S = W_2^S = 2.0\,[\mathrm{mm}]$. The resulting voltage response is probed at $\{x_1^P, x_2^P\} = \{0.02, 0.2\}\,[\mathrm{m}]$ (see Fig. 3.4b). In the analytical expression (3.22) we use Eqs. (3.21) and (3.23). As can be seen from Fig. 3.5b, the results are almost identical. Even better agreement can be achieved with a finer discretization or/and with a higher number of points in the Gauss-Legendre quadrature.

3.4 Comparison with an alternative numerical technique

Another way to validate the introduced TD-CIM is to compare its results with the corresponding outputs from alternative numerical techniques. To

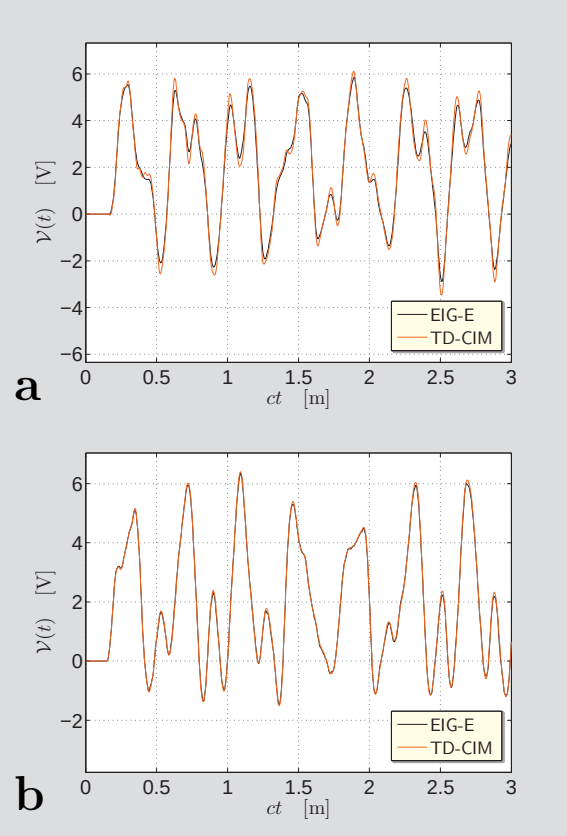

Figure 3.5: The pulsed voltage evaluated using TD-CIM and the eigenfunction expansion method (EIG-E) as observed at the (a) probe shown in Fig. 3.4a; (b) probe shown in Fig. 3.4b. From [108], adapted with permission from IEEE, © 2014 IEEE.

this end, we may use FIT as implemented in CST Microwave Studio®, for example. As to the circuits excitation, we use the model of a vertical port. For the TD-CIM simulation, the port has a hexagonal cross-section of the circumradius 1.0 [mm], while in the FIT-based simulation the circular port of radius 1.0 [mm] is used. The port is activated by the bell-shaped source signature plotted in Fig. 3.3. The distance between the PEC planes is again $d = 1.50\,[\mathrm{mm}]$ and the electric permittivity of the loss-free dielectric filling is $\epsilon = 2.50\,\epsilon_0$. The transient voltage response is observed at a specified position on the circuit periphery within the finite time window of observation $\{0 \leq ct \leq 3.0\}\,[\mathrm{m}]$. The FIT models are discretized with a hexahedral mesh. The upper and bottom planes are assumed to be perfectly electrically conducting. The sidewalls of the surrounding box are defined as the magnetic

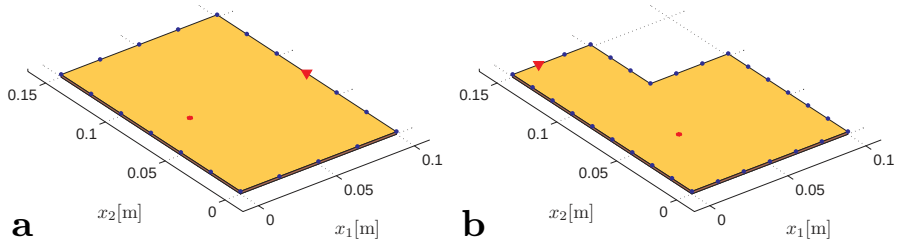

Figure 3.6: Computational models of the analyzed circuits with probes (the solid triangles on the circuit peripheries) and with vertical ports (the dots on the patch); (a) the rectangular circuit; (b) the irregularly-shaped circuit.

walls with the vanishing tangential magnetic-field component.

Our first structure is of the rectangular shape and its model as discretized for TD-CIM is shown in Fig. 3.6a. The excitation port has its center at $\{x_1^S, x_2^S\} = \{0.025, 0.075\}$ [m]. The discretization of circuit's rim is uniform with the line segment of length $|\triangle\Omega^{[n]}| = 0.025$ [m], which corresponds to a quarter of the excitation pulse spatial support $ct_{\mathrm{w}} = 0.10$ [m]. The total number of the discretization segments along the circuit periphery is 20. Our reference FIT-based model consists of about 65 of thousands mesh cells. The voltage pulses observed at $\{x_1^P, x_2^P\} = \{0.1, 0.075\}$ [m] are shown in Fig. 3.7a. As the excited field quantities causally evolve in time, we can conclude that the good agreement of the early-time responses implies a very good correspondence of our simplified excitation model with the reference one used in the FIT-based analysis. On the other hand, the differences become evident at the late-time part of the response. This observation implies slightly different behavior of the sidewalls where the reflections take place. This can be naturally expected by virtue of the different numerical strategies to tackle the problem.

The effect of the circuit boundary is even more pronounced in the second example shown in Fig. 3.6b. Its excitation port has its center at $\{x_1^S, x_2^S\} = \{0.03, 0.05\}$ [m]. The discretization is again uniform with $|\triangle\Omega^{[n]}| = 0.0167$ [m], which corresponds to a sixth of the excitation pulse spatial support $ct_{\mathrm{w}} = 0.10$ [m]. The total number of the discretization segments along the circuit periphery is then 30, while the FIT model consists of 78 of thousands mesh cells. The voltage pulse shapes observed at $\{x_1^P, x_2^P\} = \{0.0167, 0.15\}$ [m] are shown in Fig. 3.7b. The deviations at the late-time part of the responses can be attributed to different boundary conditions along the circuit's rim. While the CIM-based model assumes the perfect magnetic wall along the entire periphery, the magnetic wall in the FIT-based model is placed along the sidewalls of the surrounding box $x_1 = \{0, 0.10\}$ [m], $x_2 = \{0, 0.15\}$ [m]

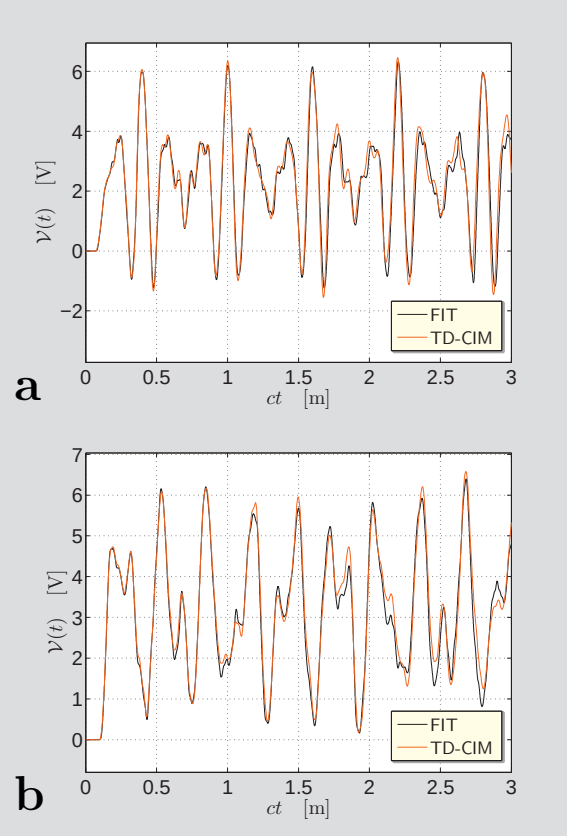

Figure 3.7: The pulsed voltage evaluated using the proposed TD-CIM and the referential FIT as observed at the (a) probe shown in Fig. 3.6a; (b) probe shown in Fig. 3.6b.

only and not along the cuts $\{0.05 \leq x_1 \leq 0.10, x_2 = 0.1\}$ [m] and $\{x_1 = 0.05, 0.10 \leq x_2 \leq 0.15\}$ [m].

3.5 Conclusions

Starting from the reciprocity-based contour-integral formulation, the Time-Domain Contour-Integral Method (TD-CIM) has been formulated. It has been demonstrated that this approach results in a stable step-by-step updating scheme that readily yields the desired space-time field distribution along the circuit's rim.

Furthermore, the introduced computational procedure has been validated with the help of the eigenfunction expansion method applied to a loss-free rectangular planar circuit as well as with the aid of FIT applied to an

irregularly-shaped planar circuit. TD-CIM may find its applications in TD modeling of various double-plane circuit topologies including passive planar circuits and thin microstrip antennas and in solving related signal/power integrity issues in multilayered PCBs. Several extensions and applications of the introduced TD-CIM will be closely described in the following chapters.

Chapter 4

Relation to the classic CIM

The FD Contour-Integral Method (CIM) is a well-established numerical technique for the efficient analysis of planar circuits of arbitrary shape [67, 69]. Thanks to its simplicity and versatility, the method is applicable to signal and power integrity analysis of complex high-speed multilayered PCBs, for which it readily provides their parallel-plate impedances [82, 119], as well as to tackling closely related EMI issues [28, 115].

The CIM formulation is based on a classic 2D contour-integral representation for cylindrical waves (e.g. [69, Eq. (3)]). This integral relation is traditionally solved upon applying the point-matching procedure [36, Sec. 1-4] along with the piecewise-constant field expansion over each of (relatively small) line segments approximating the circuit's rim. This choice of testing and expansion functions leads to an impedance matrix describing the self- and mutual interactions between the dividing segments, whose elements are easy to calculate [69, Eqs. (14)–(15)]. On the other hand, the point-matching solution may not converge to the actual solution. A straightforward way that may improve the convergence of the method is to employ the rectangular testing functions. Introducing such a numerical solution is exactly the main objective of this chapter[1].

The following sections are organized as follows. Adopting the problem configuration from the previous Chapter 3, this chapter starts by interrelating the complex-FD reciprocity-based formulation with the classic formulation of CIM as introduced by Okoshi [69]. In Sec. 4.2, the relevant integral equation is solved with the aid of the point-matching procedure. Subsequently in Sec. 4.3, the point-matching solution is generalized upon 'weighting' the integral equation with the sequence of rectangular testing functions. Finally, numerical examples that illustrate convergence properties of the numerical

[1]This chapter is largely based on Reference [113]. The permission to reuse the material originally published in the Radioengineering journal is gratefully acknowledged.

solutions are presented in Sec. 4.4.

4.1 Basic CIM formulation

To arrive at the classic CIM formulation, the testing electric-current surface density is chosen to show the Dirac-delta behavior, i.e. we substitute $\partial\hat{J}_3^B(\boldsymbol{x}|\boldsymbol{x}^S,s)=\delta(\boldsymbol{x}-\boldsymbol{x}^S)$ in Eq. (3.1) and get

$$\hat{E}_3(\boldsymbol{x}^S,s)=(s/c\pi)\int_{\boldsymbol{x}\in\partial\Omega}\hat{E}_3(\boldsymbol{x},s)\mathrm{K}_1\left[sr(\boldsymbol{x}|\boldsymbol{x}^S)/c\right]\cos[\theta(\boldsymbol{x}|\boldsymbol{x}^S)]\mathrm{d}l(\boldsymbol{x}) + (s\mu/\pi)\int_{\boldsymbol{x}\in\partial\mathcal{S}}\boldsymbol{\nu}(\boldsymbol{x})\cdot\partial\hat{\boldsymbol{J}}(\boldsymbol{x},s)\mathrm{K}_0\left[sr(\boldsymbol{x}|\boldsymbol{x}^S)/c\right]\mathrm{d}l(\boldsymbol{x}) \tag{4.1}$$

for $\boldsymbol{x}^S\in\partial\Omega$. Note that this choice of the impulsive testing source is known as the point-matching procedure. Next, taking the limit $\{s=\delta+\mathrm{i}\omega,\delta\downarrow 0,\omega\in\mathbb{R}\}$, the integral equation can be re-written in the real-FD, viz

$$\hat{V}(\boldsymbol{x}^S,\mathrm{i}\omega)=(k/2\mathrm{i})\int_{\boldsymbol{x}\in\partial\Omega}\hat{V}(\boldsymbol{x},\mathrm{i}\omega)\mathrm{H}_1^{(2)}\left[kr(\boldsymbol{x}|\boldsymbol{x}^S)\right]\cos[\theta(\boldsymbol{x}|\boldsymbol{x}^S)]\mathrm{d}l(\boldsymbol{x}) - (\omega\mu d/2)\int_{\boldsymbol{x}\in\partial\mathcal{S}}\boldsymbol{\nu}(\boldsymbol{x})\cdot\partial\hat{\boldsymbol{J}}(\boldsymbol{x},\mathrm{i}\omega)\mathrm{H}_0^{(2)}\left[kr(\boldsymbol{x}|\boldsymbol{x}^S)\right]\mathrm{d}l(\boldsymbol{x}) \tag{4.2}$$

for $\boldsymbol{x}^S\in\partial\Omega$, where $\hat{V}=-d\hat{E}_3$, $k=\omega/c$. In Eq. (4.2) we have used [1, (9.6.4)] to express the modified Bessel functions with the complex argument using the Hankel functions of the second kind.

In the following sections, the integral equation (4.2) is solved numerically. To this end, the circuit's rim is first approximated by a set of line segments $\partial\Omega\simeq\cup_{m=1}^{N}\triangle\Omega^{[m]}$ (see Fig. 3.1). Subsequently, upon employing the piecewise-constant expansion, the equation is cast into its matrix form, i.e.

$$\boldsymbol{U}\cdot\boldsymbol{V}=\boldsymbol{H}\cdot\boldsymbol{I} \tag{4.3}$$

in which $\boldsymbol{V}$ is the voltage 1D-array of $[N\times 1]$ (unknown) coefficients, $\boldsymbol{I}$ is the electric-current 1D-array of $[N\times 1]$ (prescribed) excitation coefficients and $\boldsymbol{U}$ and $\boldsymbol{H}$ are $[N\times N]$ 2D-arrays. Clearly, the corresponding $[N\times N]$ impedance matrix directly follows from Eq. (4.3) as $\boldsymbol{Z}=\boldsymbol{U}^{-1}\cdot\boldsymbol{H}$.

4.2 Point-matching solution

In the first step, the unknown voltage distribution along the approximated circuit's periphery is expanded in terms of the rectangular functions (see

Eq. (2.44)), i.e.

$$\hat{V}(\boldsymbol{x}, \mathrm{i}\omega) = \sum_{m=1}^{N} \hat{v}^{[m]} \Pi^{[m]}(\boldsymbol{x}) \tag{4.4}$$

where $\hat{v}^{[m]}$ are the expansion coefficients of vector $\boldsymbol{V}$. Upon enforcing the equality in Eq. (4.2) at isolated points located at the centers of the dividing segments denoted by $\boldsymbol{x}^{[m;c]}$ for $m = \{1, \cdots, N\}$ we end up with (cf. [69, Sec. III] and [67, Eq. (3.26)])

$$(\boldsymbol{U})_{S,m} = -\left(k\triangle\Omega^{[m]}/2\mathrm{i}\right) \mathrm{H}_1^{(2)}\left[kr(\boldsymbol{x}^{[m;c]}|\boldsymbol{x}^{[S;c]})\right] \cos\left[\theta(\boldsymbol{x}^{[m;c]}|\boldsymbol{x}^{[S;c]})\right] \tag{4.5}$$

$$(\boldsymbol{H})_{S,m} = (\omega\mu d/2)\mathrm{H}_0^{(2)}\left[kr(\boldsymbol{x}^{[m;c]}|\boldsymbol{x}^{[S;c]})\right] \tag{4.6}$$

for all $S \neq m$ and

$$(\boldsymbol{U})_{S,m} = 1 \tag{4.7}$$

$$(\boldsymbol{H})_{S,m} = \frac{\omega\mu d}{2}\left\{1 - \frac{2\mathrm{i}}{\pi}\left[\ln\left(\frac{k\triangle\Omega^{[m]}}{4}\right) - 1 + \gamma\right]\right\} \tag{4.8}$$

for all $S = m$. The latter expression has been found using the small-argument expansion of the Hankel function [1, Eq. (9.1.8)]

$$\mathrm{H}_0^{(2)}(x) = (2\mathrm{i}/\pi)\ln(2/x) - (2\mathrm{i}/\pi)\gamma + 1 + \mathcal{O}(x^2) \text{ as } x \downarrow 0 \tag{4.9}$$

and the following integral (cf. Appendix A)

$$\int_{\lambda=0}^{1} \ln[|(1-\lambda)(-\triangle\Omega/2) + \lambda\triangle\Omega/2|] = \ln(\triangle\Omega/2) - 1 \tag{4.10}$$

for $\{\triangle\Omega \in \mathbb{R}; \triangle\Omega > 0\}$. A sample MATLAB® implementation of the point-matching solution can be found in Sec. C.1.1.

4.3 Pulse-matching solution

Instead of applying the point-matching procedure we can start over with the real-FD version of the reciprocity-based relation (3.1) and associate the corresponding testing-source density with the rectangular function, i.e. we let $\partial\hat{J}_3^B(\boldsymbol{x}|\boldsymbol{x}^S, s) = \Pi^{[S]}(\boldsymbol{x})$. This choice in combination with the piecewise-constant expansion (4.4) leads to the system of algebraic equations (4.3)

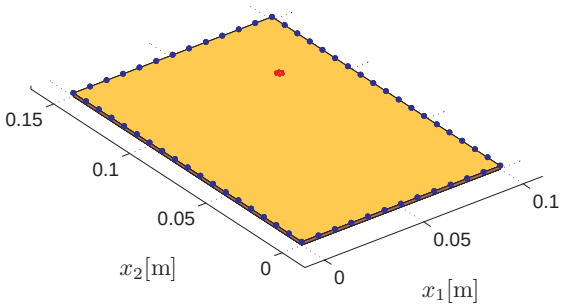

Figure 4.1: Computational model of the analyzed rectangular circuit with a vertical excitation port (the dots on the patch).

with

$$(\boldsymbol{U})_{S,m} = -\left(k\triangle\Omega^{[m]}/2\mathrm{i}\right)\int_{\lambda=0}^{1}\mathrm{d}\lambda\int_{\lambda^T=0}^{1}\mathrm{H}_1^{(2)}\left\{kr[\boldsymbol{x}(\lambda)|\boldsymbol{x}^T(\lambda^T)]\right\}\cos\left\{\theta[\boldsymbol{x}(\lambda)|\boldsymbol{x}^T(\lambda^T)]\right\}\mathrm{d}\lambda^T \tag{4.11}$$

$$(\boldsymbol{H})_{S,m} = (\omega\mu d/2)\int_{\lambda=0}^{1}\mathrm{d}\lambda\int_{\lambda^T=0}^{1}\mathrm{H}_0^{(2)}\left\{kr[\boldsymbol{x}(\lambda)|\boldsymbol{x}^T(\lambda^T)]\right\}\mathrm{d}\lambda^T \tag{4.12}$$

in which

$$\boldsymbol{x}(\lambda) = \boldsymbol{x}^{[m]} + \lambda\left(\boldsymbol{x}^{[m+1]} - \boldsymbol{x}^{[m]}\right) \in \triangle\Omega^{[m]} \tag{4.13}$$

$$\boldsymbol{x}^T(\lambda^T) = \boldsymbol{x}^{[S]} + \lambda^T\left(\boldsymbol{x}^{[S+1]} - \boldsymbol{x}^{[S]}\right) \in \triangle\Omega^{[S]} \tag{4.14}$$

for all $S \neq m$. Similarly to the previous section, the diagonal terms are handled analytically. In this way, we after a few steps of algebra obtain

$$(\boldsymbol{U})_{S,m} = 1 \tag{4.15}$$

$$(\boldsymbol{H})_{S,m} = \frac{\omega\mu d}{2}\left\{1 - \frac{2\mathrm{i}}{\pi}\left[\ln\left(\frac{k\triangle\Omega^{[m]}}{2}\right) - \frac{3}{2} + \gamma\right]\right\} \tag{4.16}$$

for all $S = m$. Finally it is noted that Eqs. (4.5)–(4.6) can be understood as a special case of (4.11)–(4.12) to which the 1-point Gaussian quadrature (see [1, Eq. (25.4.30)]) is applied. A sample MATLAB® implementation of the pulse-matching solution can be found in Sec. C.1.2.

4.4 Numerical results

In this section we shall analyze a rectangular planar circuit of dimensions $L = 0.10\,[\mathrm{m}]$ and $W = 0.15\,[\mathrm{m}]$ (see Fig. 4.1). The thickness of the planar circuit

is $d = 1.50\,[\mathrm{mm}]$. The dielectric filling is described by its electric permittivity $\epsilon = 4.50\,\epsilon_0$ and magnetic permeability $\mu = \mu_0$. The corresponding EM wave speed in the dielectric layer is $c = (\epsilon\mu)^{-1/2}$. The circuit is assumed to show low losses such that the corresponding (complex-valued) wavenumber k can be approximated according to [67, Sec. 2.2.1]

$$k \simeq (\omega/c)\left\{1 + \left[\tan(\delta) + \delta_s/d\right]/2\mathrm{i}\right\} \tag{4.17}$$

where the dielectric loss is accounted for via $\tan(\delta) = 0.0045$, the skin depth of the conductor is found from $\delta_s = \sqrt{2/\omega\mu\sigma}$ with conductivity $\sigma = 5.80 \cdot 10^7\,[\mathrm{S/m}]$. The planar circuit is activated using the excitation vertical port that has its center at $\{x_1^S, x_2^S\} = \{0.075, 0.1125\}\,[\mathrm{m}]$. The CIM model of the port has a hexagonal cross-section of circumradius $1.50\,[\mathrm{mm}]$. All the calculations that follow are performed in the frequency range $\{50 \leq f = \omega/2\pi \leq 2000\}\,[\mathrm{MHz}]$ at 200 uniformly-spaced frequency points. The circuit's boundary is discretized such that $\max_n(|\triangle\Omega^{[n]}|) < 0.12\,c/\max(f)$. The integrations in Eqs. (4.11) and (4.12) are carried out using the Gauss-Legendre quadrature, symbolically written as

$$\int_{\lambda=0}^{1} f(\lambda)\mathrm{d}\lambda \simeq \sum_{k=1}^{K} w_k f(\lambda_k) \tag{4.18}$$

where the corresponding abscissas λ_k and weights w_k for $\{0 \leq \lambda \leq 1\}$, $K = \{1, \ldots, 8\}$ of the quadrature can be found in [1, p. 921], for example. Recall that for $K = 1$ for which $w_1 = 1$, $\lambda_1 = 1/2$, Eqs. (4.11)–(4.12) become fully equivalent to Eqs. (4.5)–(4.6). For validation purposes, the input impedance is also evaluated using a special case of the double-summation formula (3.18), namely

$$\hat{Z}(\mathrm{i}\omega) = \frac{\mathrm{i}\omega\mu d}{LW} \lim_{M,N\to\infty} \sum_{m=0}^{M}\sum_{n=0}^{N} \frac{e_m^2 e_n^2}{k_m^2 + k_n^2 - k^2} F_{mn}^S F_{mn}^P \tag{4.19}$$

with $F_{mn}^S = F_{mn}^P$, where

$$F_{mn}^S = \cos(k_m x_1^S)\cos(k_n x_2^S)\mathrm{sinc}(k_m W_1^S/2)\mathrm{sinc}(k_n W_2^S/2) \tag{4.20}$$

where we take $W_1^S = W_2^S = 1.0\,[\mathrm{mm}]$. In the actual calculations, the summations in Eq. (4.19) are truncated to $N = M = 1000$.

The results are summarized in Fig. 4.2. In Figs. 4.2a and 4.2b we have shown the point-matching and pulse-matching solutions, respectively, together with the FD response calculated according to the analytical solution (4.19). As can be observed, the both CIM-based solutions agree with the

reference well. In order to clearly assess the accuracy of the numerical solutions, the absolute error of the calculated input impedance with respect to the referential solution (4.19) has been plotted in Fig. 4.2c. Apparently, the calculated error curves attain their peak values at the circuit's resonance frequencies. Comparing the point-matching and pulse-matching approaches, the latter solution leads, except for the very high-frequency part of the frequency range, to more accurate results. The difference is most evident at low frequencies. Finally it has been observed that doubling the number of the integration from $K = 6$ to $K = 12$ does not imply a significant improvement. For a related study on the impact of the width of rectangular testing functions on such numerical results' accuracy we refer the reader to [55, Sec. 5.2.2].

4.5 Conclusions

In this chapter, we have demonstrated the link between the reciprocity-based relation given in Chapter 3 and the classic real-FD CIM formulation. The resulting integral equation has been then solved for two different sequences of the testing-source density. In this respect, it has been shown that the classic point-matching solution can be viewed as a special case of the pulse-matching solution to which the 1-point Gaussian quadrature is applied. With the aid of the analytical solution based on the eigenfunction expansion, it has been finally demonstrated that the pulse-matching solution may provide more accurate results than the classic point-matching one. On the other hand, as the pulse-matching solution requires computation of integrals, one should carefully consider whether the improvement is worth the effort for practical purposes.

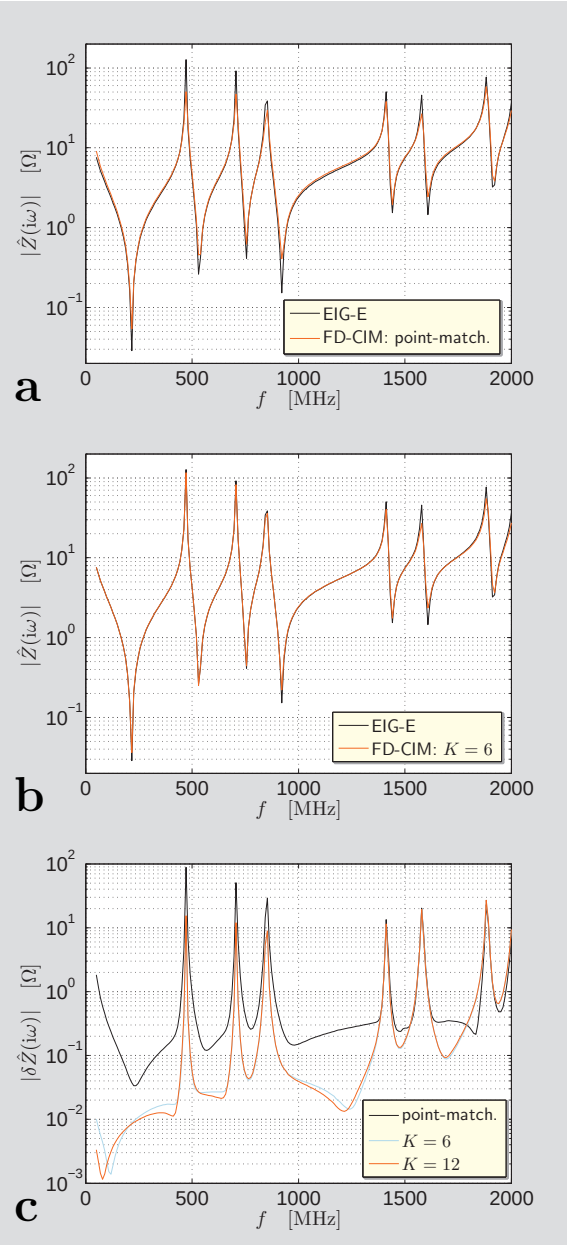

Figure 4.2: Input impedance of the rectangular planar circuit evaluated using FD-CIM and the eigen-function expansion method (EIG-E). (a) Point-matching solution with EIG-E; (b) pulse-matching solution with EIG-E; (c) the absolute error of the FD-CIM solutions with respect to the referential EIG-E solution.

Chapter 5

Rectangular planar circuits with relaxation

The advent of modern high-speed digital interconnect technologies has evoked the need for efficient but still reliable modeling techniques capable of describing transmission of pulsed signals over planar structures. A group of techniques that falls in this category is based on the cavity model that was used in Chapter 3 for TD analysis of instantaneously-reacting, loss-free planar circuits. With still increasing clock speeds and edge rates, however, relaxation mechanisms start to play a significant role with the indispensable impact on the signal transfer [42]. Accordingly, the main concern of this chapter[1] is to provide a modeling technique that allows to analyze the field distribution within a rectangular planar circuit with relaxation behavior in its dielectric filling. To this end, the method of images is combined with a robust numerical inversion of the Laplace transformation. In this way we arrive at a field expansion that can be interpreted as to be composed of 'ray-like' TD constituents propagating via the reflections against circuit's periphery.

The vast majority of previous works on rectangular power-ground structures tackle the problem traditionally in the real-FD [47–49, 100]. Here, two solutions, mutually connected via the Poisson summation formula [121, Sec. 7.5], can be in principle distinguished. The first solution is based on the eigenfunction expansion [47–49], while the second one is represented through the expansion in (source) images [100]. The both FD expansions contain infinite summations and their applicability depends on a frequency range of interest [57, Sec. 7.2]. This feature has advantageous consequences in TD. In particular, the TD image-source expansion shows the property that each

[1] This chapter is largely based on Reference [107]. Adapted with permission from IEEE, © 2014 IEEE.

'higher' constituent appears later then the previous one, which makes possible to account for only a *finite* number of image terms without any loss of accuracy. This fact has been previously recognized in the paper of Parker [71] who introduced closed-form expressions for the TD voltage response of rectangular double-plane structures. The latter work, however, is limited to loss-free structures and to special cases of the excitation pulse shape. Accordingly, the main purpose of this chapter is the construction of novel space-time expressions describing the pulsed-signal transmission over a rectangular planar circuit showing (Boltzmann-type) relaxation in its dielectric filling [107]. The obtained closed-form expressions are physically intuitive, easy-to-implement and may serve for benchmarking of purely numerical techniques.

The present chapter is organized as follows. At first, the relation between the ray-like solution and the 'classical' eigenfunction expansion is discussed for a rectangular circuit with the instantaneously reacting filling. The second part provides a closed-form solution concerning a rectangular circuit whose dielectric losses are included in its electric conductivity. Subsequently, a general technique that makes possible to account for relaxation behavior of the dielectric layer is proposed. Potentialities of the technique are demonstrated on Debije's model of an isotropic dielectric. Finally, the obtained results are validated with the aid of FIT.

5.1 Modal and ray-like TD expansions

The initial-boundary value problem defined in Eqs. (2.1)–(2.4) with (2.6) may be solved analytically in closed form for the planar circuit of rectangular shape with $\Omega = \{\boldsymbol{x} \in \mathbb{R}^2; 0 \leq x_1 \leq L, 0 \leq x_2 \leq W\}$. In such a case one may either apply the separation of variable technique [121, Sec. 4.2] or the method of images [121, Sec. 7.5]. The former leads to the classical eigenfunction expansion discussed in Sec. 2.1.1, while the latter yields the ray-type expansion that can be viewed as a collection of rays propagating via reflections against the circuit periphery. The both approaches are discussed in this section for the impulsive dielectric relaxation function $\kappa(t) = \epsilon\delta(t)$. Incorporation of relaxation effects is addressed in the following sections.

The rectangular circuit as shown in Fig. 5.1 is supposed to be activated via a spatially concentrated electric-current source

$$J_3(\boldsymbol{x}, t) = \mathcal{I}(t)\delta(\boldsymbol{x} - \boldsymbol{x}^S) \tag{5.1}$$

with $\mathcal{I}(t) = 0$ for $t < 0$. Considering a vanishing spatial support of the receiving probe, the excited pulsed voltage response observed at $\boldsymbol{x} = \boldsymbol{x}^P$ can

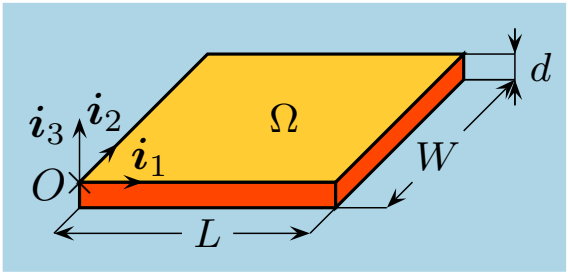

Figure 5.1: Rectangular planar circuit. Taken from [107], with permission from IEEE, © 2014 IEEE.

be written as

$$\mathcal{V}(t) = \mu d \partial_t \mathcal{I}(t) * G(\boldsymbol{x}^P|\boldsymbol{x}^S, t) \tag{5.2}$$

where we have used the results from Sec. 2.1.1. The complex-FD counterpart of the Green's function satisfies the modified Helmholtz equation (2.9) with the Neumann-type boundary condition (2.10). The boundary-value problem has for the given rectangular shape of Ω the closed-form analytical solution that reads (cf. Eq. (2.16))

$$\hat{G}(\boldsymbol{x}|\boldsymbol{x}^S, s) = \frac{1}{LW} \lim_{M,N\to\infty} \sum_{m=0}^{M} \sum_{n=0}^{N} \frac{e_m^2 e_n^2}{k_m^2 + k_n^2 + \hat{\gamma}^2} F_{mn}(\boldsymbol{x}|\boldsymbol{x}^S) \tag{5.3}$$

with

$$F_{mn} = \cos(k_m x_1) \cos(k_n x_2) \cos(k_m x_1^S) \cos(k_n x_2^S) \tag{5.4}$$

where $\hat{\gamma} = s/c$ for the loss-free, instantaneously reacting dielectric layer, $c = (\epsilon\mu_0)^{-1/2}$ and $e_m = 1$ for $m = 0$ and $e_m = \sqrt{2}$ for $m \neq 0$, $k_m = m\pi/L$, $k_n = n\pi/W$. Equation (5.3) can be with the help of [1, (29.3.15)] transformed into TD, which in combination with (5.2) yields

$$\mathcal{V}(t) = \mu d \partial_t \mathcal{I}(t) * \frac{c}{LW} \sum_{m,n} \frac{e_m^2 e_n^2}{(k_m^2 + k_n^2)^{1/2}} F_{mn}(\boldsymbol{x}^P|\boldsymbol{x}^S) \sin\left[ct(k_m^2 + k_n^2)^{1/2}\right] \mathrm{H}(t) \tag{5.5}$$

where we have used the shorthand notation for the double sum in (5.3). The lowest-order term $m = n = 0$ requires a special attention and follows as

$$\mathcal{V}^{[0,0]}(t) = (d/\epsilon LW) \int_{\tau=0}^{t} \mathcal{I}(\tau) \mathrm{d}\tau \tag{5.6}$$

which clearly represents the charge accumulation on a parallel-plate capacitor.

An alternative solution relies on the method of images. In this method, the total solution $G(.)$ is composed of the fundamental solution $G_\infty(.)$ satisfying the wave equation with the causality condition and of a secondary part that is adjusted such that $G(.)$ satisfies the (Neumann) boundary condition along $\partial\Omega$. In this way we arrive at

$$\begin{aligned}\mathcal{V}(t) = \mu d \partial_t \mathcal{I}(t) * \sum_{p=-P}^{P} \sum_{q=-Q}^{Q} \\ \big\{ G_\infty(x_1^P | x_1^S + 2pL, x_2^P | x_2^S + 2qW, t)|_{++} \\ + G_\infty(x_1^P | x_1^S + 2pL, x_2^P | 2qW - x_2^S, t)|_{+-} \\ + G_\infty(x_1^P | 2pL - x_1^S, x_2^P | x_2^S + 2qW, t)|_{-+} \\ + G_\infty(x_1^P | 2pL - x_1^S, x_2^P | 2qW - x_2^S, t)|_{--} \big\}\end{aligned} \tag{5.7}$$

where

$$G_\infty(x_1^P | x_1^S, x_2^P | x_2^S, t) = (1/2\pi)(t^2 - r^2/c^2)^{-1/2} \mathrm{H}(t - r/c) \tag{5.8}$$

is the lossless two-dimensional fundamental solution and $r = r(\boldsymbol{x}^P | \boldsymbol{x}^S)$ denotes the Eucledian distance between the source and field points

$$r(\boldsymbol{x}^P | \boldsymbol{x}^S) = \left[(x_1^P - x_1^S)^2 + (x_2^P - x_2^S)^2 \right]^{1/2} \tag{5.9}$$

Upon inspection of (5.7) with (5.8) we may identify the arrival times of the corresponding TD constituents, viz

$$c\,T_{++}^{[pq]} = \left[(x_1^P - x_1^S - 2pL)^2 + (x_2^P - x_2^S - 2qW)^2 \right]^{1/2} \tag{5.10}$$

$$c\,T_{+-}^{[pq]} = \left[(x_1^P - x_1^S - 2pL)^2 + (x_2^P + x_2^S - 2qW)^2 \right]^{1/2} \tag{5.11}$$

$$c\,T_{-+}^{[pq]} = \left[(x_1^P + x_1^S - 2pL)^2 + (x_2^P - x_2^S - 2qW)^2 \right]^{1/2} \tag{5.12}$$

$$c\,T_{--}^{[pq]} = \left[(x_1^P + x_1^S - 2pL)^2 + (x_2^P + x_2^S - 2qW)^2 \right]^{1/2} \tag{5.13}$$

From Eqs. (5.10)–(5.13) it is immediately clear that the arrival times increase with $|p| + |q|$ that is proportional to the number of reflections against the circuit's edges. Consequently, the TD constituents in (5.7) arrive at the field point in a successive manner and hence, in any finite time window of observation, only a finite number of them is necessary to build the exact solution up. On the other hand, the situation is very different for the modal expansion (5.5). In it, all the modal constituents start at the same instant

$t = 0$ and to obtain the exact solution one would need to include an unlimited number of them. In practice, of course, their number is always truncated once the prescribed precision is reached. Further properties of the modal and ray-like expansions shall be discussed in Sec. (5.4). For related works on the subject we refer the reader to [105, 116].

5.2 Conduction-loss dielectric relaxation

The simplest way to model a lossy dielectric compatible with the property of causality is to specify its relative permittivity ϵ_r and electric conductivity σ. The corresponding dielectric relaxation function has then the following form

$$\kappa(t) = \epsilon_0[\epsilon_\mathrm{r}\delta(t) + (\sigma/\epsilon_0)\mathrm{H}(t)] \tag{5.14}$$

The presence of non-zero conducting current in (2.1) manifests itself by a diffusive term in the corresponding dissipative wave equation

$$(\partial_1^2 + \partial_2^2)G_\infty - c^{-2}(\partial_t^2 + \tau_\mathrm{c}^{-1}\partial_t)G_\infty = -\delta(\boldsymbol{x} - \boldsymbol{x}^S)\delta(t) \tag{5.15}$$

that is solved for $\boldsymbol{x} \in \mathbb{R}^2$ and $t > 0$ together with the zero initial conditions and the condition of causality. Here, $\tau_\mathrm{c} = \epsilon/\sigma$ is the conduction relaxation time and $c = (\epsilon_\mathrm{r}\epsilon_0\mu_0)^{-1/2}$ is the corresponding wave speed. To solve Eq. (5.15) analytically, one may either apply the extended Cagniard-DeHoop method [21] or start with the solution of the three-dimensional dissipative wave equation [20, Sec. 26.5] and apply Hadamard's method of descent [13, III -§4.4]. The latter procedure was used in [57, Sec. 7.4], for instance. Based on the results given in Appendix F, the fundamental solution is written as (cf. Eq. (F.12))

$$\begin{aligned} G_\infty(x_1^P|x_1^S, x_2^P|x_2^S, t) &= (1/2\pi)(t^2 - r^2/c^2)^{-1/2}\mathrm{H}(t - r/c) \\ &\left\{1 + 2\sinh^2\left[(t^2 - r^2/c^2)^{1/2}/4\tau_\mathrm{c}\right]\right\}\exp(-t/2\tau_\mathrm{c}) \end{aligned} \tag{5.16}$$

Obviously, Eq. (5.8) is a special case of (5.16) for $\sigma = 0$. Its first part represents an attenuated fundamental solution of the loss-free two-dimensional wave equation, while the second part represents a dispersive contribution introduced by the diffusive term in (5.15). Finally, the total electric field follows upon substituting of (5.16) in (5.7).

5.3 Debije's dielectric relaxation

Relaxation behavior of an isotropic dielectric slab may be modeled via the first-order Debije model (see [39, Sec. 8.4], for example). The corresponding

dielectric relaxation function has the following form

$$\kappa(t) = \epsilon_0\{\epsilon_\infty\delta(t) + [(\epsilon_\mathrm{r} - \epsilon_\infty)/\tau_\mathrm{r}]\exp(-t/\tau_\mathrm{r})\mathrm{H}(t)\} \tag{5.17}$$

where ϵ_r and ϵ_∞ are the characteristic relative permittivities for which $0 < \epsilon_\infty < \epsilon_\mathrm{r}$ and τ_r is the relaxation time. The corresponding wave equation then reads (cf. Eq. (H.1))

$$(\partial_1^2 + \partial_2^2)G_\infty - c_\infty^{-2}\partial_t^2\Big\{G_\infty + (\epsilon_\mathrm{r}/\epsilon_\infty - 1)\tau_\mathrm{r}^{-1} \int_{\tau=-\infty}^{t} \exp[-(t-\tau)/\tau_\mathrm{r}]G_\infty(\boldsymbol{x},\tau)\mathrm{d}\tau\Big\} = -\delta(\boldsymbol{x} - \boldsymbol{x}^S)\delta(t) \tag{5.18}$$

where $c_\infty = (\epsilon_\infty\epsilon_0\mu_0)^{-1/2}$. Following the method described in Appendix H, the fundamental solution is expressed as

$$G_\infty(x_1|x_1^S, x_2|x_2^S, t) = \frac{1}{2\pi}\frac{\mathrm{H}(t - r/c_\infty)}{(t^2 - r^2/c_\infty^2)^{1/2}}\exp\left[-(t/2\tau_\mathrm{r})(\epsilon_\mathrm{r} - \epsilon_\infty)\right] + \frac{1}{2\pi}\int_{\tau=r/c_\infty}^{t}\frac{F(t,\tau)\,\mathrm{d}\tau}{(\tau^2 - r^2/c_\infty^2)^{1/2}} \tag{5.19}$$

for $t > \tau$, where the integrated function $F(t,\tau)$ follows from the Bromwich integral

$$F(t,\tau) = \frac{1}{2\pi\mathrm{i}}\int_{s\in\mathcal{B}}\exp(st)\hat{F}(s,\tau)\mathrm{d}s \tag{5.20}$$

where

$$\hat{F}(s,\tau) = \exp\left[-\hat{L}(s)\tau\right] - \exp\left[-\hat{L}_\infty(s)\tau\right] \tag{5.21}$$

$$\hat{L}(s) = s\left[(s+\alpha)/(s+\beta)\right]^{1/2} \tag{5.22}$$

$$\hat{L}_\infty(s) = s + (\alpha - \beta)/2 \tag{5.23}$$

with $\alpha = (\epsilon_\mathrm{r}/\epsilon_\infty)/\tau_\mathrm{r}$ and $\beta = 1/\tau_\mathrm{r}$. Here, where $\hat{L}_\infty(s)$ denotes the leading terms of $\hat{L}(s)$ in the asymptotic expansion as $|s| \to \infty$. The Bromwich integration contour $\mathcal{B}$ in (5.20) runs parallel to $\mathrm{Re}(s) = 0$ and is shifted to the right of all singularities in the complex s-plane. Here, we encounter two algebraic branch points on the negative real axis at $s = \{-\alpha, -\beta\}$. The corresponding branch cuts are chosen such that $\mathrm{Re}[(s+\alpha)^{1/2}] \geq 0$ and $\mathrm{Re}[(s+\beta)^{1/2}] \geq 0$ for all $s \in \mathbb{C}$, which implies two overlapping branch cuts along the negative real axis $\{s \in \mathbb{C}; -\infty < \mathrm{Re}(s) \leq -\alpha, \mathrm{Im}(s) = 0\}$ and

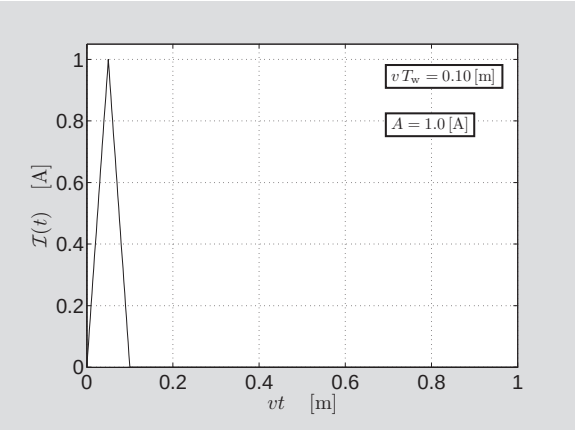

Figure 5.2: The triangular excitation signature.

$\{s \in \mathbb{C}; -\infty < \mathrm{Re}(s) \leq -\beta, \mathrm{Im}(s) = 0\}$. The Bromwich contour is then in virtue of Jordan's lemma closed to the right and the resulting contour is, in view of Cauchy's theorem, contracted to a new contour $\Gamma \cup \Gamma^*$ along which the integral is carried out numerically. For details concerning the hyperbolic contour we refer the reader to Appendix G.

Similarly to the previous section, the fundamental solution (5.19) consists of two parts. The first one is an attenuated two-dimensional Green's function of the corresponding loss-free wave equation and the second one represents the relaxation behavior. The latter part vanishes close to the wavefront at $t = r/c_\infty$, which is in fact a typical feature of dispersive phenomena [31].

5.4 Numerical results

In order to illustrate the application of the results introduced in the previous sections, sample calculations are performed for a rectangular power-ground structure of dimensions $L = 100\,[\rm mm]$ and $W = 75.0\,[\rm mm]$ (see Fig. 5.1). The rectangular circuit is excited by the triangular electric-current pulse (see Fig. 5.2 and Eq. (D.4))

$$\mathcal{I}(t) = 2A\left[\frac{t}{t_{\rm w}}\mathrm{H}(t) - 2\left(\frac{t}{t_{\rm w}} - \frac{1}{2}\right)\mathrm{H}\left(\frac{t}{t_{\rm w}} - \frac{1}{2}\right) + \left(\frac{t}{t_{\rm w}} - 1\right)\mathrm{H}\left(\frac{t}{t_{\rm w}} - 1\right)\right] \tag{5.24}$$

via a spatially localized vertical port placed at $\{x_1^S, x_2^S\} = \{25.0, 20.0\}\,[\rm mm]$ (see Fig. 5.3). Here, A is the pulse amplitude, $t_{\rm w}$ corresponds to the length

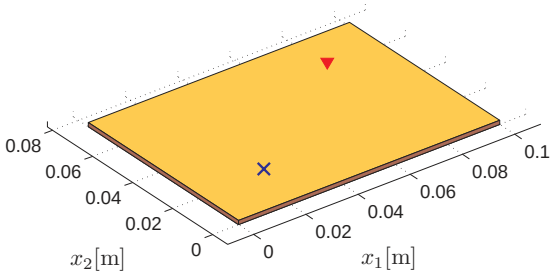

Figure 5.3: Model of the analyzed rectangular planar circuit with a field probe (the solid triangle) and an excitation port (the cross symbol).

of the base and $t_w/2$ is equal to the pulse rise and fall time. For the following examples we take $A = 1.0\,[\mathrm{A}]$ and $v\,t_w = 0.10\,[\mathrm{m}]$. The pulse voltage response is probed at $\{x_1, x_2\} = \{80.0, 60.0\}\,[\mathrm{mm}]$ within the time window of observation $\{0 \leq vt \leq 1.0\}\,[\mathrm{m}]$ (see Fig. 5.3). Here, $v = c = (\epsilon_r \epsilon_0 \mu_0)^{-1/2}$ or $v = c_\infty = (\epsilon_\infty \epsilon_0 \mu_0)^{-1/2}$ for the conduction-loss or Debije dielectric relaxation, respectively.

5.4.1 Modal and ray time-domain constituents

The first example is related to Sec. 5.1 and demonstrates the main features of the modal and ray time-domain expansions. The EM properties of the dielectric layer are described here by its scalar electric permittivity $\epsilon = 4.50\,\epsilon_0$ and magnetic permeability μ_0. Four low-order terms from the right-hand side of Eq. (5.5) are shown in Fig. 5.4a.

As already noted in Sec. 5.1, all the modal constituents start at $t = 0$ and the property of causality turns up once a sufficient number of them is included. For the field evaluation itself it is important to note that as the rate of oscillations increases with the order of the constituents, one may find difficult to evaluate the time convolution with (the time derivative of) the excitation pulse shape for (strongly oscillatory) high-order terms. This is not an issue, however, for special cases of the excitation pulse shape such as the triangular one (5.24), for example, for which the time convolution integral exists in closed form. The pulse shapes of low-order ray constituents as evaluated using Eq. (5.7) are shown in Fig. 5.4b. Here we may observe the direct source/probe wave constituent (++) and the reflected constituents that are associated with the image sources. As can be seen in Fig. 5.4b, all the reflected constituents reach the field point after the direct wave making the evaluated total field strictly causal. This fact is illustrated in Fig. 5.5a,

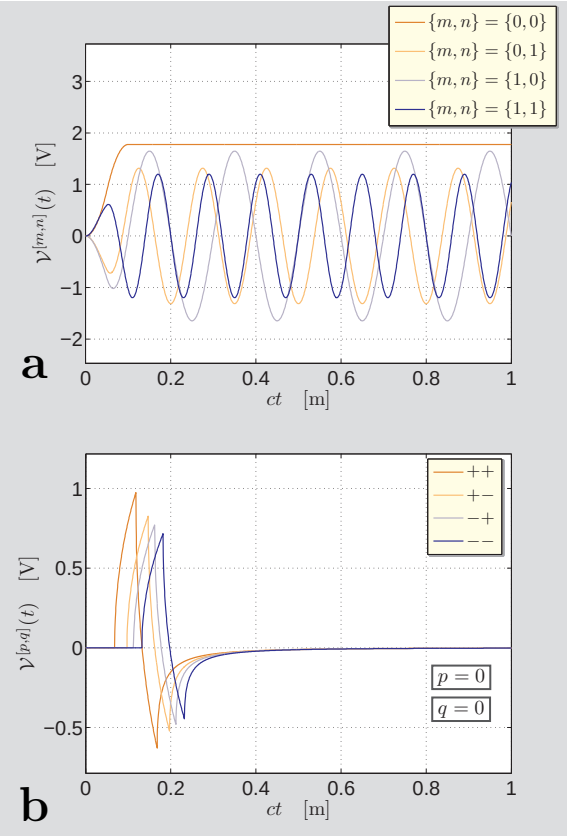

Figure 5.4: Time-domain constituents. (a) The oscillatory modal type; (b) the progressing ray type. From [107], adapted with permission from IEEE, © 2014 IEEE.

where the total field responses, as evaluated using Eq. (5.5) with $M = N = 25$ and Eq. (5.7) with $P = Q = 7$, are compared. While the ray-type expansion already provides the exact results, the modal solution is evidently still missing high-frequency components (see Fig. 5.5b). In this example, the total number of the modal constituents is $M \times N = 625$, while the total number of the ray constituents that appear in the chosen time window is only 423 out of $4 \times (2P + 1) \times (2Q + 1) = 900$.

5.4.2 Inclusion of conduction loss

The second example illustrates the results described in Sec. 5.2. The EM properties of the dielectric slab are described with its scalar electric permittivity $\epsilon = 4.50\,\epsilon_0$, electric conductivity $\sigma = 0.02\,[\mathrm{S/m}]$ and magnetic

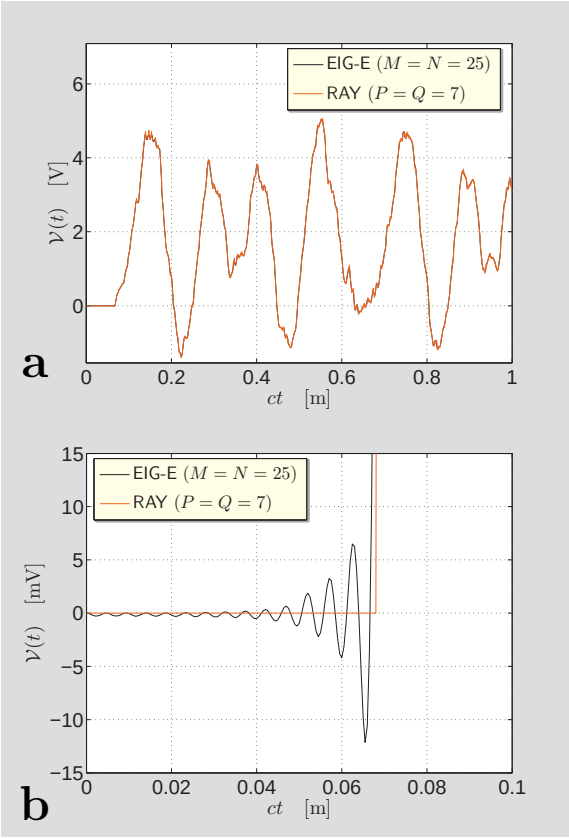

Figure 5.5: The voltage responses represented using (a) the ray-like (RAY) and modal solutions (EIG-E); (b) the early-time part of the responses.

permeability μ_0. The corresponding conduction relaxation time τ_c is a small fraction of the excitation pulse time width $t_w/2$, namely $t_w/\tau_c \simeq 3 \cdot 10^4$.

The following examples were evaluated with the help of Eqs. (5.7) with (5.16) as well as with FIT as implemented in CST Microwave Studio®. In short only, the reference FIT model is placed in homogeneous, isotropic and loss-free ('normal') embedding. The model consists of a homogeneous layer described with the corresponding electric permittivity, electric conductivity, magnetic permeability and its thickness $d = 1.50\,[\mathrm{mm}]$. Note that the layer is very thin with respect to the spatial of the excitation pulse since $d/ct_w = 0.015$. The layer is sandwiched between two PEC sheets of vanishing thickness. The model is finely discretized into about 600 of thousands hexahedral mesh cells. Sidewalls of the surrounding box are defined as the magnetic walls with vanishing tangential magnetic-field components. The model is activated through the electric-current discrete port having a van-

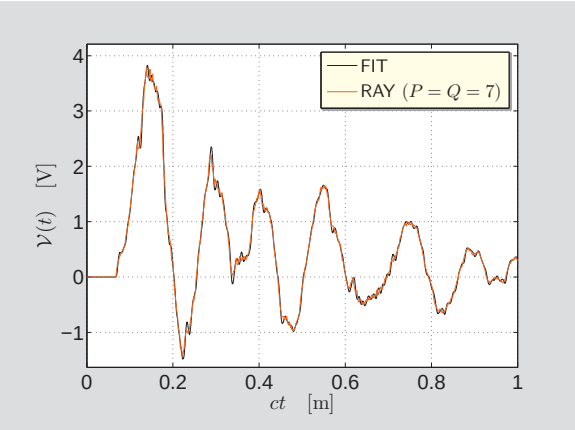

Figure 5.6: The pulsed voltage responses of the circuit with the conductive-loss dielectric relaxation as evaluated using the ray-type expansion (RAY) and the referential FIT.

ishing radius. As can be seen, the corresponding results as shown in Fig. 5.6 agree well. In fact, the ray-type expansion is exact and thus may provide an useful tool for benchmarking purely numerical techniques.

5.4.3 Inclusion of Debije's dielectric relaxation

The last example illustrates the results concerning the Debije relaxation function as described in Sec. 5.3. The following results were evaluated with the help of Eqs. (5.7), (5.19) and again, with FIT as implemented in CST Microwave Studio®. In the first step, the dispersion characteristics of 'FR-4 (lossy)' as defined in the CST Material Library were used to find the parameters of the corresponding dielectric relaxation function (5.17). The corresponding complex (steady-state) dielectric relaxation function reads

$$\mathrm{Re}[\hat{\kappa}(\mathrm{i}\omega)]/\epsilon_0 = \epsilon_\infty + (\epsilon_\mathrm{r} - \epsilon_\infty)/(1 + \omega^2\tau^2) \tag{5.25}$$

$$\mathrm{Im}[\hat{\kappa}(\mathrm{i}\omega)]/\epsilon_0 = (\epsilon_\mathrm{r} - \epsilon_\infty)\omega\tau/(1 + \omega^2\tau^2) \tag{5.26}$$

for $\omega = 2\pi f \in \mathbb{R}$. Its real and imaginary parts for $\epsilon_\mathrm{r} = 4.410$, $\epsilon_\infty = 4.195$ and $\tau_\mathrm{r} = 1.630 \cdot 10^{-11}$ [s] are plotted in Figs. 5.7. In the real-frequency range $f = (0...12)$ [GHz], that covers four main lobes of the amplitude-frequency spectrum of the excitation pulse, the dispersion characteristics are almost identical. Except for the dielectric filling, the FIT model was defined as described in the previous subsection 5.4.2. The corresponding pulsed voltage responses are shown in Fig. 5.8. Again, the observed pulse shapes agree very well thus validating the proposed method.

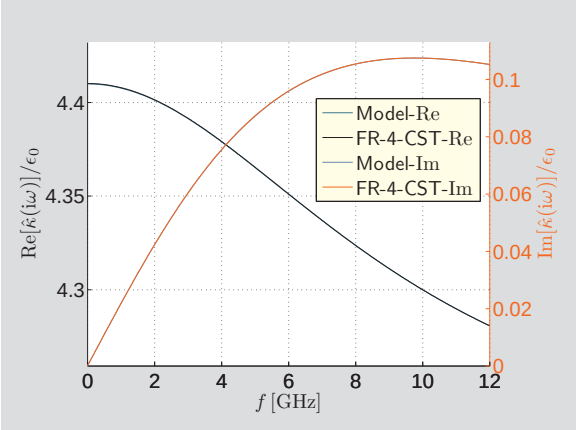

Figure 5.7: Real (Re) and imaginary (Im) parts of the complex dielectric relaxation function related to FR-4. The curves from the implemented model and CST Material Library overlap each other. Taken from [107], with permission from IEEE, © 2014 IEEE.

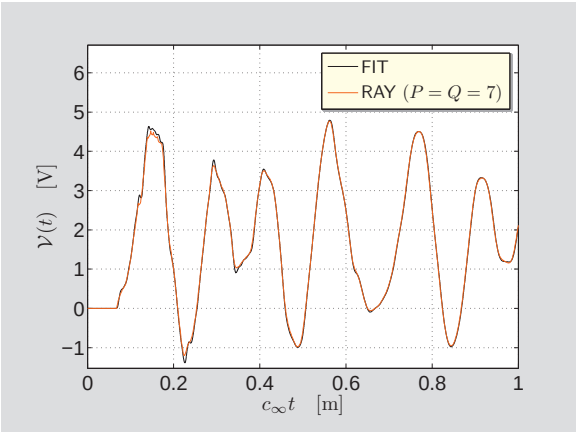

Figure 5.8: The pulsed voltage responses of the circuit with the Debije-dielectric relaxation as evaluated using the ray-type expansion (RAY) and the referential FIT.

5.5 Conclusions

A TD technique for analyzing the pulsed EM-field transmission over a rectangular planar circuit has been described. This technique is based on the method of images and allows for the inclusion of rather general relaxation mechanisms. The TD analysis has been first carried out for the loss-free case demonstrating the main features of the ray-type and modal expansions. Subsequently, two dielectric relaxation models have been analyzed in detail. Namely, we have focused on the conduction-loss and Debije-dielectric relaxation functions for an isotropic dielectric.

The proposed technique is very easy-to-implement, physically intuitive, and in combination with the technique given in Appendix H, it makes possible to account for general (Boltzmann-type) relaxation mechanisms. These properties make the introduced computational model suitable for the fast broadband analysis of rectangular circuits as well as for benchmarking computational techniques such as the TD finite-difference method, for instance.

Chapter 6

Arbitrarily-shaped planar circuits with relaxation

The two-dimensional circuit model with the ideal open-circuit boundary represents a loss-free resonator whose TD response never dies down. In order to set up a more realistic model, one has to account for relaxation and dissipation effects of the dielectric layer. On the other hand, effects of non-perfectly conducting planes can be for practical cases neglected (see [102, Fig. 8]).

Generally speaking, the dissipation and relaxation mechanisms in the FD description manifest themselves by the imaginary part of the wavenumber making their inclusion straightforward [67, Sec. 2.2.1]. As far as the TD analysis is concerned, their inclusion in the TD is much more challenging (see e.g. [33]). In TD, the inclusion of material dissipation and relaxation phenomena changes the form of the field equations and hence the corresponding fundamental solution (see Appendix F). Except for special cases, the time convolutions occurring in the reciprocity relations must be then calculated numerically and the analysis becomes computationally more involved. In this chapter[1] it is demonstrated that a promising way to solve this drawback is the numerical Laplace-transform inversion based on the deformation of the Bromwich contour into a hyperbolic one (see Appendix G). Although the attention is primarily paid to the relaxation behavior of an isotropic dielectric described via the finite-conductivity and Debije-type relaxation models, the proposed modeling techniques are very general and allow to include more complex relaxation behavior such the Lorentzian absorption line, for example. Finally, a few sample calculations are performed and their results are validated using FIT.

[1] This chapter is largely based on Reference [110]. Adapted with permission from IEEE, © 2015 IEEE.

6.1 Inclusion of relaxation behavior

Let us consider a planar circuit activated by the controlled vertical electric-current surface density $\partial\hat{J}_3$ applied to a part of the rim $\partial\mathcal{S} \subset \partial\Omega$. The rest of the circuit periphery forms the perfect magnetic wall to which the explicit-type boundary condition (2.6) applies. The corresponding reciprocity-integral relation has then the following form (cf. Eq. (3.1))

$$\begin{aligned}
&\int_{\boldsymbol{x}\in\partial\Omega} \hat{E}_3(\boldsymbol{x},s)\partial\hat{J}_3^B(\boldsymbol{x}|\boldsymbol{x}^S,s)\mathrm{d}l(\boldsymbol{x}) \\
&= [\hat{\gamma}(s)/\pi] \int_{\boldsymbol{x}\in\partial\Omega} \hat{E}_3(\boldsymbol{x},s) \int_{\boldsymbol{x}^T\in\partial\Omega} \mathrm{K}_1\left[\hat{\gamma}(s)r(\boldsymbol{x}|\boldsymbol{x}^T)\right] \\
&\qquad \partial\hat{J}_3^B(\boldsymbol{x}^T|\boldsymbol{x}^S,s)\cos[\theta(\boldsymbol{x}|\boldsymbol{x}^T)]\mathrm{d}l(\boldsymbol{x}^T)\mathrm{d}l(\boldsymbol{x}) \\
&\quad +(s\mu/\pi) \int_{\boldsymbol{x}\in\partial\mathcal{S}} \partial\hat{J}_3(\boldsymbol{x},s) \int_{\boldsymbol{x}^T\in\partial\Omega} \mathrm{K}_0\left[\hat{\gamma}(s)r(\boldsymbol{x}|\boldsymbol{x}^T)/c\right] \\
&\qquad \partial\hat{J}_3^B(\boldsymbol{x}^T|\boldsymbol{x}^S,s)\mathrm{d}l(\boldsymbol{x}^T)\mathrm{d}l(\boldsymbol{x}) \qquad (6.1)
\end{aligned}$$

where $\hat{\gamma} = \hat{\gamma}(s)$ is the propagation coefficient (see Sec. 2.1.1) that obviously depends on relaxation behavior of the dielectric slab. Besides the instantaneously reacting medium as described in Chapter 3 for which $\hat{\gamma}(s) = s/c$, two other models of an isotropic dielectric are analyzed:

- The finite-conductivity relaxation model defined via its relative electric permittivity ϵ_r with and electric conductivity σ. The corresponding propagation coefficient has the form $\hat{\gamma}(s) = [s(s+\alpha)]^{1/2}/c$ with $c = (\epsilon_\mathrm{r}\epsilon_0\mu_0)^{-1/2}$, where α is related to the conduction relaxation time as $\alpha = 1/\tau_\mathrm{c} = \sigma/\epsilon$.

- The Debije dielectric relaxation model defined via its relative characteristic permittivities ϵ_r and ϵ_∞ and the relaxation time τ_r. The corresponding propagation coefficient has the form $\hat{\gamma}(s) = s[(s+\alpha)/(s+\beta)]^{1/2}/c_\infty$ with $c_\infty = (\epsilon_\infty\epsilon_0\mu_0)^{-1/2}$, where $\alpha = (\epsilon_\mathrm{r}/\epsilon_\infty)/\tau_\mathrm{r}$, $\beta = 1/\tau_\mathrm{r}$.

Details concerning the Laplace inversion are discussed for the both cases in the following subsections.

6.1.1 Conduction-loss dielectric model

The following analysis is carried out for the piecewise linear temporal expansion of the electric field strength (viz Chapter 3). Other types of the time expansion may be readily handled in a similar way. With reference to

Eq. (6.1), the inverse Laplace transformation of the following expressions will be found

$$\hat{\gamma}(s)\mathrm{K}_1[\hat{\gamma}(s)r]/s^2 = [s(s+\alpha)]^{1/2}\mathrm{K}_1\left\{[s(s+\alpha)]^{1/2}r/c\right\}/cs^2 \tag{6.2}$$

$$\mathrm{K}_0[\hat{\gamma}(s)r] = \mathrm{K}_0\left\{[s(s+\alpha)]^{1/2}r/c\right\} \tag{6.3}$$

where $\alpha = \sigma/\epsilon$, $\epsilon = \epsilon_\mathrm{r}\epsilon_0$ and $c = (\epsilon_\mathrm{r}\epsilon_0\mu_0)^{-1/2}$. It is worth to note that as $\sigma \downarrow 0$, one may find the corresponding Laplace inversions analytically with the help of (cf. Eqs. (3.13) and (3.14))

$$\mathcal{L}^{-1}[\mathrm{K}_1(sr/c)/s] = (c^2t^2/r^2 - 1)^{1/2}\mathrm{H}(t - r/c) \tag{6.4}$$

$$\mathcal{L}^{-1}[\mathrm{K}_0(sr/c)] = (t^2 - r^2/c^2)^{-1/2}\mathrm{H}(t - r/c) \tag{6.5}$$

Although the inversion of expressions (6.2) and (6.3) can be in principle carried out analytically with the aid of the Schouten-van-der-Pol theorem [87, 101], the numerical procedure described in Appendix G is, for the sake of generality, applied. To this end, one needs to study the analytical properties of the expressions in the complex s-plane. Here, we encounter two branch points on the negative real axis at $s = \{0, -\alpha\}$ and a (double) pole singularity at $s = 0$ in Eq. (6.2). The corresponding branch cuts are chosen such that $\mathrm{Re}[(s+\alpha)^{1/2}] \geq 0$ and $\mathrm{Re}(s^{1/2}) \geq 0$ for all $s \in \mathbb{C}$, which implies two overlapping branch cuts along the negative real axis $\{s \in \mathbb{C}; -\infty < \mathrm{Re}(s) \leq 0, \mathrm{Im}(s) = 0\}$, $\{s \in \mathbb{C}; -\infty < \mathrm{Re}(s) \leq -\alpha, \mathrm{Im}(s) = 0\}$ together with

$$c\hat{\gamma}(s) = s + \alpha + \mathcal{O}(s^{-1}) \tag{6.6}$$

as $|s| \to \infty$. On account of the large-argument expansions

$$\mathrm{K}_{0,1}(sr/c) = (\pi c/2r)^{1/2}s^{-1/2}\exp(-sr/c)\left[1 + \mathcal{O}(s^{-1})\right] \tag{6.7}$$

as $|s| \to \infty$, the original Bromwich integration contour can be closed to the right for $t > r/c$ and the corresponding integration is in view of Cauchy's theorem carried out along the hyperbolic contour $\Gamma \cup \Gamma^*$ (here * denotes complex conjugate) sketched in Fig. 6.1. Here, only the non-overlapping part of the branch cuts is depicted. For further details concerning the numerical integration along the hyperbolic contour we refer the reader to Appendix G.

Finally, the unknown expansion coefficients follow upon solving Eq. (3.8) provided that the integrated functions ψ and Φ defined in Eqs. (3.13) and (3.14) are replaced by their corresponding (numerical) inversions

$$\psi(r,t) = \mathcal{L}^{-1}\Big\{[s(s+\alpha)]^{1/2}\mathrm{K}_1\left\{[s(s+\alpha)]^{1/2}r/c\right\}/s^2\Big\} \tag{6.8}$$

$$\Phi(r,t) = -\mu\partial_t\mathcal{I}(t) * \mathcal{L}^{-1}\Big\{\mathrm{K}_0\left\{[s(s+\alpha)]^{1/2}r/c\right\}\Big\} \tag{6.9}$$

for $t > r/c$.

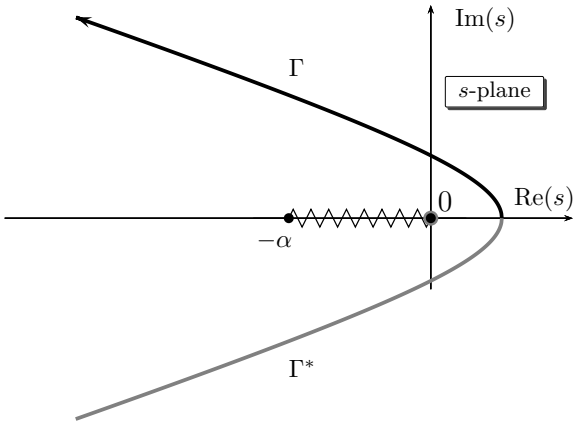

Figure 6.1: Complex s-plane related to the finite-conductivity model. Taken from [110] with permission from IEEE, © 2015 IEEE.

6.1.2 Debije dielectric model

As in the previous subsection 6.1.1, the following considerations are related to the piecewise linear temporal expansion. Again, with reference to Eq. (6.1), the inverse Laplace transformation of the following expressions will be found (cf. Eqs. (6.2) and (6.3))

$$\hat{\gamma}(s)\mathrm{K}_1[\hat{\gamma}(s)r]/s^2 = s[(s+\alpha)/(s+\beta)]^{1/2} \mathrm{K}_1\left\{s[(s+\alpha)/(s+\beta)]^{1/2}r/c_\infty\right\}/c_\infty s^2 \tag{6.10}$$

$$\mathrm{K}_0[\hat{\gamma}(s)r] = \mathrm{K}_0\left\{s[(s+\alpha)/(s+\beta)]^{1/2}r/c_\infty\right\} \tag{6.11}$$

Since no straightforward closed-form inversion of (6.10) and (6.11) does exist, the numerical technique as described in Appendix G is applied. In the corresponding complex s-plane we encounter two branch points at $s = \{-\alpha, -\beta\}$ and a double pole at $s = 0$ in Eq. (6.10). Also, the corresponding propagation coefficient $\hat{\gamma}$ shows the inverse-square root singularity at $s = -\beta$ causing that Eq. (6.10) is unbounded there. The corresponding branch cuts are chosen such that $\mathrm{Re}[(s+\alpha)^{1/2}] \geq 0$ and $\mathrm{Re}[(s+\beta)^{1/2}] \geq 0$ for all $s \in \mathbb{C}$, which implies two overlapping branch cuts along the negative real axis $\{s \in \mathbb{C}; -\infty < \mathrm{Re}(s) \leq -\alpha, \mathrm{Im}(s) = 0\}$, $\{s \in \mathbb{C}; -\infty < \mathrm{Re}(s) \leq -\beta, \mathrm{Im}(s) = 0\}$ together with

$$c_\infty \hat{\gamma}(s) = s + (\alpha - \beta)/2 + \mathcal{O}(s^{-1}) \tag{6.12}$$

as $|s| \to \infty$. Based on the large-argument expansions (6.7), the Bromwich inversion contour can be closed to the right for $t > r/c_\infty$ and the corresponding

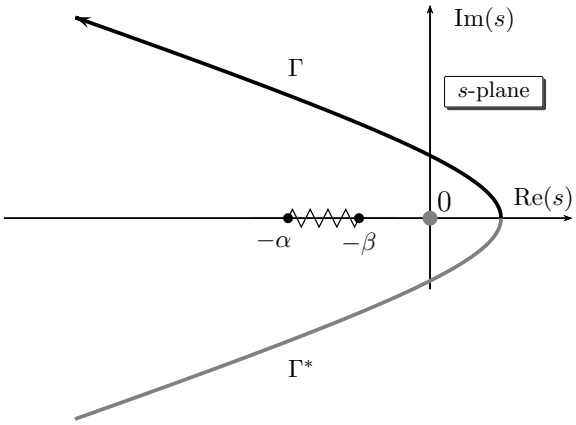

Figure 6.2: Complex s-plane related to the Debije model. Taken from [110] with permission from IEEE, © 2015 IEEE.

integration is in view of Cauchy's theorem carried out along the hyperbolic contour $\Gamma \cup \Gamma^*$ (here * denotes complex conjugate) shown in Fig. 6.2. Owing to the inverse square-root singularity affecting the inversion of Eq. (6.10), the new integration path should not be too close to the singularity at $s = -\beta$. In Fig. 6.2, only the non-overlapping part of the branch cuts is shown. For further details concerning the numerical integration along the hyperbolic contour we refer the reader to Appendix G.

Finally, the unknown expansion coefficients follow upon solving (3.8) provided that the integrated functions ψ and Φ defined in Eqs. (3.13) and (3.14) are replaced by their corresponding (numerical) inversions

$$\psi(r,t) = \mathcal{L}^{-1}\Big\{ s[(s+\alpha)/(s+\beta)]^{1/2} \\ \mathrm{K}_1\left\{ s[(s+\alpha)/(s+\beta)]^{1/2} r/c_\infty \right\} / s^2 \Big\} \tag{6.13}$$

$$\Phi(r,t) = -\mu \partial_t \mathcal{I}(t) * \mathcal{L}^{-1}\Big\{ \mathrm{K}_0\left\{ s[(s+\alpha)/(s+\beta)]^{1/2} r/c_\infty \right\} \Big\} \tag{6.14}$$

for $t > r/c_\infty$.

6.2 Numerical results

This section is divided into two parts and presents sample numerical calculations concerning the inclusion of the dielectric Boltzmann-type relaxation mechanisms via the finite-conductivity and Debije-type models. All the obtained results are compared with the corresponding results evaluated using FIT of CST Microwave Studio®.

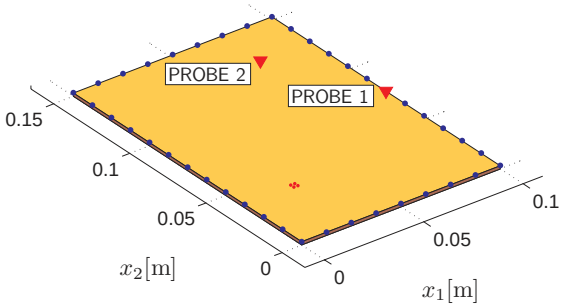

Figure 6.3: Computational model of the analyzed circuit with probes (the solid triangles) and a vertical excitation port (the dots on the patch).

6.2.1 Inclusion of conduction loss

The present subsection is related to Sec. 6.1.1 and provides a sample numerical result concerning a rectangular planar circuit with the conductive and dielectric filling and with the perfect magnetic wall along its rim. The EM properties of the slab are now defined via its electric permittivity $\epsilon = 2.50\epsilon_0$ and electric conductivity $\sigma = 0.02\,[\mathrm{m}]$. Its thickness is again $d = 1.50\,[\mathrm{mm}]$. The model of the circuit as used for the TD-CIM simulation is shown in Fig. 6.3.

As the excitation pulse we take, again, the waveform shown in Fig. 3.3. The structure is activated via a vertical cylindrical port of radius $1.0\,[\mathrm{mm}]$ with its center placed at $\{x_1^S, x_2^S\} = \{0.0250, 0.0375\}\,[\mathrm{m}]$. The time-domain electric-field response is probed at (a) $\{x_1^P, x_2^P\} = \{0.100, 0.075\}\,[\mathrm{m}]$ (PROBE 1) and (b) $\{x_1^P, x_2^P\} = \{0.075, 0.125\}\,[\mathrm{m}]$ (PROBE 2) both within the time window of observation $\{0 \leq ct \leq 3.0\}\,[\mathrm{m}]$. The discretization of circuit's rim is uniform with the the line segment of length $|\triangle\Omega^{[n]}| = 0.0125\,[\mathrm{m}]$, which corresponds to a eighth of the excitation pulse spatial support $ct_{\mathrm{w}} = 0.10\,[\mathrm{m}]$. The reference FIT model is composed of about 65 of thousands mesh cells and its lateral sides are defined as the perfect magnetic wall. The corresponding attenuated pulsed voltage responses are shown in Figs. 6.4a and 6.4b. Obviously, the obtained TD-CIM- and FIT-based signals are almost identical.

6.2.2 Inclusion of Debije's dielectric relaxation

The numerical example that follows is related to Sec. 6.1.2. The following numerical experiment validates the proposed inclusion of the Debije dielectric relaxation model in TD-CIM. In this example, the EM properties of the slab are defined via its relative electric permittivities $\epsilon_{\mathrm{r}} = 4.410$, $\epsilon_\infty = 4.195$ and

relaxation time $\tau_\mathrm{r} = 1.630 \cdot 10^{-11}$ [s]. The material parameters correspond to 'FR-4 (lossy)' as defined in the CST Material Library. Except for the material filling, the numerical models used for the TD-CIM and FIT simulations remain the same as in the previous section. The voltage pulses evaluated at $\{x_1^P, x_2^P\} = \{0.100, 0.075\}$ [m] (PROBE 1) are shown in Fig. 6.4c. Obviously, the signals resulting from TD-CIM and FIT almost overlap each other. It is worth to note that the early parts of the corresponding pulsed responses for conduction losses (viz Fig. 6.4a) and Debije's relaxation behavior (viz Fig. 6.4c) are almost identical. This observation is in agreement with the fact that any dispersion phenomenon shows itself in a transition region after the relevant wavefront has passed [31].

6.3 Conclusions

In order to incorporate the relaxation behavior of a planar circuit into TD-CIM its extension has been proposed. Namely, the inclusion of relaxation effects has been accomplished by a dedicated Laplace-transform inversion. The latter makes use of the Bromwich-contour deformation in the complex-frequency plane and allows for the inclusion of rather general relaxation mechanisms. The corresponding numerical examples concerning the conduction-loss and Debije-type relaxation functions have shown a very good agreement with respect to (three-dimensional) FIT.

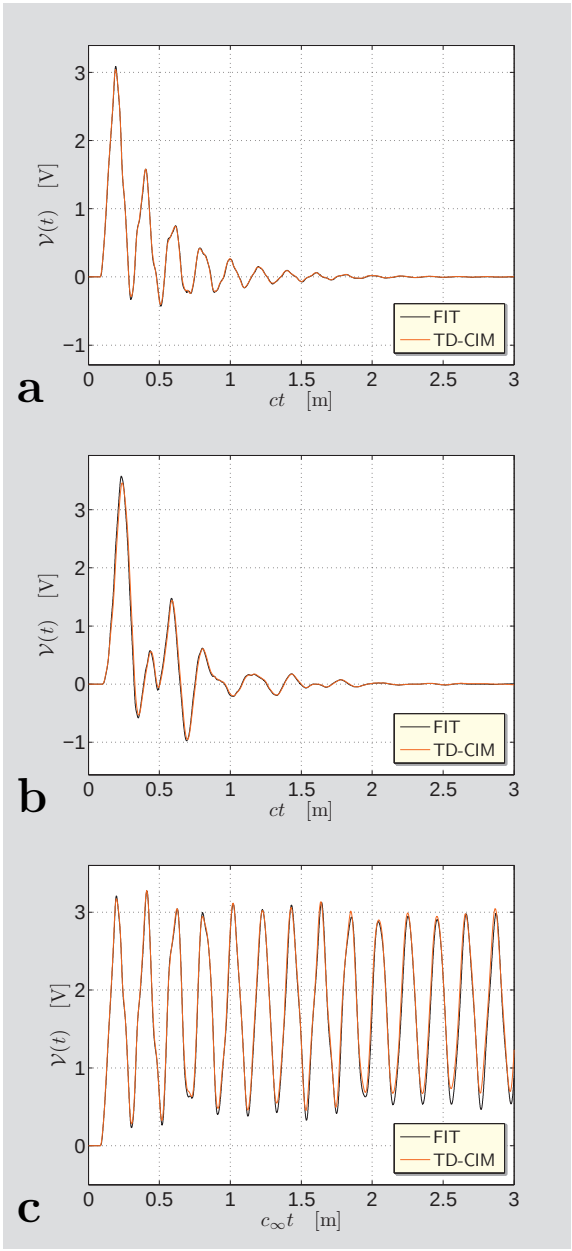

Figure 6.4: The pulsed voltage responses as evaluated using the proposed TD-CIM and the referential FIT of the rectangular circuit with (a) conduction loss evaluated at PROBE 1; (b) conduction loss evaluated at PROBE 2; (c) Debije's relaxation evaluated at PROBE 1.

Chapter 7

Far-field radiation characteristics

Modeling of pulsed EM radiation is of interest for the TD performance analysis of microstrip antennas as well as for the evaluation of unintentional EMI due to switching noise induced on PCBs. In case of planar structures one may take the advantage of their (relatively) low thickness and make use of a simplified radiation model. In that model, the electric-current surface density on conducting plates is neglected against the magnetic-current surface density along the lateral sides of a planar circuit. In this way, the radiated EM field is represented via (the slant-stack transformation of) the equivalent magnetic-current surface density distributed along the circuit's rim. This approximation works well for thin planar circuits and was formerly applied to FD radiation-field analysis of patch antennas (e.g. [51, 115]). The present chapter develops the corresponding TD formulation.

The following sections are organized as follows. At first, in Sec. 7.1, the electric-field and magnetic-field radiation characteristics are represented via a line integral of the tangential magnetic-current surface density on the circuit periphery. Secondly, in the following Sec. 7.2, upon accounting for the piecewise linear expansion of the equivalent magnetic-current surface density, the radiation integral is approximated by a sum of the nodal electric-field coefficients resulting from TD-CIM. In Sec. 7.3, calculated pulse shapes of the relevant pulsed EM radiation characteristics are compared with ones found using FIT. Finally, time-varying three-dimensional radiation patterns of an irregularly-shaped planar antenna are presented.

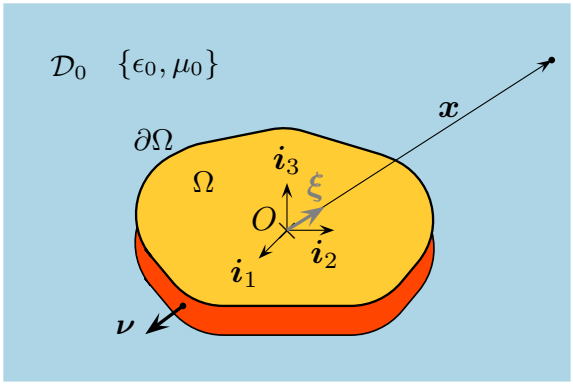

Figure 7.1: Radiation from a planar circuit. From [106], adapted with permission from IEEE, © 2014 IEEE.

7.1 Radiation model of a planar circuit

Let us consider an arbitrarily shaped planar circuit that is placed in the homogeneous and isotropic embedding $\mathcal{D}_0$ described by its electric permittivity ϵ_0 and magnetic permeability μ_0 (see Fig. 7.1). The corresponding EM wave speed is $c_0 = (\epsilon_0\mu_0)^{-1/2}$.

For planar circuits whose thickness d is negligible with respect to the spatial support of an excitation pulse, the total radiated EM field is dominantly generated by a magnetic-current surface density on the lateral sides of the circuit [4, Sec. 14.2.2]. For field points placed far from a circuit, the EM field components admit the far-field expansion

$$\{\boldsymbol{E}, \boldsymbol{H}\}(\boldsymbol{x}, t) = \frac{\{\boldsymbol{E}_\infty, \boldsymbol{H}_\infty\}(\boldsymbol{\xi}, t - |\boldsymbol{x}|/c_0)}{4\pi|\boldsymbol{x}|}\left[1 + \mathcal{O}\left(|\boldsymbol{x}|^{-1}\right)\right] \tag{7.1}$$

as $|\boldsymbol{x}| \to \infty$ for $\{t \in \mathbb{R}; t > 0\}$, where $\{\boldsymbol{E}_\infty, \boldsymbol{H}_\infty\}$ are the electric-field and magnetic-field vector radiation characteristics, respectively, and $\boldsymbol{\xi} = \boldsymbol{x}/|\boldsymbol{x}|$ is the unit vector in the direction of observation. Note that, in contrast to the previous sections, all bold Greek and Latin symbols stand for three-dimensional vectors. Interpreting the lateral sides of a circuit as Huygens' surfaces, the electric-field radiation characteristic is represented as [106, Eq. (9)]

$$\mathbf{I}_t\, \boldsymbol{E}_\infty(\boldsymbol{\xi}, t) = \frac{d}{c_0}\,\boldsymbol{\xi} \times \int_{\boldsymbol{x}' \in \partial\Omega} E_3(\boldsymbol{x}', t + \boldsymbol{\xi} \cdot \boldsymbol{x}'/c_0)\boldsymbol{\tau}(\boldsymbol{x}')\mathrm{d}l(\boldsymbol{x}') \tag{7.2}$$

where the integrand is assumed to be constant along the x_3-direction and $\boldsymbol{\tau} = \boldsymbol{i}_3 \times \boldsymbol{\nu}$ is the unit vector tangential with respect to the circuit periphery

$\partial\Omega$. It can be easily verified that the radiation characteristics are interrelated via the plane-wave relation

$$\boldsymbol{\xi} \times \boldsymbol{E}_\infty(\boldsymbol{\xi}, t) = (\mu_0/\epsilon_0)^{1/2} \boldsymbol{H}_\infty(\boldsymbol{\xi}, t) \tag{7.3}$$

Once the space-time distribution of the vertical electric field strength is known, the TD radiation characteristics of a planar circuit can be evaluated according to (7.2) and (7.3) for a given direction specified via the observation angle $\boldsymbol{\xi}$.

7.2 Evaluation of the radiation integral

Except for special cases the radiation integral given in Eq. (7.2) has to be evaluated numerically. As far as TD-CIM is concerned, the vertical electric-field strength is provided in terms of coefficients along the discretized circuit rim and the time axis. Specifically, the electric-field strength is represented as a piecewise linear function of space (cf. Eqs. (3.4)–(3.5))

$$E_3(\boldsymbol{x}, t) = \sum_{m=1}^{N} e^{[m]}(t) T^{[m]}(\boldsymbol{x}) \tag{7.4}$$

Since the integration of a piecewise linear function along a line segment can be carried out analytically, the spatial integral in (7.2) can be approximately written as the sum of the nodal field coefficients, i.e.

$$\begin{aligned} \mathbf{I}_t \, \boldsymbol{E}_\infty(\boldsymbol{\xi}, t) \simeq \frac{d}{2c_0} \sum_{m=1}^{N} \triangle\Omega^{[m]} \left(\boldsymbol{\xi} \times \boldsymbol{\tau}^{[m]}\right) \big[& e^{[m]}(t + \boldsymbol{\xi} \cdot \boldsymbol{x}_c^{[m]}/c_0) \\ & + e^{[m+1]}(t + \boldsymbol{\xi} \cdot \boldsymbol{x}_c^{[m]}/c_0) \big] \end{aligned} \tag{7.5}$$

where $e^{[m]}(t)$ and $e^{[m+1]}(t)$ are the time-dependent nodal values at the end-points of the m-th segment, $\boldsymbol{\tau}^{[m]} = (\boldsymbol{x}^{[m+1]} - \boldsymbol{x}^{[m]})/|\boldsymbol{x}^{[m+1]} - \boldsymbol{x}^{[m]}|$ is a unit vector tangential to the m-th segment and finally, $\boldsymbol{x}_c^{[m]} = (\boldsymbol{x}^{[m+1]} + \boldsymbol{x}^{[m]})/2$ localizes its central point. Since the computation runs along a discrete time axis only, the nodal values in (7.5) are appropriately interpolated between the neighboring instants.

7.3 Numerical results

In this section, the radiation characteristics are calculated for a planar circuit of irregular shape. We assume the loss-free dielectric slab of thickness

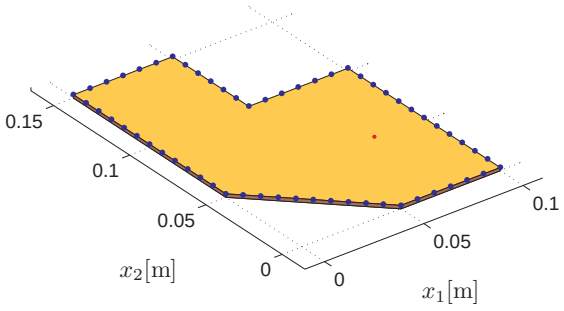

Figure 7.2: Computational model of the analyzed circuit with an electric-current vertical port (the dot on the patch).

$d = 1.50\,[\mathrm{mm}]$ showing the electric permittivity $\epsilon = 4.0\epsilon_0$ and magnetic permeability $\mu = \mu_0$. The TD-CIM model of the circuit with its discretized rim is shown in Fig. 7.2. The circuit is activated by the bell-shaped pulse with the amplitude $A = 1.0\,[\mathrm{A}]$ and the pulse time width $ct_\mathrm{w} = 0.10\,[\mathrm{m}]$ (see Fig. 3.3). The pulse is applied to a vertical excitation probe placed at $\{x_1^S, x_2^S\} = \{0.075, 0.05\}\,[\mathrm{m}]$. The electric-field radiation characteristics are observed within the time window of observation $\{0 \leq c_0 t < 3.0\}\,[\mathrm{m}]$. For validation purposes, we make use of FIT as implemented in the CST Microwave Studio®.

For the TD-CIM model, we assume the vertical excitation port with a hexagonal cross-section of circumradius $0.10\,[\mathrm{mm}]$ and the magnetic wall along the circuit periphery. The total number of the discretization line elements is 58 and the length of all discretization segments is less than a tenth of the spatial width of the excitation pulse. More precisely, we have $\max_m \left(|\triangle\Omega^{[m]}|\right)/ct_\mathrm{w} \simeq 0.083$. On the other hand, the reference FIT model consists of a circular excitation port with radius $0.1\,[\mathrm{mm}]$ and the 'open' boundary condition on the surrounding box. The total number of mesh cells is about 70 of thousands.

The electric-field radiation characteristics are evaluated with the help of Eq. (7.5) with the far-field origin (the phase center) placed at $(0.050, 0.075, 0)$ [m]. At first, for a given observation angle $\boldsymbol{\xi}$, the contributions from the line segments on the right-hand side of Eq. (7.5) are added up and secondly, the time difference is taken to get values of $\boldsymbol{E}_\infty(\boldsymbol{\xi}, t)$. For the sake of convenience, the TD radiation characteristics are expressed in terms of components with respect to the spherical coordinate system $\{0 \leq R < \infty, 0 \leq \phi \leq 2\pi, 0 \leq$

$\theta \leq \pi\}$

$$E_{\infty;\theta} = E_{\infty;1}\cos(\phi)\cos(\theta) + E_{\infty;2}\sin(\phi)\cos(\theta) - E_{\infty;3}\sin(\theta) \tag{7.6}$$

$$E_{\infty;\phi} = -E_{\infty;1}\sin(\phi) + E_{\infty;2}\cos(\phi) \tag{7.7}$$

where $E_{\infty;k}$ for $k = \{1, 2, 3\}$ denotes a Cartesian component of the three-dimensional radiation vector. Then the direction of observation can be uniquely determined by the spherical angles, i.e. $\boldsymbol{\xi} = \boldsymbol{\xi}(\phi, \theta)$.

The pulse shapes of the θ- and ϕ-components of the radiation vector are shown in Figs. 7.3 and 7.4 for two observation angles $\{\phi, \theta\} = \{\pi/4, \pi/4\}$ and $\{\phi, \theta\} = \{0, \pi/3\}$, respectively. As can be observed, the results calculated using TD-CIM and FIT agree well at the early part of the response and start to deviate at later observation times. This can be expected due to different nature of the boundary conditions imposed along the circuit periphery. While the TD-CIM model assumes the perfect magnetic wall here, the circuit boundary in the (three-dimensional) FIT model is fully 'open'. Note that the same behavior was observed in Sec. 3.4, where the vertical component of the electric-field strength along $\partial\Omega$ is evaluated. The latter, in fact, corresponds to the equivalent magnetic-current surface density that generates the observed far-field amplitude.

In the next step, three-dimensional, time-varying radiation patterns were calculated. Their surface was constructed, for a fixed point in time, by mapping the absolute values of the far field to a set of observation points on the unit sphere. Consequently, the actual values of the radiated field were represented with a color scale. The results are shown in Figs. 7.5–7.7 for the θ-, ϕ-components and absolute values of the electric-field radiation characteristic, respectively. In order to demonstrate its time evolution, we take $c_0 t = \{0.60, 1.20, 1.80, 2.40\}$ [m] as the observation time points.

7.4 Conclusions

The pulsed EM radiation from a planar circuit has been analyzed in the context of TD-CIM. It has been shown that the electric-field (time-integrated) far-field amplitude can be expressed using the slant-stack transformation of the equivalent magnetic-current surface density distributed along circuit's rim. A straightforward numerical solution of the integral representation has been proposed and numerically validated for the case of an irregularly-shaped planar circuit. The resulting radiated pulse shapes have shown a very good agreement with respect to the ones evaluated with the aid of (three-dimensional) FIT.

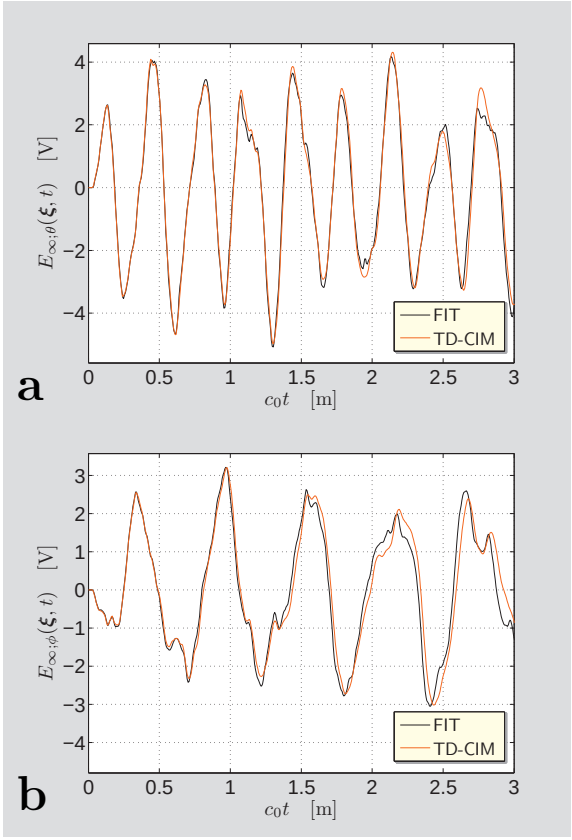

Figure 7.3: The radiated pulse shapes evaluated using the proposed TD-CIM and the referential FIT at $\{\phi, \theta\} = \{\pi/4, \pi/4\}$ for the (a) θ-component; (b) ϕ-component of the vectorial electric-field radiation characteristic.

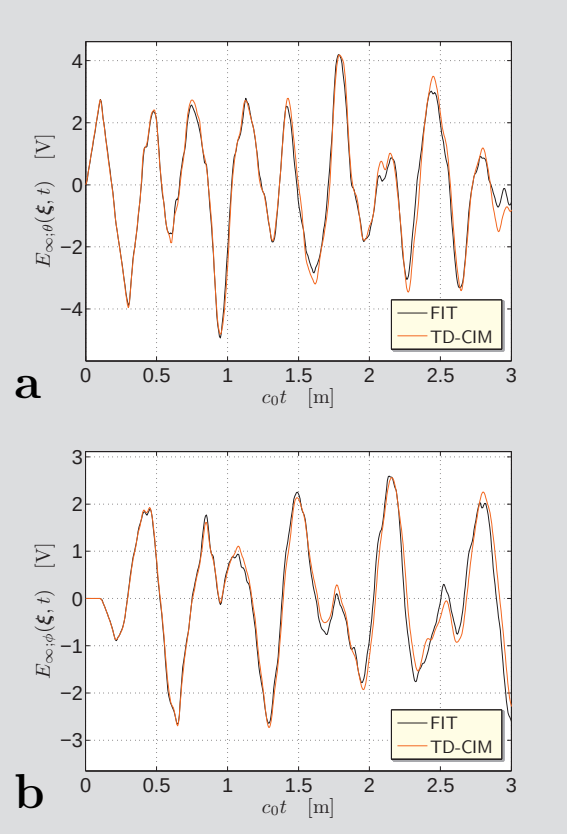

Figure 7.4: The radiated pulse shapes evaluated using the proposed TD-CIM and the referential FIT at $\{\phi, \theta\} = \{0, \pi/3\}$ for the (a) θ-component; (b) ϕ-component of the vectorial electric-field radiation characteristic.

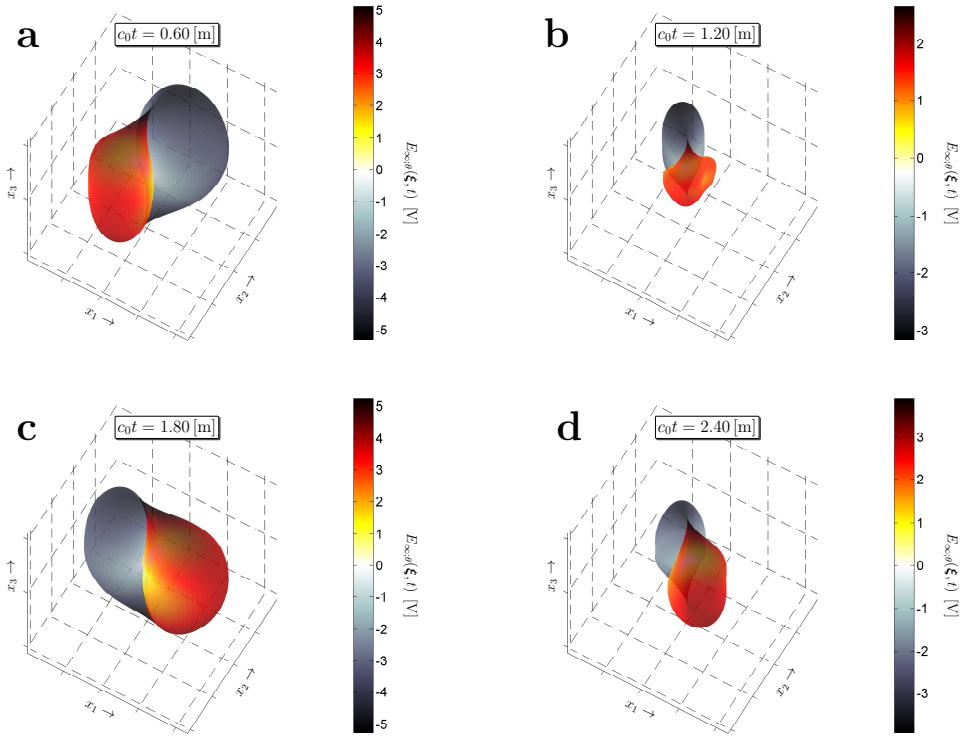

Figure 7.5: Time-varying radiation diagram of the θ-component of the vectorial electric-field radiation characteristic.

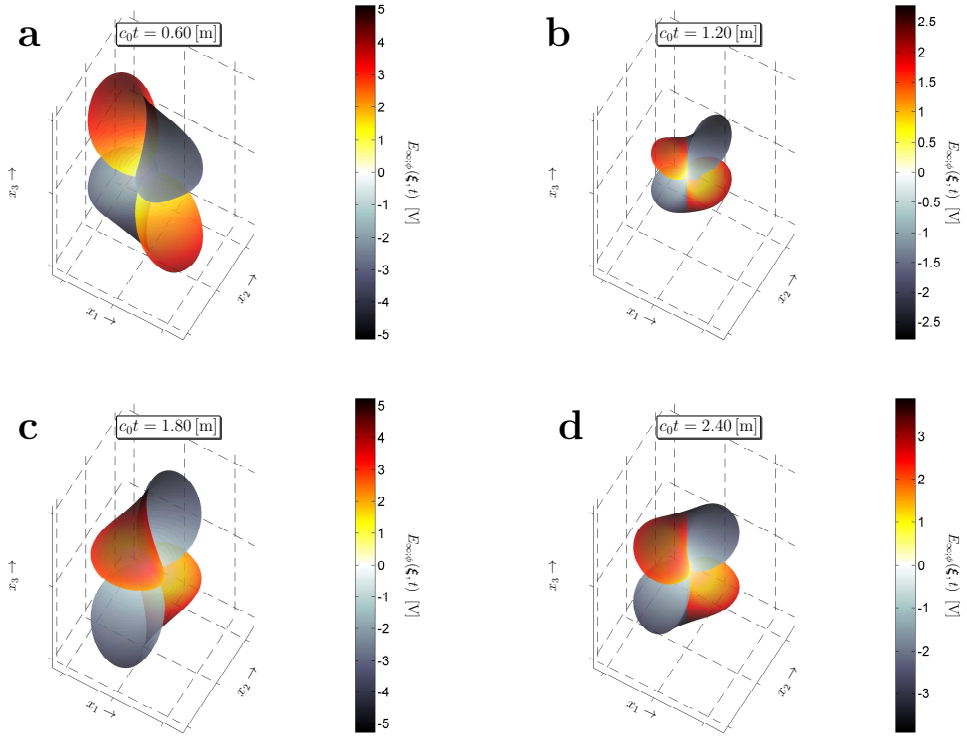

Figure 7.6: Time-varying radiation diagram of the ϕ-component of the vectorial electric-field radiation characteristic.

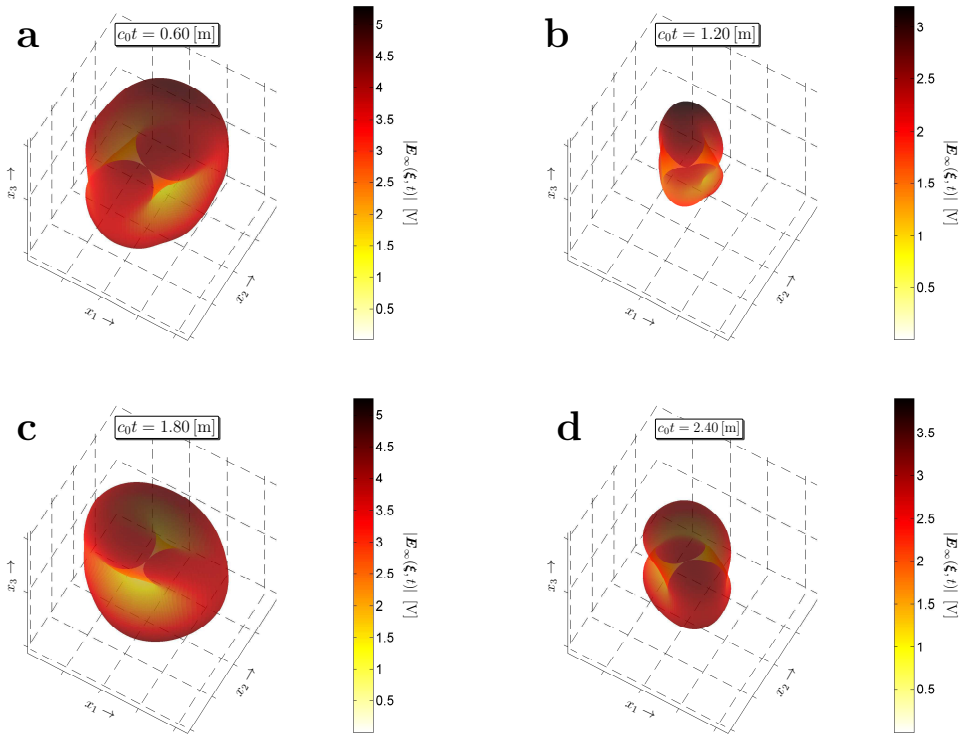

Figure 7.7: Time-varying radiation diagram of the absolute value of the vectorial electric-field radiation characteristic.

Chapter 8

Time-domain mutual coupling between planar circuits

The recent trend in still increasing bit and edge rates of bit-like signals on high-speed digital systems puts severe demands on their performance as well as on the corresponding computational tools [2, 81]. The generation of switching noise together with still increasing crowding of components on PCBs urgently call for a thorough study into *time-domain* coupling phenomena. Proper understanding of TD mutual coupling between planar structures, that represent the basic building blocks of advanced digital systems [118], is therefore of major importance in the efficient prevention of accompanying signal integrity issues.

Mutual coupling effects between microstrip elements have been intensively studied in the real-FD (see e.g. [40, 52, 64, 73, 74], for example). Here, basically, two main approaches can be distinguished. The first approach is based on the concept of reaction [83] combined with the cavity model [51] and its description in terms of the eigenfunction field expansion [52, 73]. The second one is more general and relies on a full wave solution via the method of moments [64, 74].

Despite the fact that high-speed digital circuits inherently operate in TD, the corresponding TD analysis, that would shed light on the mutual interaction of parallel-plate radiators, is lacking in literature on the subject. The main purpose of this chapter[1], therefore, is to fill this gap and provide the interference analysis of planar circuits entirely in space-time. To this end, the reciprocity theorem of the time-convolution type [20, Sec. 28.2] is taken as the point of departure. It is shown that its combination with TD-CIM yields

[1]This chapter is largely based on Reference [109]. Adapted with permission from IEEE, © 2014 IEEE.

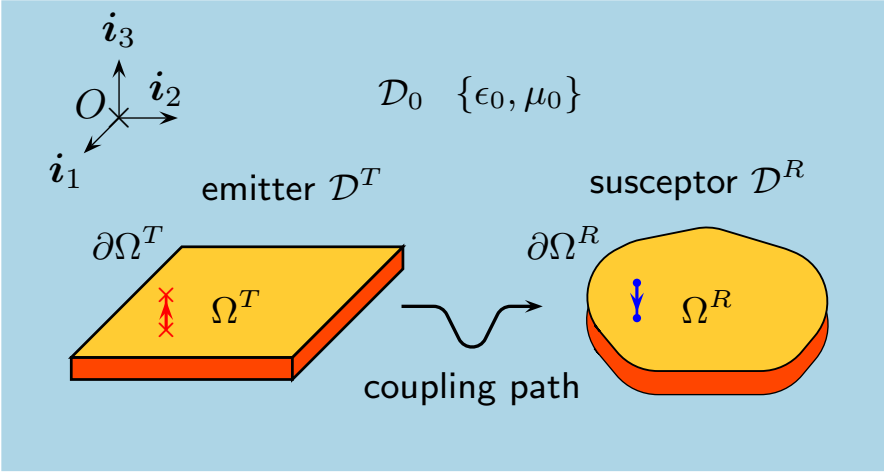

Figure 8.1: Problem configuration consisting of two arbitrarily-shaped planar circuits that are electromagnetically coupled. From [109], adapted with permission from IEEE, © 2014 IEEE.

a promising computational tool that serves the purpose very well. Finally it is worth to note that the TD EM coupling is largely a desired phenomenon for intra- and inter-chip wireless interconnections [11, 44]. Mastery of the pulsed-field transfer between two EM radiators is the key point towards the full utilization of wireless interconnects in practice. Here, too, compliance with the international regulations on EMI is of crucial importance [45].

The following sections are organized as follows. For the sake of completeness, the starting reciprocity-based contour-integral formulation for the TD-CIM analysis of a single planar circuit is given in Sec. 8.2. Subsequently, the main results of this chapter are presented in Sec. 8.3 using the systematic application of the reciprocity theorem of the time-convolution type. Here it is shown that the pulsed-voltage response of a receiving (or victim) planar circuit can be expressed via straightforward rim-to-rim relations consisting of two contour integrations over transmitting- and receiving-circuits' rims. Finally, the resulting coupling model is implemented and validated in Sec. 8.4, where EM coupling of two irregularly-shaped planar circuits is numerically analyzed.

8.1 Coupling model

The problem configuration consists of a transmitting planar circuit (the emitter) $\mathcal{D}^T \subset \mathbb{R}^3$ and a receiving planar circuit (the susceptor) $\mathcal{D}^R \subset \mathbb{R}^3$ that

are placed in the linear, isotropic, homogeneous and loss-free embedding $\mathcal{D}_0$ whose EM properties are described by its electric permittivity ϵ_0 and magnetic permeability μ_0 (see Fig. 8.1). The corresponding EM wave speed is $c_0 = (\epsilon_0\mu_0)^{-1/2} > 0$. Each planar circuit is described by its surface domain $\Omega^{T,R} \subset \mathbb{R}^2$, its thickness $d^{T,R}$ and by its relative electric permittivity $\epsilon_{\mathrm{r}}^{T,R}$ of the dielectric filling. The EM wave speed in the dielectric layer is then $c^{T,R} = c_0(\epsilon_{\mathrm{r}}^{T,R})^{-1/2}$. The outer unit vector with respect to the circuit rims $\partial\Omega^{T,R} \subset \mathbb{R}$ is denoted by $\boldsymbol{\nu}^{T,R} = \boldsymbol{\nu}^{T,R}(\boldsymbol{x})$ and $\boldsymbol{\tau}^{T,R} = \boldsymbol{\tau}^{T,R}(\boldsymbol{x}) = \boldsymbol{i}_3 \times \boldsymbol{\nu}^{T,R}$.

The main goal of the following interference analysis is to find the pulsed voltage induced in the receiving circuit $\mathcal{D}^R$ due to the pulsed electric-current excitation applied to the transmitting circuit $\mathcal{D}^T$.

8.2 A single planar circuit

In this section, a global reciprocity relation is formulated for a single planar circuit. Throughout this section, we do not distinguish between the transmitting and the receiving circuit. As a consequence, Ω and $\partial\Omega$ stand for $\Omega^{T,R}$ and $\partial\Omega^{T,R}$, respectively. The reciprocity theorem of the time-convolution type is applied to the actual and testing (B) wave fields and to the surface domain of a planar circuit Ω. Considering the testing source density along the circuit periphery only, we finally end up with (cf. Eq. (2.34))

$$\begin{aligned}\tfrac{1}{2}\int_{\boldsymbol{x}\in\partial\Omega} E_3(\boldsymbol{x},t) * \partial J_3^B(\boldsymbol{x}|\boldsymbol{x}^S,t)\mathrm{d}l(\boldsymbol{x}) = \int_{\boldsymbol{x}\in\Omega} E_3^B(\boldsymbol{x}|\boldsymbol{x}^S,t) * J_3(\boldsymbol{x},t)\mathrm{d}A(\boldsymbol{x}) \\ + \int_{\boldsymbol{x}\in\partial\Omega} E_3(\boldsymbol{x},t) * \boldsymbol{\nu}(\boldsymbol{x}) \cdot \partial\boldsymbol{J}^B(\boldsymbol{x}|\boldsymbol{x}^S,t)\mathrm{d}l(\boldsymbol{x}) \qquad (8.1)\end{aligned}$$

where the testing fields are linearly related to their source according to

$$E_3^B(\boldsymbol{x}|\boldsymbol{x}^S,t) = -\mu\partial_t \int_{\boldsymbol{x}^T\in\partial\Omega} G_\infty[r(\boldsymbol{x}|\boldsymbol{x}^T),t] * \partial J_3^B(\boldsymbol{x}^T|\boldsymbol{x}^S,t)\mathrm{d}l(\boldsymbol{x}^T) \qquad (8.2)$$

$$\partial J_\kappa^B(\boldsymbol{x}|\boldsymbol{x}^S,t) = -\partial_\kappa \int_{\boldsymbol{x}^T\in\partial\Omega} G_\infty[r(\boldsymbol{x}|\boldsymbol{x}^T),t] * \partial J_3^B(\boldsymbol{x}^T|\boldsymbol{x}^S,t)\mathrm{d}l(\boldsymbol{x}^T) \qquad (8.3)$$

for all $\boldsymbol{x}^S \in \partial\Omega$ and $t > 0$. Here, $r(\boldsymbol{x}|\boldsymbol{x}^T) = |\boldsymbol{x} - \boldsymbol{x}^T|$ is the Eucledian distance between positions given by the position vectors $\boldsymbol{x}$ and $\boldsymbol{x}^T$ and $G_\infty(r,t)$ denotes a fundamental solution of the two-dimensional wave equation that satisfies the zero initial conditions and the causality condition. In the interference analysis that follows, Eq. (8.1) is solved numerically for the both transmitting and receiving planar circuits using TD-CIM. The corresponding solution procedure for a loss-free planar circuit is closely described in Chapter 3.

8.3 Coupling between two planar circuits

In this section, the study into the TD mutual coupling between the planar circuits is carried out. To this end, the total field in the receiving state (R) is written as the superposition of incident (i) and scattered (s) wave fields, i.e.

$$\{\boldsymbol{E}^R, \boldsymbol{H}^R\} = \{\boldsymbol{E}^i + \boldsymbol{E}^s, \boldsymbol{H}^i + \boldsymbol{H}^s\} \tag{8.4}$$

As the testing state (B) we take the testing wave field $\{\boldsymbol{E}^B, \boldsymbol{H}^B\}$ generated by a vertical excitation port

$$\boldsymbol{J}^B(\boldsymbol{x}, t) = \mathcal{I}^B(t)\delta(\boldsymbol{x} - \boldsymbol{x}^S)\boldsymbol{i}_3 \tag{8.5}$$

for $\boldsymbol{x}^S \in \mathcal{D}^R$, where $\mathcal{I}^B$ is the source signature for which $\mathcal{I}^B(t) = 0$ for $t < 0$. The testing wave field satisfies the magnetic-wall boundary condition $\boldsymbol{\nu}^R \cdot \boldsymbol{H}^B(\boldsymbol{x}, t) = 0$ for all $\boldsymbol{x} \in \partial\Omega^R$ and $t > 0$ (cf. Eq. (2.6)). At this point it is noted that in the analysis we neglect multiple scattering between the planar circuits meaning that the testing wave field does not account for the presence of the transmitting circuit. This assumption, however, does not introduce any error up to the instant when a scattered field due to the presence of the transmitter gets back to the receiver. Consequently, the early part of the pulsed voltage response is exact, whatever coupling strength. Beyond this limit, especially in applications where multiple scattering effects are of crucial importance, one has to resort to a full-wave numerical solver.

In the first step, the reciprocity theorem is applied to the domain exterior to the receiving structure and to the scattered and testing wave fields, which gives

$$\int_{\boldsymbol{x}\in\partial\mathcal{D}^R} \Big[\boldsymbol{E}^B(\boldsymbol{x}, t) \overset{*}{\times} \boldsymbol{H}^s(\boldsymbol{x}, t) - \boldsymbol{E}^s(\boldsymbol{x}, t) \overset{*}{\times} \boldsymbol{H}^B(\boldsymbol{x}, t)\Big] \cdot \boldsymbol{\nu}^R(\boldsymbol{x})\mathrm{d}A(\boldsymbol{x}) = 0 \tag{8.6}$$

for all $t > 0$. Substitution of Eq. (8.4) in (8.6) yields

$$\begin{aligned}\int_{\boldsymbol{x}\in\partial\mathcal{D}^R} &\Big[\boldsymbol{E}^B(\boldsymbol{x}, t) \overset{*}{\times} \boldsymbol{H}^R(\boldsymbol{x}, t) - \boldsymbol{E}^R(\boldsymbol{x}, t) \overset{*}{\times} \boldsymbol{H}^B(\boldsymbol{x}, t)\Big] \cdot \boldsymbol{\nu}^R(\boldsymbol{x})\mathrm{d}A(\boldsymbol{x}) \\ = \int_{\boldsymbol{x}\in\partial\mathcal{D}^R} &\Big[\boldsymbol{E}^B(\boldsymbol{x}, t) \overset{*}{\times} \boldsymbol{H}^i(\boldsymbol{x}, t) - \boldsymbol{E}^i(\boldsymbol{x}, t) \overset{*}{\times} \boldsymbol{H}^B(\boldsymbol{x}, t)\Big] \cdot \boldsymbol{\nu}^R(\boldsymbol{x})\mathrm{d}A(\boldsymbol{x})\end{aligned} \tag{8.7}$$

for all $t > 0$ Secondly, the reciprocity theorem is applied to the domain occupied by the receiving circuit $\mathcal{D}^R$ and to the total wave fields in the both states

$$\int_{\boldsymbol{x}\in\partial\mathcal{D}^R} \Big[\boldsymbol{E}^B(\boldsymbol{x},t) \overset{*}{\times} \boldsymbol{H}^R(\boldsymbol{x},t) - \boldsymbol{E}^R(\boldsymbol{x},t) \overset{*}{\times} \boldsymbol{H}^B(\boldsymbol{x},t)\Big] \cdot \boldsymbol{\nu}^R(\boldsymbol{x})\mathrm{d}A(\boldsymbol{x}) = \int_{\boldsymbol{x}\in\mathcal{D}^R} \boldsymbol{J}^B(\boldsymbol{x},t) \overset{*}{\cdot} \boldsymbol{E}^R(\boldsymbol{x},t)\mathrm{d}V(\boldsymbol{x}) \quad (8.8)$$

In virtue of the thin-slab approximation and the magnetic-wall boundary condition satisfied by the testing wave field, we arrive, upon combining Eqs. (8.7)–(8.8), at the final expression

$$\mathcal{V}^R(\boldsymbol{x}^S,t) * \mathcal{I}^B(t) \simeq -\int_{\boldsymbol{x}\in\partial\Omega^R} \mathcal{V}^B(\boldsymbol{x}|\boldsymbol{x}^S,t) * \boldsymbol{\tau}^R(\boldsymbol{x}) \cdot \boldsymbol{H}^i(\boldsymbol{x},t)\mathrm{d}l(\boldsymbol{x}) \quad (8.9)$$

for all $\boldsymbol{x}^S \in \Omega^R$ and $t > 0$. In Eq. (8.9), $\mathcal{V}^R$ is the TD voltage induced in the receiving circuit due to the tangential magnetic field strength radiated from the transmitting circuit and $\mathcal{V}^B(\boldsymbol{x}|\boldsymbol{x}^S,t)$ represents the TD testing voltage along the rim of the receiving circuit $\boldsymbol{x} \in \partial\Omega^R$ activated via the electric-current point source placed at $\boldsymbol{x}^S \in \Omega^R$ (see Eq. (8.5)). The incident magnetic field strength is given via the following Kirchhoff-Huygens electromagnetic field representations

$$\boldsymbol{H}^i = \boldsymbol{H}^{i;\mathrm{NF}} + \boldsymbol{H}^{i;\mathrm{IF}} + \boldsymbol{H}^{i;\mathrm{FF}} \quad (8.10)$$

where

$$\boldsymbol{H}^{i;\mathrm{NF}}(\boldsymbol{x}^R,t) \simeq -\mu_0^{-1} \int_{\boldsymbol{x}\in\partial\Omega^{\mathrm{T}}} \frac{\mathbf{I}_t\mathcal{V}^T(\boldsymbol{x},t-|\boldsymbol{x}^R-\boldsymbol{x}|/c_0)}{4\pi|\boldsymbol{x}^R-\boldsymbol{x}|^3} \big[3\boldsymbol{\xi}(\boldsymbol{x}^R-\boldsymbol{x})\boldsymbol{\xi}^{\mathrm{T}}(\boldsymbol{x}^R-\boldsymbol{x}) - \mathbb{I}\big] \cdot \boldsymbol{\tau}^T(\boldsymbol{x})\mathrm{d}l(\boldsymbol{x}) \quad (8.11)$$

$$\boldsymbol{H}^{i;\mathrm{IF}}(\boldsymbol{x}^R,t) \simeq -\eta_0 \int_{\boldsymbol{x}\in\partial\Omega^{\mathrm{T}}} \frac{\mathcal{V}^T(\boldsymbol{x},t-|\boldsymbol{x}^R-\boldsymbol{x}|/c_0)}{4\pi|\boldsymbol{x}^R-\boldsymbol{x}|^2} \big[3\boldsymbol{\xi}(\boldsymbol{x}^R-\boldsymbol{x})\boldsymbol{\xi}^{\mathrm{T}}(\boldsymbol{x}^R-\boldsymbol{x}) - \mathbb{I}\big] \cdot \boldsymbol{\tau}^T(\boldsymbol{x})\mathrm{d}l(\boldsymbol{x}) \quad (8.12)$$

$$\boldsymbol{H}^{i;\mathrm{FF}}(\boldsymbol{x}^R,t) \simeq -\epsilon_0 \int_{\boldsymbol{x}\in\partial\Omega^{\mathrm{T}}} \frac{\partial_t\mathcal{V}^T(\boldsymbol{x},t-|\boldsymbol{x}^R-\boldsymbol{x}|/c_0)}{4\pi|\boldsymbol{x}^R-\boldsymbol{x}|} \big[\boldsymbol{\xi}(\boldsymbol{x}^R-\boldsymbol{x})\boldsymbol{\xi}^{\mathrm{T}}(\boldsymbol{x}^R-\boldsymbol{x}) - \mathbb{I}\big] \cdot \boldsymbol{\tau}^T(\boldsymbol{x})\mathrm{d}l(\boldsymbol{x}) \quad (8.13)$$

for all $\boldsymbol{x}^R \in \partial\Omega^R$ and $t > 0$, where $\mathcal{V}^T$ is the voltage on a rim of the transmitting structure, $\boldsymbol{\xi}(\boldsymbol{x}) = \boldsymbol{x}/|\boldsymbol{x}|$ is the unit vector in the direction of $\boldsymbol{x}$, $\mathbb{I}$ is the

3×3 identity matrix, $^{\mathrm{T}}$ denotes transposition and $\eta_0 = (\epsilon_0/\mu_0)^{1/2} > 0$. It is worth noting that combination of Eq. (8.9) with Eqs. (8.10)–(8.13) provides a useful space/time relation between the interacting planar structures.

In conclusion, the described approach consists of the following steps. Starting with the transmitting structure, the pulsed voltage distribution $\mathcal{V}^T$ is evaluated for all $\boldsymbol{x} \in \partial\Omega^T$ in a given time window and for a given excitation electric-current pulse $\mathcal{I}^T(t)$. This step can be done, for an arbitrarily-shaped planar structure, with the aid of TD-CIM as introduced in Chapter 3. The evaluated voltage distribution $\mathcal{V}^T$ is subsequently substituted in Eqs. (8.11)–(8.13), which yields the incident magnetic field strength at points along the rim of the receiving structure $\partial\Omega^R$. Since domains occupied by the interacting planar circuits are disjoint, Eqs. (8.11)–(8.13) are free of the spatial singularities, and their evaluation, therefore, do not present any difficulties. In the next step, the testing pulsed voltage $\mathcal{V}^B$ due to the electric-current pulse shape $\mathcal{I}^B$ is evaluated for all $\boldsymbol{x} \in \partial\Omega^R$ in a given time window. This step is accomplished through TD-CIM again. Finally, once the time convolution on the right-hand side of Eq. (8.9) is evaluated, $\mathcal{V}^R$ may be readily recovered for a convenient choice of the testing electric-current pulse shape $\mathcal{I}^B(t)$. The shortest way to obtain $\mathcal{V}^R$ from the known convolution $\mathcal{V}^R * \mathcal{I}^B$ would be to choose the Dirac delta test-source signature $\mathcal{I}^B(t) = \delta(t)$. This option, apparently, is not possible as the corresponding voltage response $\mathcal{V}^B$ is evaluated using TD-CIM that requires a somewhat smoother excitation signature (see Eq. (3.14)). In case of the bell-shaped electric-current signature (cf. Eq. (D.6))

$$\begin{aligned}\mathcal{I}^B(t) = {} & 2\left(\frac{t}{t_{\mathrm{w}}}\right)^2 \mathrm{H}(t) - 4\left(\frac{t}{t_{\mathrm{w}}} - \frac{1}{2}\right)^2 \mathrm{H}\left(\frac{t}{t_{\mathrm{w}}} - \frac{1}{2}\right) \\ & + 4\left(\frac{t}{t_{\mathrm{w}}} - \frac{3}{2}\right)^2 \mathrm{H}\left(\frac{t}{t_{\mathrm{w}}} - \frac{3}{2}\right) - 2\left(\frac{t}{t_{\mathrm{w}}} - 2\right)^2 \mathrm{H}\left(\frac{t}{t_{\mathrm{w}}} - 2\right)\end{aligned} \tag{8.14}$$

one may employ, for example, the following two-step deconvolution procedure. In this procedure, the bell-shaped pulse is written as the time convolution of the rectangular and triangular functions, which finally yields

$$\mathcal{V}^R(\boldsymbol{x}^S, t) = \partial_t^2 \mathcal{T}^T(\boldsymbol{x}^S, t) + 2\mathcal{V}^R(\boldsymbol{x}^S, t - t_{\mathrm{w}}/2) - \mathcal{V}^R(\boldsymbol{x}^S, t - t_{\mathrm{w}}) \tag{8.15}$$

where

$$\mathcal{T}^T(\boldsymbol{x}^S, t) = t_{\mathrm{w}}^2 \partial_t \mathcal{V}^R(\boldsymbol{x}^S, t) * \mathcal{I}^B(t)/4 + \mathcal{T}^T(\boldsymbol{x}^S, t - t_{\mathrm{w}}) \tag{8.16}$$

corresponds to the time convolution of the sought voltage response $\mathcal{V}^R$ with the triangular pulse $\mathrm{T}(t, t_{\mathrm{w}})$ (see Eq. (D.4)). For an alternative closed-form deconvolution algorithm we refer the reader to Eq. (10.22).

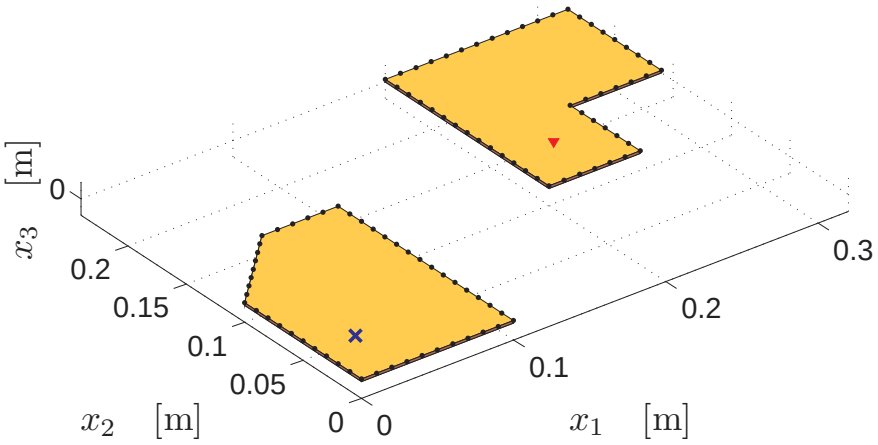

Figure 8.2: Computational model of the analyzed configuration in which the transmitting structure is activated by an electric-current vertical port (the cross symbol) and the induced voltage response is observed by a probe (the solid triangle).

8.4 An illustrative numerical example

This section provides an illustrative numerical example concerning the TD mutual coupling between two planar circuits both lying in one plane $x_3 = 0$. The analyzed problem configuration is shown in Fig. 8.2. In this configuration, the transmitting circuit is excited by a vertical electrical-current source centered at $\boldsymbol{x}^T = \{25.0, 37.5, 0\}, [\text{mm}]$ (see the red dot in Fig. 8.2). The pulse shape of the electric-current source is shown in Fig. 3.3. Here, $c = c^R = c^T$ since the both studied circuits show the relative electric permittivity $\epsilon_{\text{r}}^{T,R} = 4.0$. Their thickness is $d^{T,R} = 1.50\,[\text{mm}]$.

The pulsed voltage response is observed at $\boldsymbol{x}^R = \{230, 135, 0\}$ [mm] in the receiving planar circuit (see the blue dot in Fig. 8.2). In order to validate the developed computational model, the problem has also been analyzed using FIT as implemented in CST Microwave Studio®. The three-dimensional FIT-based model consists of about 620 of *thousands* hexahedral mesh cells, while the developed model requires to account for only $(48 + 52)$ of line segments along the peripheral rims (see the black dots in Fig. 8.2). The results are shown in Fig. 8.3. Considering the huge reduction of the solution space, the observed signals agree very well.

It is worth noting that calculation of the pulsed-voltage response via the rim-to-rim expressions (8.9)–(8.13) involves the one-dimensional integrations

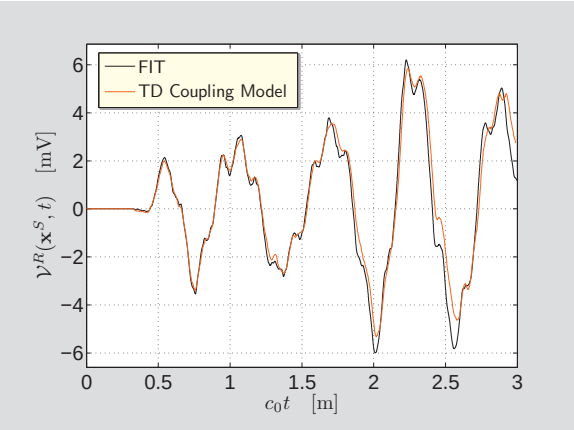

Figure 8.3: The pulsed voltage response at the probe as evaluated using the proposed coupling model and the referential FIT. From [109], adapted with permission from IEEE, © 2014 IEEE.

only, whatever the emitter/susceptor distance. This property along with the omission of multiple scattering effects make the constructed model suitable for applications where the emitter/susceptor distance related to the spatial support of an excitation pulse is relatively large and the traditional direct-discretization numerical approaches require an exceedingly high number of discretization cells within their (truncated) three-dimensional computational domain.

8.5 Conclusions

Space-time mutual EM coupling between two planar circuit has been described in closed form directly in TD. Besides providing physical insights into the mutual (space-time) coupling mechanism, the proposed coupling model indicates huge savings of computational resources with respect to the traditional direct-discretization numerical methods such as FIT. Accordingly, the use of the constructed model is especially profitable in configurations where the spatial support of an excitation pulse is relatively short with respect to the emitter/susceptor distance. Thanks to its high efficiency, the introduced methodology may find its applications in optimizing TD coupling effects between planar circuits, wireless interconnections or simple antenna arrays.

Chapter 9

Time-domain self-reciprocity of a one-port planar circuit

The concept of reciprocity is without doubt among the most intriguing concepts in EM theory. The reciprocity theorem furnishes a solid foundation for the uniqueness theorem [22], encompasses the 'weak' formulations of direct and inverse scattering/source problems [18], it has wealthy applications in computational electromagnetics [19] and facilitates the rigorous study into the fundamental transmission/reception properties of general antenna systems [24]. The vast majority of works on reciprocity are traditionally carried out in the real-FD [17, 23, 78, 94], [103, Sec. 8.7],[12, Sec. 5.1]. Despite the still growing interest in purely TD applications such as Ultra Wide Band (UWB) radio systems [56] or inter/intra-chip wireless interconnections [11, 45], the pulsed-field antenna and EMC/EMI aspects were much less discussed so far. Only a few exceptions in this respect do exist. The general antenna-system description in TD can be found in [5, 24, 89] and a small-antenna UWB radio link and its optimization is investigated in [76, 77]. The main purpose of this chapter[1], therefore, is to construct a purely TD self-reciprocity relation that makes possible to find the pulsed EM radiation characteristics of a planar circuit through its reaction on an incident plane wave in the receiving state.

The following sections are organized as follows. At first, Secs. 9.1–9.3 introduce the reader to the transmitting and receiving situations of a one-port planar circuit. Subsequently, the main results of the chapter are developed in Sec. 9.4, where the desired self-reciprocity relation is derived using the reciprocity theorem of the time-convolution type. Apart from its application to constructing the pulsed EM radiation characteristics, it is finally demon-

[1]This chapter is largely based on Reference [106]. Adapted with permission from IEEE, © 2014 IEEE.

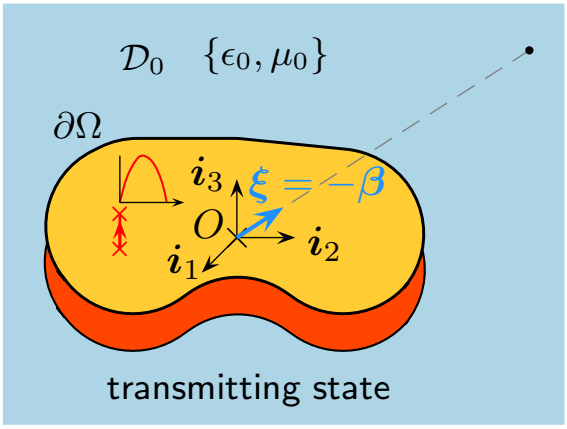

Figure 9.1: Planar circuit in its transmitting state. From [106], adapated with permission from IEEE, © 2014 IEEE.

strated in Sec. 9.5 that the introduced self-reciprocity relation is useful for consistency benchmarks of purely numerical EM-field solvers.

9.1 Model definition

Let us assume a one-port planar circuit that occupies a domain $\mathcal{D} \subset \mathbb{R}^3$ bounded by $\partial\mathcal{D} \subset \mathbb{R}^2$. The circuit is placed in the linear, isotropic, homogeneous and loss-free embedding $\mathcal{D}_0$ whose EM properties are described by its electric permittivity ϵ_0 and magnetic permeability μ_0. The corresponding EM wave speed is $c_0 = (\epsilon_0\mu_0)^{-1/2} > 0$. The EM properties of the dielectric slab are described by its electric permittivity ϵ and magnetic permeability μ_0. The electrically conducting plate of the circuit occupies a surface domain $\Omega \subset \partial\mathcal{D}$ bounded by its rim $\partial\Omega \subset \mathbb{R}$. The normal outer unit vector is denoted by $\boldsymbol{\nu}$. Partial differentiation with respect to the spatial coordinates is, for the sake of conciseness, denoted by $\boldsymbol{\nabla} = \partial_1\boldsymbol{i}_1 + \partial_2\boldsymbol{i}_2 + \partial_3\boldsymbol{i}_3$. In the following sections we find a reciprocity relation between transmitting and receiving properties of a one-port planar circuit.

9.2 Transmitting state of a planar circuit

The planar circuit is in its transmitting state activated via the vertical excitation probe (see Fig. 9.1) with defined electric-current density $\boldsymbol{J}^T = J^T\boldsymbol{i}_3$.

The transmitted (T) EM field then satisfies

$$\boldsymbol{\nabla} \times \boldsymbol{H}^T - \epsilon \partial_t \boldsymbol{E}^T = \boldsymbol{J}^T \tag{9.1}$$

$$\boldsymbol{\nabla} \times \boldsymbol{E}^T + \mu_0 \partial_t \boldsymbol{H}^T = \boldsymbol{0} \tag{9.2}$$

for all $\boldsymbol{x} \in \mathcal{D}$ and $t > 0$, where the thin-slab approximation is tacitly assumed (cf. Eqs. (2.1)–(2.2)). In the domain exterior to the circuit the transmitted EM field satisfies

$$\boldsymbol{\nabla} \times \boldsymbol{H}^T - \epsilon_0 \partial_t \boldsymbol{E}^T = \boldsymbol{0} \tag{9.3}$$

$$\boldsymbol{\nabla} \times \boldsymbol{E}^T + \mu_0 \partial_t \boldsymbol{H}^T = \boldsymbol{0} \tag{9.4}$$

for all $\boldsymbol{x} \in \mathcal{D}_0$ and $t > 0$ together with the 'radiation condition'. By virtue of causality, the radiated EM field admits the far-field representation (7.1) and hence its contribution from the 'sphere at infinity' vanishes. Finally, upon neglecting the contribution of the electric-current surface density on the circuit's conducting surfaces, we may find the corresponding radiation characteristics as (cf. (7.2))

$$\mathbf{I}_t \, \boldsymbol{E}^T_\infty(\boldsymbol{\xi}, t) = \frac{d}{c_0} \, \boldsymbol{\xi} \times \int_{\boldsymbol{x}' \in \partial\Omega} \boldsymbol{E}^T(\boldsymbol{x}', t + \boldsymbol{\xi} \cdot \boldsymbol{x}'/c_0) \times \boldsymbol{\nu}(\boldsymbol{x}') \mathrm{d}l(\boldsymbol{x}') \tag{9.5}$$

Equation (9.5) expresses the pulsed EM radiation characteristics in terms of the (equivalent) magnetic-current surface density on the circuit's periphery.

9.3 Receiving state of a planar circuit

The planar circuit is in its receiving state activated via a uniform impulsive plane (see Fig. 9.1) defined via

$$\boldsymbol{E}^i(\boldsymbol{x}, t) = \boldsymbol{\alpha} \, e^i(t - \boldsymbol{\beta} \cdot \boldsymbol{x}/c_0) \tag{9.6}$$

$$\boldsymbol{H}^i(\boldsymbol{x}, t) = (\epsilon_0/\mu_0)^{1/2} \boldsymbol{\beta} \times \boldsymbol{\alpha} \, e^i(t - \boldsymbol{\beta} \cdot \boldsymbol{x}/c_0) \tag{9.7}$$

where $e^i(t)$ is the plane-wave signature, $\boldsymbol{\alpha}$ is the polarization vector and $\boldsymbol{\beta}$ is a unit vector in the direction of propagation. In the receiving state, the presence of the circuit is accounted for by the scattered field (cf. Eq. (8.4))

$$\{\boldsymbol{E}^s, \boldsymbol{H}^s\} = \{\boldsymbol{E}^R - \boldsymbol{E}^i, \boldsymbol{H}^R - \boldsymbol{H}^i\} \tag{9.8}$$

where superscript R denotes the total field in the receiving state. The scattered field is outside the circuit source-free and satisfies

$$\boldsymbol{\nabla} \times \boldsymbol{H}^s - \epsilon_0 \partial_t \boldsymbol{E}^s = \boldsymbol{0} \tag{9.9}$$

$$\boldsymbol{\nabla} \times \boldsymbol{E}^s + \mu_0 \partial_t \boldsymbol{H}^s = \boldsymbol{0} \tag{9.10}$$

together with the 'radiation condition' at infinity.

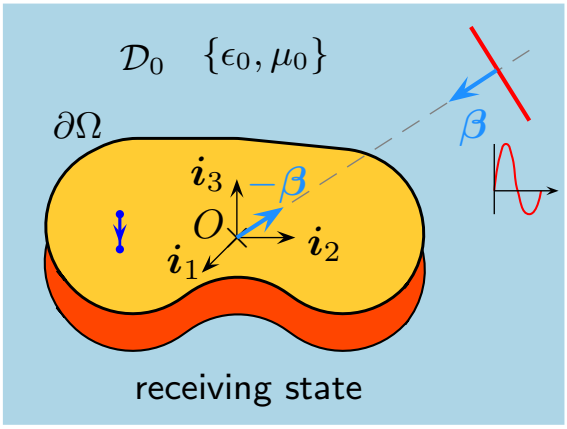

Figure 9.2: Planar circuit in its receiving state. From [106], adapted with permission from IEEE, © 2014 IEEE.

9.4 Reciprocity relations

Similarly to Sec. 8.3, the reciprocity theorem is in the first step applied to the domain exterior to the circuit and to the transmitted (T) and scattered (s) wave fields. This step yields

$$\int_{\boldsymbol{x}\in\partial\mathcal{D}} \Big[\boldsymbol{E}^T(\boldsymbol{x},t) \overset{*}{\times} \boldsymbol{H}^s(\boldsymbol{x},t) - \boldsymbol{E}^s(\boldsymbol{x},t) \overset{*}{\times} \boldsymbol{H}^T(\boldsymbol{x},t)\Big] \cdot \boldsymbol{\nu}(\boldsymbol{x})\mathrm{d}A(\boldsymbol{x}) = 0 \tag{9.11}$$

for all $t > 0$. Substitution of Eq. (9.8) in (9.11) gives

$$\begin{aligned}\int_{\boldsymbol{x}\in\partial\mathcal{D}} \Big[\boldsymbol{E}^T(\boldsymbol{x},t) \overset{*}{\times} \boldsymbol{H}^R(\boldsymbol{x},t) - \boldsymbol{E}^R(\boldsymbol{x},t) \overset{*}{\times} \boldsymbol{H}^T(\boldsymbol{x},t)\Big] \cdot \boldsymbol{\nu}(\boldsymbol{x})\mathrm{d}A(\boldsymbol{x}) \\ = \int_{\boldsymbol{x}\in\partial\mathcal{D}} \Big[\boldsymbol{E}^T(\boldsymbol{x},t) \overset{*}{\times} \boldsymbol{H}^i(\boldsymbol{x},t) - \boldsymbol{E}^i(\boldsymbol{x},t) \overset{*}{\times} \boldsymbol{H}^T(\boldsymbol{x},t)\Big] \cdot \boldsymbol{\nu}(\boldsymbol{x})\mathrm{d}A(\boldsymbol{x})\end{aligned} \tag{9.12}$$

In the second step, the reciprocity theorem is applied to the domain occupied by the circuit $\mathcal{D}$ and to the total wave fields in the both states, i.e.

$$\int_{\boldsymbol{x}\in\partial\mathcal{D}} \Big[\boldsymbol{E}^T(\boldsymbol{x},t) \overset{*}{\times} \boldsymbol{H}^R(\boldsymbol{x},t) - \boldsymbol{E}^R(\boldsymbol{x},t) \overset{*}{\times} \boldsymbol{H}^T(\boldsymbol{x},t)\Big] \cdot \boldsymbol{\nu}(\boldsymbol{x})\mathrm{d}A(\boldsymbol{x}) = \int_{\boldsymbol{x}\in\mathcal{D}} \boldsymbol{J}^T(\boldsymbol{x},t) \overset{*}{\cdot} \boldsymbol{E}^R(\boldsymbol{x},t)\mathrm{d}V(\boldsymbol{x}) \tag{9.13}$$

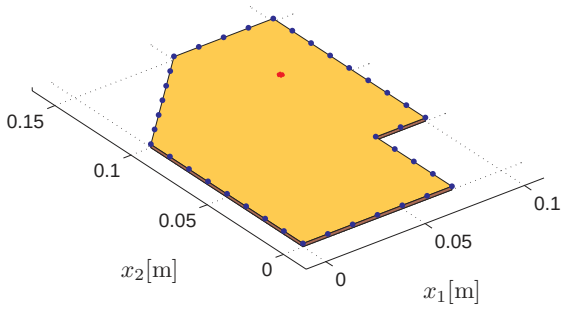

Figure 9.3: Computational model of the analyzed circuit activated by a vertical electric-current port (the dot on the patch).

In the final step, we combine (9.5) with (9.7) and (9.12) with (9.13), which finally yields

$$\boldsymbol{\alpha} \cdot \boldsymbol{E}_{\infty}^{T}(-\boldsymbol{\beta}, t) \simeq \mathcal{V}^{R}(\boldsymbol{x}^{S}, t) \tag{9.14}$$

provided that

$$e^{i}(t) = \mu_0 \partial_t \mathcal{I}^{T}(t) \tag{9.15}$$

where we have assumed the spatially concentrated vertical electric-current excitation port described via

$$\boldsymbol{J}^{T}(\boldsymbol{x}, t) = \mathcal{I}^{T}(t)\delta(\boldsymbol{x} - \boldsymbol{x}^{S})\, \boldsymbol{i}_3 \tag{9.16}$$

The final result (9.14) with (9.15) relates the pulsed EM radiation characteristics $\boldsymbol{E}_{\infty}^{T}$ of a planar circuit in the transmitting state with the pulsed-voltage response $\mathcal{V}^{R}$ on the plane wave in its receiving state. Equations (9.14) and (9.15) thus provide a means for determining the pulsed EM radiation characteristics of a thin planar antenna in the transmitting state using its reaction on the plane wave in the receiving state (see Figs. 9.2 and 9.1).

9.5 Numerical results

The derived reciprocity relation (9.14) with (9.15) is validated using FIT as implemented in CST Microwave Studio®. To this end we take four observation directions $\boldsymbol{\xi} = -\boldsymbol{\beta}$ such that the polarization and propagation vectors read

$$\boldsymbol{\alpha} = [0, \cos(\gamma), \sin(\gamma)] \tag{9.17}$$

$$\boldsymbol{\beta} = [0, -\sin(\gamma), \cos(\gamma)] \tag{9.18}$$

respectively, for $\gamma = \{3/4, 5/6, 11/12, 1\}\pi$. Note that $\boldsymbol{\alpha} \cdot \boldsymbol{\beta} = 0$. The calculations are carried out for the planar circuit shown in Fig. 9.3. The dielectric slab of the circuit has thickness $d = 1.50\,[\mathrm{mm}]$, electric permittivity $\epsilon = 4.0\epsilon_0$ and magnetic permeability $\mu = \mu_0$. The time window of observation is taken as $\{0 \leq c_0 t \leq 3.0\}\,[\mathrm{m}]$.

The planar circuit is in its transmitting state excited via the vertical electric-current port with its center at $\{x_1^T, x_2^T\} = \{75.0, 112.5\}\,[\mathrm{mm}]$. As the corresponding electric-current excitation we take the power-exponential pulse shape [80]

$$\mathcal{I}^T(t) = A(t/t_\mathrm{r})^\nu \exp[-\nu(t/t_\mathrm{r} - 1)]\mathrm{H}(t) \tag{9.19}$$

with $ct_\mathrm{w} = 0.10\,[\mathrm{m}]$, $\nu = 4$ and $A = 1.0\,[\mathrm{A}]$. The pulse time width t_w is then related to t_r and ν via $t_\mathrm{w} = t_\mathrm{r}\, \nu^{-\nu-1}\Gamma(\nu+1)\exp(\nu)$ where $\Gamma(x)$ is the Euler gamma function. The corresponding electric-current excitation signature $\mathcal{I}^T$ for the transmitting state and the electric-field plane-wave signature e^i in the receiving state are shown in Fig. 9.4. In the transmitting state, the circuit is excited by the electric-current excitation pulse and the pulsed radiation field is observed using the 'far-field probes'. The obtained transmitted electric-field vector $\boldsymbol{E}_\infty^T(-\boldsymbol{\beta}, t)$ is then projected onto the polarization direction specified by $\boldsymbol{\alpha}$. Subsequently, the TD voltage responses $\mathcal{V}^R$ on the corresponding pulsed plane waves are evaluated in the receiving state. The results are shown in Figs. 9.5–9.6. As can be observed, the pulse shapes evaluated in the transmitting and the receiving state overlap each other validating the introduced (time-derivative) reciprocity relation (9.14)–(9.15). Since these pulses were evaluated via two distinct ways, we may conclude that the CST Microwave Studio® has passed the consistency check very well.

9.6 Conclusions

Self-reciprocity properties of a planar one-port circuit has been closely studied in TD. The derived transmission-reception 'time-derivative' self-reciprocity relation links the planar circuit's pulsed EM radiation characteristics to its pulsed-voltage response to a plane wave in the receiving situation. It has been shown that the introduced relation is applicable to consistency benchmarking of purely numerical EM solvers.

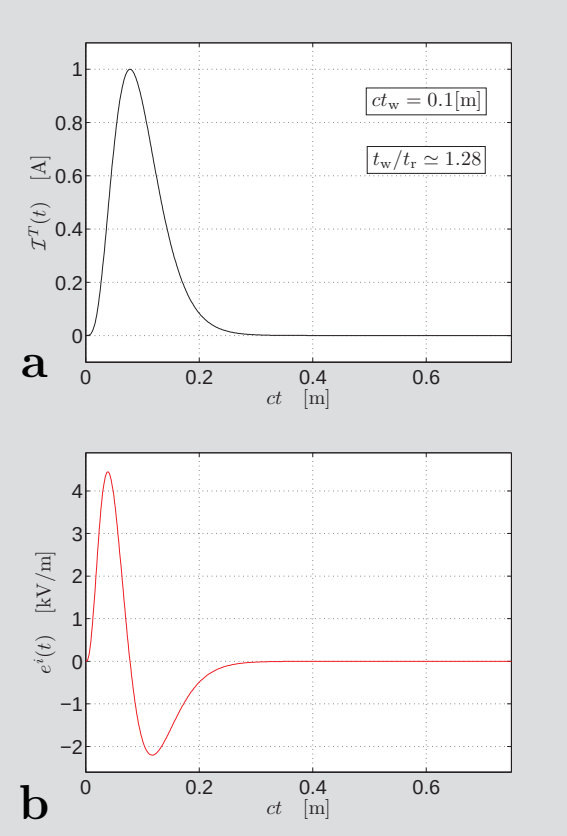

Figure 9.4: Excitation pulse shapes. (a) The power-exponential electric-current signature in the transmitting state; (b) the plane-wave signature in the receiving state.

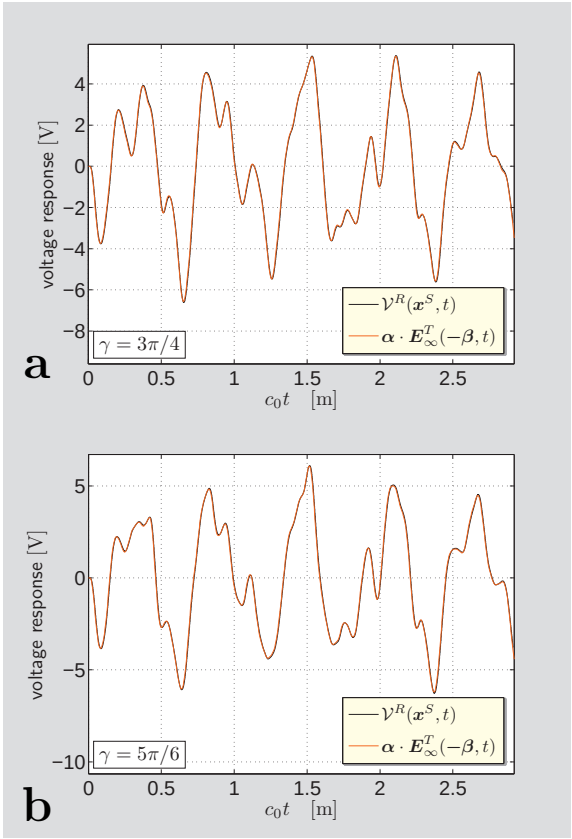

Figure 9.5: The pulsed voltage responses on the plane-wave excitation and the co-polarized pulsed radiation electric-field characteristics at $\boldsymbol{\xi} = -\boldsymbol{\beta}$ specified by (a) $\gamma = 3\pi/4$; (b) $\gamma = 5\pi/6$. From [106], adapted with permission from IEEE, © 2014 IEEE.

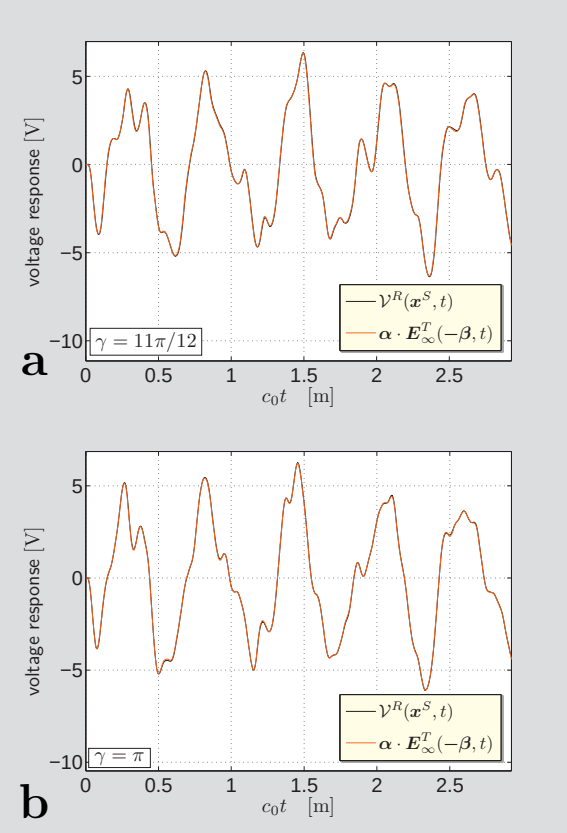

Figure 9.6: The pulsed voltage responses on the plane-wave excitation and the co-polarized pulsed radiation electric-field characteristics at $\boldsymbol{\xi} = -\boldsymbol{\beta}$ specified by (a) $\gamma = 11\pi/12$; (b) $\gamma = \pi$. From [106], adapted with permission from IEEE, © 2014 IEEE.

Chapter 10

Thévenin's circuit of an N-port planar circuit

The Kirchhoff-type equivalent representation of an antenna system is a corollary of the Lorentz reciprocity theorem of the time-convolution type that illuminates their transmission/reception properties and thus facilitates efficient design and measurement methodologies. In EMC, the objective is to secure the proper operation of an electronic device in the presence of an EM disturbance (i.e. the receiving state) without introducing intolerable EM emissions (i.e the transmitting state). Accordingly, the relation between the transmitting and receiving situations is of particular interest in EMC, too (e.g. [72, Ch. 8]).

The transmitting state of parallel-plane structures is traditionally studied with the aid of the cavity model that has proved to be computationally efficient and physically instructive in analyzing such structures of simple [49, 107] as well as irregular shapes [108, 115]. For the corresponding EM radiated susceptibility analysis concerning the plane-wave coupling into PCB traces, efficient computational models have been proposed and successfully validated (e.g. [50]). Despite the well-know benefits from applying the property of reciprocity (e.g. [6]), it seems that its potentialities in analyzing radiated EM emissions/susceptibility of planar circuits have not been fully appreciated so far. Indeed, except for the reciprocity-based calculations in transmission-line theory (see e.g. [97, Sec. 7.5.2]), the vast majority of relevant works on the subject keep the transmission and reception situations apart. Hence, the main purpose of this chapter[1] is to generalize the results of Chapter 9 and introduce a reciprocity-based description that will shed some light on the

[1]This chapter is largely based on Reference [112]. Adapted with permission from IEEE, © 2016 IEEE.

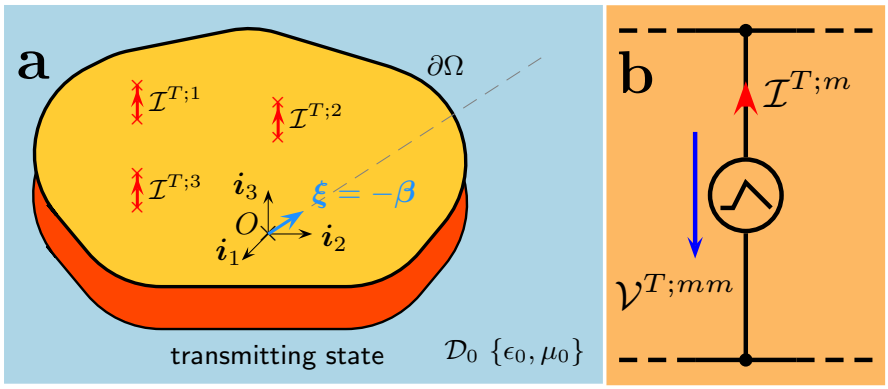

Figure 10.1: Transmitting state. (a) Emitting N-port planar circuit; (b) a feeding port. From [112], adapted with permission from IEEE, © 2016 IEEE.

transmitting/receiving states of N-port planar circuits.

The following sections are organized as follows. After introducing the problem configuration in Sec. 10.1, a reciprocity-based analysis of an N-port planar circuit is carried out. This analysis results in the N-port Thévenin-network representation of a planar circuit, which is the main result of this chapter. Subsequently, application of the result is illustrated on a 2-port planar circuit, whose equivalent circuit is discussed in detail. Specifically, it is shown how the equivalent circuit can be applied to calculate the circuit's pulsed EM radiation characteristics. Finally, the obtained results are validated using FIT.

10.1 Model definition

Let us analyze a multiport planar circuit that occupies a domain $\mathcal{D} \subset \mathbb{R}^3$ bounded by $\partial\mathcal{D} \subset \mathbb{R}^2$. The circuit is placed in the linear, isotropic, homogeneous and loss-free embedding $\mathcal{D}_0$ whose EM properties are described by its electric permittivity ϵ_0 and magnetic permeability μ_0. The corresponding EM wave speed is $c_0 = (\epsilon_0\mu_0)^{-1/2} > 0$. The EM properties of the dielectric slab are described by its electric permittivity ϵ and magnetic permeability μ_0. The electrically conducting plate of the circuit occupies a surface domain $\Omega \subset \partial\mathcal{D}$ bounded by its rim $\partial\Omega \subset \mathbb{R}$. The normal outer unit vector is denoted by $\boldsymbol{\nu}$. In the following sections we find a reciprocity relation between transmitting and receiving properties of an N-port planar circuit.

10.2 Transmitting state of an N-port planar circuit

The planar circuit is in the transmitting state (see Fig. 10.1) activated by vertical electric-current ports whose action is accounted for by the electric-current volume density $\boldsymbol{J}^T(\boldsymbol{x}|\boldsymbol{x}^m, t)$, for $m = \{1, \ldots, N\}$, where $\boldsymbol{x}^m$ is the position and $\mathcal{I}^{T;m}$ denotes the electric-current pulse shape of the m-th port. The corresponding pulsed voltage response $\mathcal{V}^{T;nm}$ at $\boldsymbol{x}^n$ is linearly related to the excitation current at $\boldsymbol{x}^m$ via

$$\mathcal{V}^{T;nm}(t) = \mathcal{Z}^{T;nm}(t) * \mathcal{I}^{T;m}(t) \tag{10.1}$$

for $n = \{1, \ldots, N\}$, where $\mathcal{Z}^{T;nm}$ is the corresponding transfer impedance. Consequently, the planar circuit manifests itself via the transmitted EM wave field $\{\boldsymbol{E}^T, \boldsymbol{H}^T\}(\boldsymbol{x}, t)$ radiated into the embedding where it admits the far-field expansion [20, Sec. 26.12]

$$\begin{aligned}\{\boldsymbol{E}^T, \boldsymbol{H}^T\}(\boldsymbol{x}, t) \;=\; & \sum_{m=1}^{N} \frac{\{\boldsymbol{E}^T_\infty, \boldsymbol{H}^T_\infty\}(\boldsymbol{\xi}, t - |\boldsymbol{x}|/c_0)|_{\mathcal{I}^{T;m}(t)=\delta(t)}}{4\pi|\boldsymbol{x}|} * \mathcal{I}^{T;m}(t) \\ & [1 + \mathcal{O}(|\boldsymbol{x}|^{-1})]\end{aligned} \tag{10.2}$$

as $|\boldsymbol{x}| \to \infty$, where $\{\boldsymbol{E}^T_\infty, \boldsymbol{H}^T_\infty\} = \{\boldsymbol{E}^T_\infty, \boldsymbol{H}^T_\infty\}(\boldsymbol{\xi}, t)$ are the electric- and magnetic-field vector radiation characteristics, respectively, and $\boldsymbol{\xi} = \boldsymbol{x}/|\boldsymbol{x}|$ is the unit vector in the direction of observation. The TD surface-source radiation-characteristics representation follows as [106, Eq. (8)]

$$\begin{aligned}\mathbf{I}_t \boldsymbol{E}^T_\infty(\boldsymbol{\xi}, t) = \mu_0 \boldsymbol{\xi} \times \boldsymbol{\xi} \times & \int_{\boldsymbol{x} \in \partial\mathcal{D}} \boldsymbol{\nu}(\boldsymbol{x}) \times \boldsymbol{H}^T(\boldsymbol{x}, t + \boldsymbol{\xi} \cdot \boldsymbol{x}/c_0) \mathrm{d}A(\boldsymbol{x}) \\ & - c_0^{-1} \boldsymbol{\xi} \times \int_{\boldsymbol{x} \in \partial\mathcal{D}} \boldsymbol{\nu}(\boldsymbol{x}) \times \boldsymbol{E}^T(\boldsymbol{x}, t + \boldsymbol{\xi} \cdot \boldsymbol{x}/c_0) \mathrm{d}A(\boldsymbol{x})\end{aligned} \tag{10.3}$$

with $\boldsymbol{\xi} \times \boldsymbol{E}^T_\infty = \eta_0 \boldsymbol{H}^T_\infty$ and $\boldsymbol{\xi} \cdot \boldsymbol{E}^T_\infty = 0$.

10.3 Receiving state of an N-port planar circuit

Similarly to Sec. 9.3, the planar circuit is in its receiving situation (see Fig. 10.2) irradiated by an uniform plane wave defined in Eqs. (9.6) and (9.7). The total field in the configuration $\{\boldsymbol{E}^R, \boldsymbol{H}^R\}(\boldsymbol{x}, t)$ is then the superposition

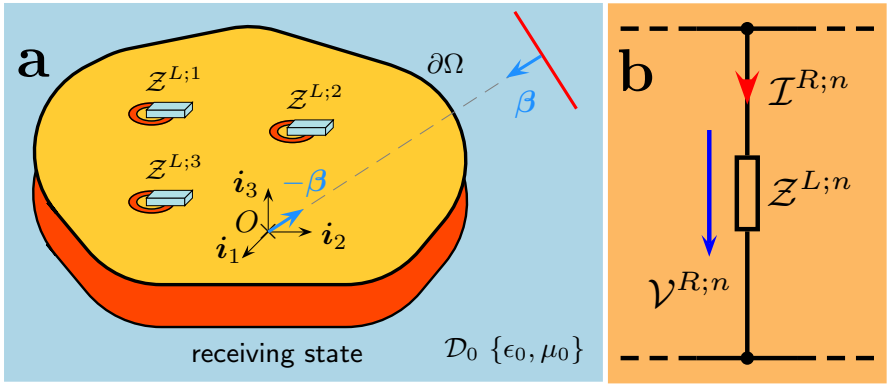

Figure 10.2: Receiving state. (a) Receiving N-port planar circuit; (b) a load impedance. From [112], adapted with permission from IEEE, © 2016 IEEE.

of the incident field $\{\boldsymbol{E}^i, \boldsymbol{H}^i\}(\boldsymbol{x}, t)$ and the scattered field $\{\boldsymbol{E}^s, \boldsymbol{H}^s\}(\boldsymbol{x}, t)$ that is thus defined according to Eq. (9.8).

The planar structure is at $\boldsymbol{x}^n$, for $n = \{1, \ldots, N\}$, loaded by lumped impedances. The corresponding electric-current volume density is then described via $\boldsymbol{J}^R(\boldsymbol{x}, t)$, with $\mathcal{I}^{R;n}$ being the (induced) electric current flowing across the n-th load. The voltage across the load is then linearly related to the load current according to

$$\mathcal{V}^{R;n}(t) = \mathcal{Z}^{L;n}(t) * \mathcal{I}^{R;n}(t) \tag{10.4}$$

where $\mathcal{Z}^{L;n}$ denotes n-th load's impedance.

10.4 Reciprocity relations

The present reciprocity analysis overlaps in part with the one given in Sec. 9.4. At first, combination of the surface-integral representation of the transmitted-field radiation amplitude (10.3) with Eqs. (9.6)–(9.7) results in the following interaction integral

$$\int_{\boldsymbol{x}\in\partial\mathcal{D}} \Big[\boldsymbol{E}^T(\boldsymbol{x}, t) \overset{*}{\times} \boldsymbol{H}^i(\boldsymbol{x}, t) - \boldsymbol{E}^i(\boldsymbol{x}, t) \overset{*}{\times} \boldsymbol{H}^T(\boldsymbol{x}, t)\Big] \cdot \boldsymbol{\nu}(\boldsymbol{x}) \mathrm{d}A(\boldsymbol{x})$$
$$= -\mu_0^{-1} \boldsymbol{\alpha} e^i(t) \overset{*}{\cdot} \mathbf{I}_t \boldsymbol{E}_\infty^T(-\boldsymbol{\beta}, t) \tag{10.5}$$

Thanks to the fact that the transmitted and scattered wave fields are causal and that the embedding is self-adjoint in its EM behavior we can further

write

$$\int_{\boldsymbol{x}\in\partial\mathcal{D}} \Big[\boldsymbol{E}^T(\boldsymbol{x},t) \overset{*}{\times} \boldsymbol{H}^s(\boldsymbol{x},t) - \boldsymbol{E}^s(\boldsymbol{x},t) \overset{*}{\times} \boldsymbol{H}^T(\boldsymbol{x},t)\Big] \cdot \boldsymbol{\nu}(\boldsymbol{x})\mathrm{d}A(\boldsymbol{x}) = 0 \tag{10.6}$$

which in combination with (10.5) and (9.8) leads to

$$\int_{\boldsymbol{x}\in\partial\mathcal{D}} \Big[\boldsymbol{E}^T(\boldsymbol{x},t) \overset{*}{\times} \boldsymbol{H}^R(\boldsymbol{x},t) - \boldsymbol{E}^R(\boldsymbol{x},t) \overset{*}{\times} \boldsymbol{H}^T(\boldsymbol{x},t)\Big] \cdot \boldsymbol{\nu}(\boldsymbol{x})\mathrm{d}A(\boldsymbol{x}) = -\mu_0^{-1}\boldsymbol{\alpha}e^i(t) \overset{*}{\cdot} \mathbf{I}_t\boldsymbol{E}_\infty^T(-\boldsymbol{\beta},t) \tag{10.7}$$

Application of the reciprocity theorem to the domain occupied by the planar circuit and to the total fields in the transmitting and receiving situations yields

$$\begin{aligned}&\int_{\boldsymbol{x}\in\partial\mathcal{D}} \Big[\boldsymbol{E}^T(\boldsymbol{x},t) \overset{*}{\times} \boldsymbol{H}^R(\boldsymbol{x},t) - \boldsymbol{E}^R(\boldsymbol{x},t) \overset{*}{\times} \boldsymbol{H}^T(\boldsymbol{x},t)\Big] \cdot \boldsymbol{\nu}(\boldsymbol{x})\mathrm{d}A(\boldsymbol{x})\\ &= \int_{\boldsymbol{x}\in\mathcal{D}} \Big[\boldsymbol{J}^T(\boldsymbol{x},t) \overset{*}{\cdot} \boldsymbol{E}^R(\boldsymbol{x},t) - \boldsymbol{J}^R(\boldsymbol{x},t) \overset{*}{\cdot} \boldsymbol{E}^T(\boldsymbol{x},t)\Big]\mathrm{d}V(\boldsymbol{x})\end{aligned} \tag{10.8}$$

where we have assumed that the medium in $\mathcal{D}$ is self-adjoint in its EM properties. Subsequently, combination of (10.7) with (10.8) leads to

$$\int_{\boldsymbol{x}\in\mathcal{D}} \Big[\boldsymbol{J}^T(\boldsymbol{x},t) \overset{*}{\cdot} \boldsymbol{E}^R(\boldsymbol{x},t) - \boldsymbol{J}^R(\boldsymbol{x},t) \overset{*}{\cdot} \boldsymbol{E}^T(\boldsymbol{x},t)\Big]\mathrm{d}V(\boldsymbol{x}) = -\mu_0^{-1}\boldsymbol{\alpha}e^i(t) \overset{*}{\cdot} \mathbf{I}_t\boldsymbol{E}_\infty^T(-\boldsymbol{\beta},t) \tag{10.9}$$

Owing to the thin-slab assumption, the latter relation can be rewritten as

$$\mathcal{I}^{T;m}(t) * \mathcal{V}^{R;m}(t) + \sum_{n=1}^{N} \mathcal{I}^{R;n}(t) * \mathcal{V}^{T;nm}(t) = \mu_0^{-1}\boldsymbol{\alpha}e^i(t) \overset{*}{\cdot} \mathbf{I}_t\boldsymbol{E}_\infty^T(-\boldsymbol{\beta},t) \tag{10.10}$$

for $m = \{1,\ldots,N\}$, where the orientation of the source/load currents and voltages is depicted in Figs. 10.1b and 10.2b. Equation (10.10) makes possible to introduce Norton's and Thévenin's equivalent network of an N-port planar circuit. As these equivalent circuits are fully equivalent [25], we shall further limit our analysis to the Thévenin network only. To this end, we assume

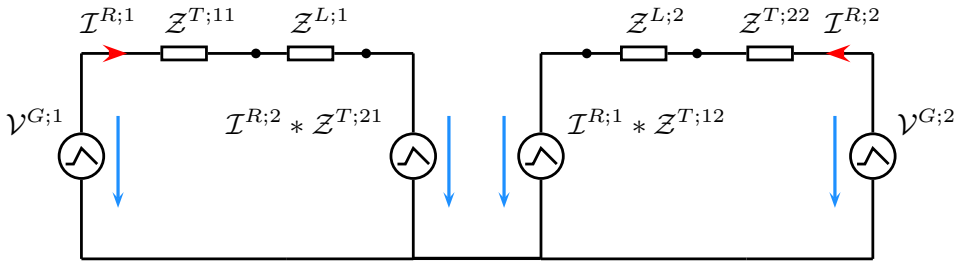

Figure 10.3: Equivalent circuit of a 2-port planar circuit.

that the planar circuit is in its transmitting state activated by prescribed electric-current source signatures $\mathcal{I}^{T;m}$ and rewrite Eq. (10.10) as

$$\mathcal{V}^{R;m}(t) + \sum_{n=1}^{N} \mathcal{Z}^{T;nm}(t) * \mathcal{I}^{R;n}(t) = \mathcal{V}^{G;m}(t) \tag{10.11}$$

with

$$\mathcal{V}^{G;m}(t) = \mu_0^{-1} \boldsymbol{\alpha} e^{i}(t) \overset{*}{\cdot} \mathbf{I}_t \boldsymbol{E}_{\infty}^{T}(-\boldsymbol{\beta}, t)|_{\mathcal{I}^{T;m}(t)=\delta(t)} \tag{10.12}$$

for $m = \{1, \ldots, N\}$, being the Thévenin voltage generator. Equations (10.11) and (10.12) define the Thévenin network representation of an N-port planar circuit. The conditions under which the impedance matrix $\mathcal{Z}^{\mathrm{T}}$ is symmetrical have been discussed in [112].

10.5 An illustrative example

The main result of the previous section will be next illustrated on a 2-port planar circuit. The relevant definition equations follow directly from Eq. (10.11) for $N = 2$, here given in the explicit matrix form

$$\begin{pmatrix} \mathcal{V}^{G;1} \\ \mathcal{V}^{G;2} \end{pmatrix} = \begin{pmatrix} \mathcal{V}^{R;1} \\ \mathcal{V}^{R;2} \end{pmatrix} + \begin{pmatrix} \mathcal{Z}^{T;11} & \mathcal{Z}^{T;21} \\ \mathcal{Z}^{T;12} & \mathcal{Z}^{T;22} \end{pmatrix} * \begin{pmatrix} \mathcal{I}^{R;1} \\ \mathcal{I}^{R;2} \end{pmatrix} \tag{10.13}$$

A network representation of the 2-port planar circuit is then shown in Fig. 10.3.

Next it is observed that we may decouple the system of equations (10.13) by taking its special cases, namely the open-circuited port 2 for which $\mathcal{I}^{R;2} = 0$, i.e.

$$\mathcal{V}^{R;1}(t) + \mathcal{Z}^{T;11}(t) * \mathcal{I}^{R;1}(t) = \mathcal{V}^{G;1}(t) \tag{10.14}$$

$$\mathcal{V}^{R;2}(t) + \mathcal{Z}^{T;12}(t) * \mathcal{I}^{R;1}(t) = \mathcal{V}^{G;2}(t) \tag{10.15}$$

and, the case when port 1 is open-circuited, i.e. $\mathcal{I}^{R;1} = 0$, which implies

$$\mathcal{V}^{R;1}(t) + \mathcal{Z}^{T;21}(t) * \mathcal{I}^{R;2}(t) = \mathcal{V}^{G;1}(t) \tag{10.16}$$

$$\mathcal{V}^{R;2}(t) + \mathcal{Z}^{T;22}(t) * \mathcal{I}^{R;2}(t) = \mathcal{V}^{G;2}(t) \tag{10.17}$$

Now, taking into account relation (10.12) it is seen that we may use either Eq. (10.14) or (10.16) to calculate the pulsed EM characteristics due to the electric-current source of port 1, i.e. $\mathcal{I}^{T;1}$, while the use of either Eq. (10.15) or (10.17) leads to the pulsed EM characteristics due to $\mathcal{I}^{T;2}$. In the numerical examples that follow we shall consider the former case and rewrite the corresponding equations to the form that is practical for our calculations, namely

$$\begin{aligned} &\mathcal{I}^{T;1}(t) * \mathcal{V}^{R;1}(t) + \mathcal{V}^{T;11}(t) * \mathcal{I}^{R;1}(t) \\ &\qquad = \mathcal{I}^{T;1}(t) * \mathcal{V}^{G;1}(t) \text{ for } \mathcal{I}^{R;2}(t) = 0 \end{aligned} \tag{10.18}$$

$$\begin{aligned} &\mathcal{I}^{T;1}(t) * \mathcal{V}^{R;1}(t) + \mathcal{V}^{T;21}(t) * \mathcal{I}^{R;2}(t) \\ &\qquad = \mathcal{I}^{T;1}(t) * \mathcal{V}^{G;1}(t) \text{ for } \mathcal{I}^{R;1}(t) = 0 \end{aligned} \tag{10.19}$$

The procedure then goes along the following lines

- For a given excitation pulse $\mathcal{I}^{T;1}$, calculate (or measure) the pulsed voltage responses $\mathcal{V}^{T;11}$ or $\mathcal{V}^{T;21}$ in the transmitting state. Such calculations can be readily carried out using TD-CIM.

- For the corresponding plane-wave pulse e^i (see Eq. (10.21)), calculate (or measure) the pulsed voltage or/and current responses $\{\mathcal{V}^{R;1}, \mathcal{I}^{R;1}\}$ with $\mathcal{I}^{R;2} = 0$ or $\{\mathcal{V}^{R;1}, \mathcal{I}^{R;2}\}$ with $\mathcal{I}^{R;1} = 0$.

- With the pulsed responses at our disposal we can perform the operations indicated in Eq. (10.18) or (10.19) and get $\mathcal{I}^{T;1} * \mathcal{V}^{G;1}$. Recovery of $\mathcal{V}^{G;1}$ apparently calls for a deconvolution algorithm. An example of the latter is specified in the following Sec. 10.6.

- The Thévenin voltage generator $\mathcal{V}^{G;1}$ is subsequently identified with the corresponding TD EM radiation characteristics via (cf. Eq. (10.12))

  $$\mathcal{V}^{G;1}(t) = \boldsymbol{\alpha} \cdot \boldsymbol{E}^T_\infty(-\boldsymbol{\beta}, t)|_{\mathcal{I}^{T;1}(t)=\delta(t)} * \mathcal{I}^{T;1}(t) \tag{10.20}$$

  provided that the plane-wave signature is related to the electric-current pulse shape in the following way

  $$e^i(t) = \mu_0 \partial_t \mathcal{I}^{T;1}(t) \tag{10.21}$$

Finally note that Eqs. (10.20)–(10.21) are known as the transmission-reception time-derivative relation [106, Sec. IVb].

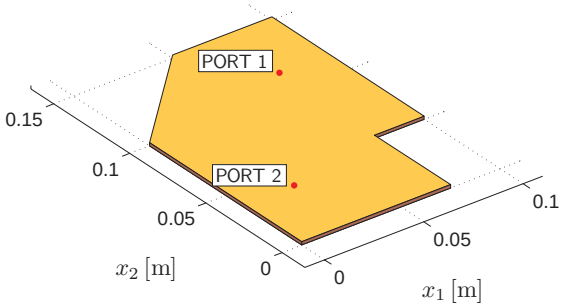

Figure 10.4: Computational model of the analyzed circuit with two accessible ports (the dots on the patch). From [112], adapted with permission from IEEE, © 2016 IEEE.

10.6 Numerical results

In order to validate the proposed methodology, the irregularly-shaped planar circuit shown in Fig. 10.4 is analyzed. Its accessible ports are placed at $\boldsymbol{x}^1 = \{75.0, 112.5, 0\}$ [mm] (PORT 1) and at $\boldsymbol{x}^2 = \{25.0, 37.5, 0\}$ [mm] (PORT 2), its thickness is taken as $d = 1.50$ [mm] and the relative permittivity of the dielectric slab is $\epsilon_\mathrm{r} = 4.2$. The corresponding EM wave speed in the slab is $c = c_0/\sqrt{\epsilon_\mathrm{r}}$. For validation purposes, the transmitting state is analyzed using TD-CIM, while the pulsed responses in the receiving situation are evaluated with the help of FIT of CST Microwave Studio®.

According to the methodology outlined in Sec. 10.5, the planar circuit is first analyzed in its transmitting state. To this end, the planar structure is activated at its PORT 1 by the electric-current pulse defined in Appendix D with the amplitude $A = 1.0$ [A] and the spatial pulse width $ct_\mathrm{w} = 0.15$ (m) (see Fig. 10.5a). The resulting pulsed-voltage responses $\mathcal{V}^{T;11}$ and $\mathcal{V}^{T;21}$ at PORT 1 and PORT 2 are shown in Figs. 10.6a and 10.6b, respectively. In the second step, the structure is irradiated by the incident uniform plane-wave (see Eqs. (9.6) and (9.7)) whose polarization and direction of propagation is defined according to Eqs. (9.17) and (9.18) where we substitute $\gamma = 5\pi/6$, for the present example. The plane-wave pulse shape calculated from Eq. (10.21) is shown in Fig. 10.5b. In line with Eqs. (10.18) and (10.19), we distinguish between two receiving situations. In the first one pertaining to Eq. (10.18), PORT 2 is left open-circuited (i.e. $\mathcal{I}^{R;2} = 0$) and we calculate the pulsed response $\mathcal{V}^{R;1}$ at PORT 1. For this case we have chosen the purely resistive (instantaneously-reacting) load $\mathcal{Z}^{L;1}(t) = R^{L;1}\delta(t)$ with $R^{L;1} = 240.0$ [Ω] and calculated the pulsed-voltage response across the element. The result is plotted in Fig. 10.7a. Since the corresponding electric-current response $\mathcal{I}^{R;1}$ is

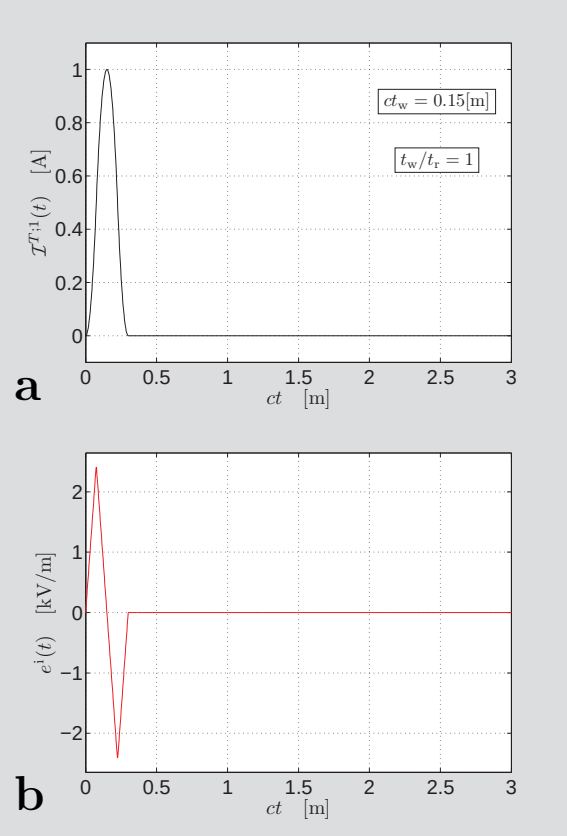

Figure 10.5: Excitation pulse shapes. (a) The bell-shaped electric-current signature in the transmitting state; (b) the plane-wave signature in the receiving state.

just a scaled copy of $\mathcal{V}^{R;1}$, its plot is omitted.

The second receiving state is associated with Eq. (10.19) and corresponds to the situation with the open-circuited PORT 1 (i.e. $\mathcal{I}^{R;1} = 0$). In this case, we have calculated the open-circuited voltage response $\mathcal{V}^{R;1}$ and the electric-current pulse $\mathcal{I}^{R;2}$ in the chosen capacitive impedance $\mathcal{Z}^{L;2}(t) = (C^{L;2})^{-1}\mathrm{H}(t)$ at PORT 2 with $C^{L;2} = 500\,[\mathrm{pF}]$. The resulting pulse shapes are shown in Figs. 10.7b and 10.7c, respectively.

With all the signals at hand we may evaluate the time convolutions on the left-hand sides of Eqs. (10.18) and (10.19) and get $\mathcal{Q}(t) = \mathcal{I}^{T;1}(t) * \mathcal{V}^{G;1}(t)$. For the electric-current excitation pulse specified in Appendix D, the closed-form deconvolution algorithm that yields $\mathcal{V}^{G;1}$ at once does exist, viz

$$\mathcal{V}^{G;1}(t) = \frac{t_w^2}{4A}\sum_{n=0}^{\infty}\frac{2(n+2)^2 - 1 + (-1)^{n+2}}{8}\partial_t^3\mathcal{Q}(t - nt_w/2) \qquad (10.22)$$

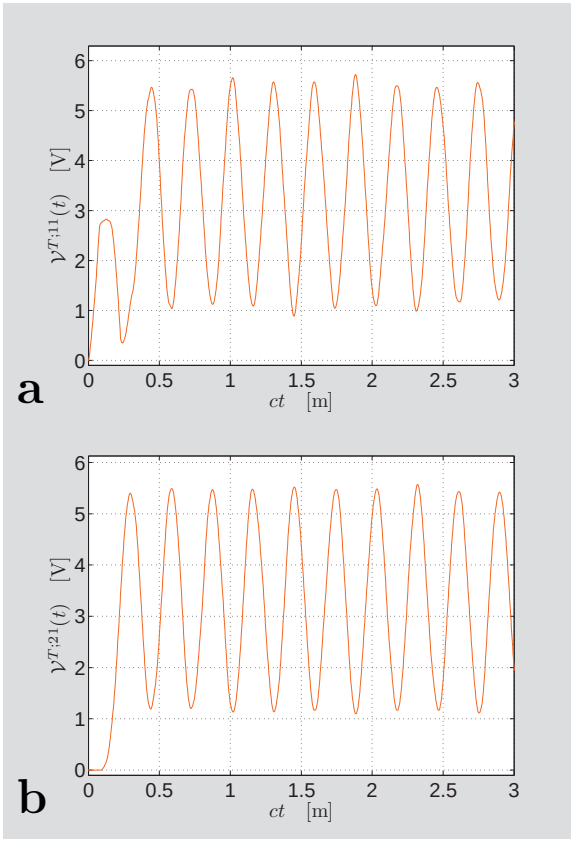

Figure 10.6: The pulsed voltage responses in the transmitting situation that are observed at (a) PORT 1; (b) PORT 2. From [112], adapted with permission from IEEE, © 2016 IEEE.

Obviously, the number of terms in (10.22) is finite in any (bounded) time-window of observation.

The sought pulse shapes of the pulsed EM radiation characteristics as calculated from Eqs. (10.18)–(10.19) are shown in Fig. 10.8. In order to validate the results, the radiated electric field has also been evaluated with the help of the 'far-field probes' implemented in CST Microwave Studio®. As can be seen, the final results agree very well. The visible discrepancy in the late part of the response found from (10.19) is largely attributed to fact that $\mathcal{V}^{T;21}$ was obtained upon integrating the space-time voltage distribution along the circuit rim (see Eq. (2.37)) under the thin-slab assumption implicit in the formulation of TD-CIM. Obviously, the additional contour integration as well as the thin-slab approximation introduce errors that typically manifest themselves in the late-part of the response.

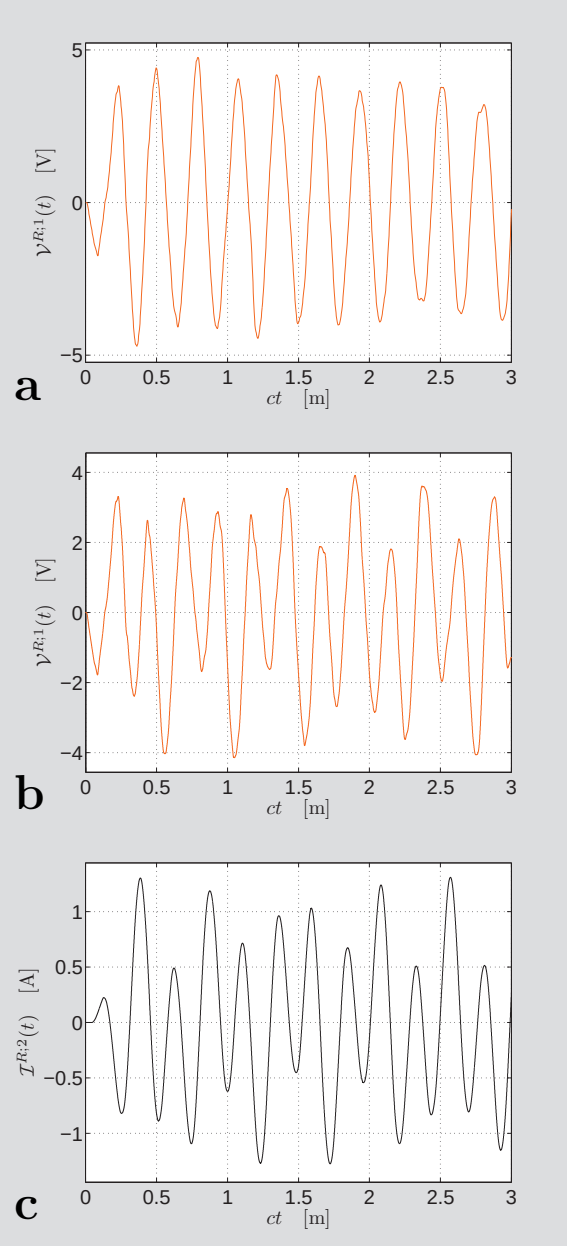

Figure 10.7: The pulsed responses in the receiving situation. (a) Voltage across $R^{L;1}$ at PORT 1; (b) open-circuited voltage at PORT 1 with $C^{L;2}$ connected at PORT 2; (c) electric current across $C^{L;2}$ at PORT 2 with PORT 1 open-circuited.

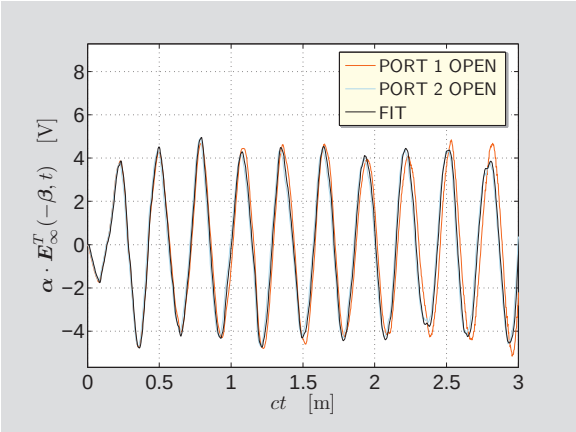

Figure 10.8: Pulsed EM radiation characteristics evaluated via Eq. (10.18) (PORT 2 open-circuited), Eq. (10.19) (PORT 1 open-circuited) and the 'far-field probes' of the referential FIT. From [112], adapted with permission from IEEE, © 2016 IEEE.

10.7 Conclusions

Thévenin's equivalent network of a planar circuit with N accessible ports has been constructed with the aid of the TD reciprocity theorem of the time-convolution type. As has been demonstrated, such a representation closely relates the transmitting and receiving states of the planar circuit and may hence provide new physical insights into its radiation and reception pulsed EM-field behavior. Furthermore, the presented description may reveal new reciprocity relations that can be applied to benchmark purely numerical EM solvers. Consistency of the proposed equivalent-network representation has been validated with the aid of TD-CIM and (three-dimensional) Finite-Integration Technique (FIT).

Chapter 11

Time-domain radiated susceptibility of a planar circuit

The two-dimensional cavity model as formulated in Sec. 2.1 proved to be useful and efficient for analyzing the radiation characteristics of planar circuits (see Chapter 7). Based on reciprocity considerations, it may be hence anticipated that this model will do well in the corresponding receiving situation in which a planar circuit is irradiated by an external EM source. The confirmation of this expectation is basically a spin-off of the present chapter, where straightforward expressions for the efficient calculation of the pulsed-voltage response to an external EM disturbance are constructed.

Closely related scattering problems are dominantly solved using the standard real-FD numerical techniques. Examples in this category are Method-of-Moments-based solutions [63, 75] or the Finite-Element-based analysis concerning a microstrip structure and related topologies (see [10, 117], for example). As to EM plane-wave coupling, the previous works on the subject analyze the aperture coupling to a perfectly-conducting box [65, 88, 91] and approximate models of a PCB trace [8, 50], for instance, relying on the classical transmission-line theory [97, Chapter 7].

In this chapter[1], the reciprocity theorem of the time-convolution type is applied to express the pulsed voltage induced within a planar circuit via a straightforward one-dimensional integration of the testing (or auxiliary) field distribution along a circuit periphery. As is shown, this approach is in particular efficient when combined with TD-CIM, whose basic formulation was introduced in Sec. 3, or the TD ray-type Green's function representation as given in Sec. 5, for example. While the former leads directly to the required

[1]This chapter is largely based on Reference [111].

space-time testing voltage distribution on the circuit's rim, the latter expresses the solution in terms of (a finite number of) the causality-preserving TD 'generalized-ray' constituents. In this way, the introduced methodology makes possible to readily evaluate the TD radiated susceptibility of a planar circuit with very low computational efforts and yet reasonable accuracy.

11.1 Reciprocity relations

Let us, again, assume a planar circuit that is, in its receiving state (see Fig. 9.2), irradiated by an impulsive plane wave defined via Eqs. (9.6) and (9.7). The receiving circuit is again placed in the linear, isotropic, homogeneous and loss-free embedding $\mathcal{D}_0$ whose EM properties are described by its electric permittivity ϵ_0 and magnetic permeability μ_0. The corresponding EM wave speed is $c_0 = (\epsilon_0\mu_0)^{-1/2} > 0$. The EM properties of the dielectric slab are described by its electric permittivity ϵ and magnetic permeability μ_0. The electrically conducting plate of the circuit occupies a surface domain $\Omega^R \subset \partial\mathcal{D}^R$ bounded by its rim $\partial\Omega^R \subset \mathbb{R}$. The normal outer unit vector is denoted by $\boldsymbol{\nu}$, while the corresponding tangent vector is $\boldsymbol{\tau} = \boldsymbol{i}_3 \times \boldsymbol{\nu}$.

In order to describe the TD radiated susceptibility in closed form, we follow in part the procedure described in Sec. 8.3. Upon enforcing the magnetic-wall boundary condition for the testing field state, Eq. (8.7) can be, under the thin-slab approximation, rewritten as

$$\int_{\boldsymbol{x}'\in\partial\Omega^R} \mathcal{V}^B(\boldsymbol{x}'|\boldsymbol{x}^S,t) * \boldsymbol{\tau}(\boldsymbol{x}') \cdot \boldsymbol{H}^R(\boldsymbol{x}',t)\mathrm{d}l(\boldsymbol{x}') = \int_{\boldsymbol{x}'\in\partial\Omega^R} \mathcal{V}^B(\boldsymbol{x}'|\boldsymbol{x}^S,t) * \boldsymbol{\tau}(\boldsymbol{x}') \cdot \boldsymbol{H}^i(\boldsymbol{x}',t)\mathrm{d}l(\boldsymbol{x}') \qquad (11.1)$$

for all $t > 0$, where $\mathcal{V}^B(\boldsymbol{x}|\boldsymbol{x}^S,t)$ denotes the testing voltage distribution along the rim of the receiving planar circuit $\partial\Omega^R$. Now it is worth noting that the tangential part (with respect to $\partial\Omega^R$) of the (total) field $\boldsymbol{H}^R$ in Eq. (11.1) should be, too, in virtue of the thin-slab approximation, taken as zero. As the TD optical (extinction) theorem [114] tells, however, the cavity model in such a case does not absorb any energy. The boundary perturbation that allows for a non-vanishing tangential part of $\boldsymbol{H}^R$ is also commonly used in the corresponding transmitting situation (see [90, Sec. 4.7] and [34, Sec. 2.3], for example).

In the second step, the reciprocity theorem is applied to the domain occupied by the receiving planar circuit and to the total-field (R) and the testing-field (B) states, which, under the thin-slab approximation, yields

(cf. Eq. (9.13))

$$\int_{\boldsymbol{x}'\in\partial\Omega^R} \mathcal{V}^B(\boldsymbol{x}'|\boldsymbol{x}^S,t) * \boldsymbol{\tau}(\boldsymbol{x}') \cdot \boldsymbol{H}^R(\boldsymbol{x}',t)\mathrm{d}l(\boldsymbol{x}') = -\mathcal{V}^R(\boldsymbol{x}^S,t) * \mathcal{I}^B(t) \tag{11.2}$$

where $\mathcal{V}^R = -dE_3^R$ is the total voltage induced in the planar circuit at $\boldsymbol{x}^S \in \Omega$. Upon combining the latter with Eq. (11.1) we end up with (cf. Eq. (8.9)

$$\mathcal{V}^R(\boldsymbol{x}^S,t) * \mathcal{I}^B(t) = -\int_{\boldsymbol{x}'\in\partial\Omega^R} \mathcal{V}^B(\boldsymbol{x}'|\boldsymbol{x}^S,t) * \boldsymbol{\tau}(\boldsymbol{x}') \cdot \boldsymbol{H}^i(\boldsymbol{x}',t)\mathrm{d}l(\boldsymbol{x}') \tag{11.3}$$

which expresses the induced (total) voltage $\mathcal{V}^R$ in the planar circuit though the testing voltage distribution $\mathcal{V}^B$ and the tangential part of the incident plane wave $\boldsymbol{H}^i$ along the circuit rim $\partial\Omega^R$. Now, taking into the account that Eq. (11.3) should hold for arbitrary $\mathcal{I}^B(t)$, we arrive at

$$\mathcal{V}^R(\boldsymbol{x}^S,t) = -d\, c_0^{-1}(\boldsymbol{\beta}\times\boldsymbol{\alpha})\partial_t e^i(t) \overset{*}{\cdot} \int_{\boldsymbol{x}'\in\partial\Omega^R} G(\boldsymbol{x}'|\boldsymbol{x}^S, t-\boldsymbol{\beta}\cdot\boldsymbol{x}'/c_0)\boldsymbol{\tau}(\boldsymbol{x}')\mathrm{d}l(\boldsymbol{x}') \tag{11.4}$$

where we have made use of (9.7) in (11.3) and

$$\mathcal{V}^B(\boldsymbol{x}|\boldsymbol{x}^S,t) = \mu_0 d\partial_t \mathcal{I}^B(t) * G(\boldsymbol{x}|\boldsymbol{x}^S,t) \tag{11.5}$$

for the concentrated electric-current testing source (8.5) (see Eq. (2.11)). Here, $G(\boldsymbol{x}|\boldsymbol{x}^S,t)$ is the two-dimensional TD Green's function whose closed-form ray and modal representations for the rectangular domain Ω^R are given in Chapter 5. This strikingly straightforward relation makes possible to readily evaluate the pulsed-voltage response to the incident impulsive plane. Owing to its simplicity it may be useful for estimating the (worst-case) pulsed radiated EM susceptibility of planar circuits.

It is interesting to note that Eq. (11.5) can also be derived from the contour-integral representation of the (time-dependent) far-field radiation characteristic (see Eq. (7.1))

$$\boldsymbol{E}_\infty^B(\boldsymbol{\xi},t) = -d\, c_0^{-1}\mu_0\partial_t^2\mathcal{I}^B(t) * \int_{\boldsymbol{x}'\in\partial\Omega^R} G^B(\boldsymbol{x}'|\boldsymbol{x}^S, t+\boldsymbol{\xi}\cdot\boldsymbol{x}'/c_0)\boldsymbol{\xi}\times\boldsymbol{\tau}(\boldsymbol{x}')\mathrm{d}l(\boldsymbol{x}') \tag{11.6}$$

and the property of self-reciprocity that relates the circuit's receiving and transmitting (or testing) states according to (9.14) and (9.15).

In the following sections, Eqs. (11.3) and (11.4) are applied to evaluate the plane-wave response $\mathcal{V}^R$ of an irregularly-shaped and a rectangular planar structure, respectively. For the former equation, the testing voltage distribution $\mathcal{V}^B$ is found via TD-CIM, while the latter makes use of the ray-type field representation as given in in Chapter 5.

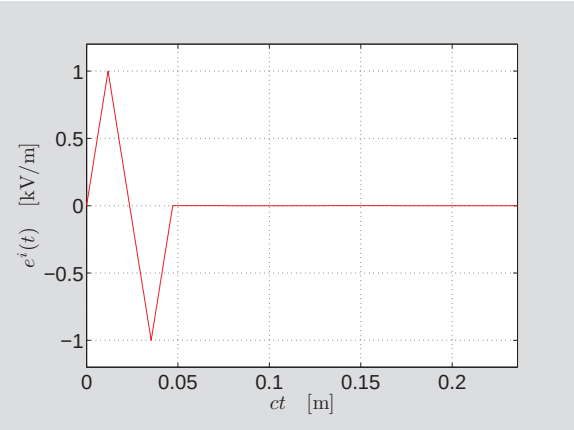

Figure 11.1: The triangular plane-wave signature. From [111], adapted with permission from Taylor & Francis, © 2016 Taylor & Francis.

11.2 Numerical results

The pulsed voltage response of both irregularly-shaped and rectangular planar structures is evaluated via Eqs. (11.3) and (11.4), respectively, and the referential Finite-Integration Technique (FIT) as implemented in CST Microwave Studio®. The circuits are irradiated by the (impulsive) incident plane wave that is defined via its polarization and propagation vectors (cf. Eqs. (9.6)–(9.7))

$$\boldsymbol{\alpha} = [\cos(\phi)\cos(\theta), \sin(\phi)\cos(\theta), -\sin(\theta)] \tag{11.7}$$

$$\boldsymbol{\beta} = [-\cos(\phi)\sin(\theta), -\sin(\phi)\sin(\theta), -\cos(\theta)] \tag{11.8}$$

respectively, and its (bipolar) triangular pulse shape (cf. (D.6))

$$e^i(t) = \frac{2e_\mathrm{m}}{t_\mathrm{w}}\left[t\,\mathrm{H}(t) - 2\left(t - \frac{t_\mathrm{w}}{2}\right)\mathrm{H}\left(t - \frac{t_\mathrm{w}}{2}\right) + 2\left(t - \frac{3t_\mathrm{w}}{2}\right)\mathrm{H}\left(t - \frac{3t_\mathrm{w}}{2}\right) - (t - 2t_\mathrm{w})\,\mathrm{H}\,(t - 2t_\mathrm{w})\right] \tag{11.9}$$

as shown in Fig. 11.1. Its amplitude is taken as $e_\mathrm{m} = 1 \cdot 10^3\,[\mathrm{V/m}]$ and the zero-crossing time as $ct_\mathrm{w} = 1.0\,D/\sqrt{\epsilon_\mathrm{r}}$, where $c = c_0/\sqrt{\epsilon_\mathrm{r}}$. The reference FIT-based models are finely meshed such that the maximum mesh step is always less than $ct_\mathrm{w}/50$. The boundary condition on the surrounding box is set to 'open'. Two different plane-wave excitations will be considered (a) $\{\phi, \theta\} = \{\pi/2, \pi/4\}$ (PW 1); (b) $\{\phi, \theta\} = \{\pi/4, \pi/4\}$ (PW 2). The resulting

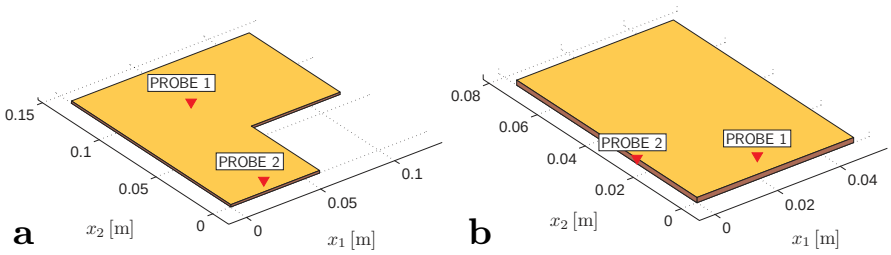

Figure 11.2: Computational models of the analyzed circuits with field probes (the solid triangles). (a) The irregularly-shaped circuit; (b) The rectangular circuit.

voltage responses are observed in the time window of observation $\{0 < ct \leq 10D/\sqrt{\epsilon_\mathrm{r}}\}$. In the following examples we take $\epsilon_\mathrm{r} = 4.50$, $D = 50.0\,[\mathrm{mm}]$ and $d = 1.50\,[\mathrm{mm}]$ is circuits' thickness.

11.2.1 An irregularly-shaped planar circuit

At first, the pulsed response of the irregularly-shaped circuit as shown in Fig. 11.2a is evaluated via Eq. (11.3). It is assumed that at $t = 0$ plane wave PW 1 hits the top edge $x_2 = 140\,[\mathrm{mm}]$, while PW 2 at that origin hits the top-left corner $\{x_1, x_2\} = \{120, 140\}\,[\mathrm{mm}]$. The pulsed voltage responses are observed at $\{x_1^S, x_2^S\} = \{50, 100\}\,[\mathrm{mm}]$ (PROBE 1) and $\{x_1^S, x_2^S\} = \{30, 10\}\,[\mathrm{mm}]$ (PROBE 2) (see Fig. 11.2a).

The corresponding results are shown in Figs. (11.3) and (11.4). As can be seen, the pulses evaluated via Eq. (11.3) agree very well with the FIT-based ones. The observable discrepancies may be dominantly attributed to different strategies in modeling the circuit's boundary conditions. While the TD-CIM-based model assumes the perfect magnetic wall along $\partial\Omega^R$, the three-dimensional FIT model has the 'open boundary' accounting for the fringing fields.

11.2.2 A rectangular planar circuit

The pulsed voltage response of a rectangular circuit $\Omega = \{0 < x_1 < L, 0 < x_2 < W\}$ of dimensions $\{L, W\} = \{50, 75\}\,[\mathrm{mm}]$ (see Fig. 11.2b) is evaluated with the help of (11.4) and (5.7) with (5.16). In this example, we assume conductive losses incorporated in the dielectric relaxation function according to Eq. (5.14) with $\sigma = 0.02\,[\mathrm{S/m}]$. The pulsed voltage responses are evaluated at two observation points $\{x_1^S, x_2^S\} = \{L/2, W/10\}$ (PROBE 1) and $\{x_1^S, x_2^S\} = \{0, W/3\}$ (PROBE 2) (see Fig. 11.2b.). It is assumed that at

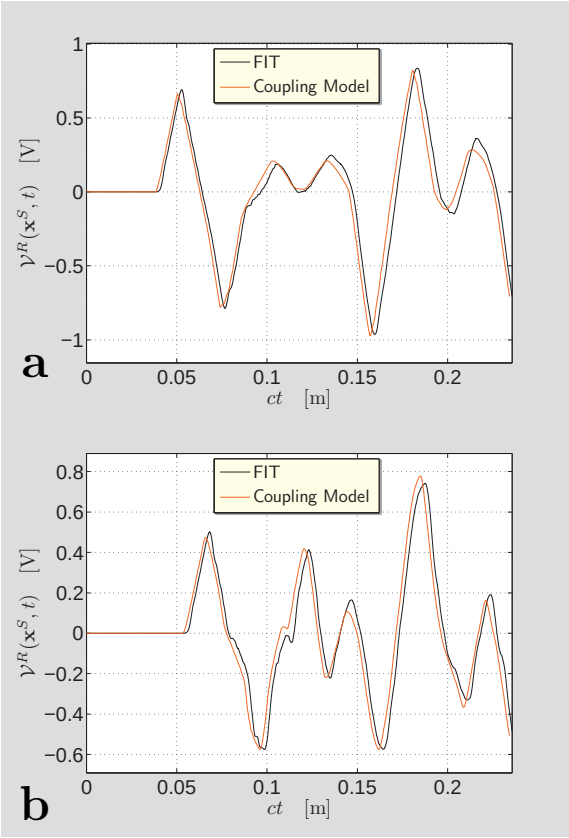

Figure 11.3: The pulsed voltage evaluated using the proposed coupling model and the referential FIT as observed at PROBE 1 of the irregularly-shaped circuit due to the plane wave (a) $\{\phi, \theta\} = \{\pi/2, \pi/4\}$ (PW 1); (b) $\{\phi, \theta\} = \{\pi/4, \pi/4\}$ (PW 2). From [111], adapted with permission from Taylor & Francis, © 2016 Taylor & Francis.

$t = 0$ plane wave PW 1 hits the top edge $x_2 = 75\,[\text{mm}]$, while PW 2 at that origin hits the top-left corner $\{x_1, x_2\} = \{50, 75\}\,[\text{mm}]$.

The corresponding results are given in Figs. 11.5 and 11.6. Here, again, the differences with respect to the FIT-based results can be mainly attributed to the different boundary conditions imposed along the circuit periphery $\partial\Omega^R$. In this respect, it is interesting to interpret the discrepancies in the early part of the response in Fig. 11.6a. Owing to the fact that the incident magnetic-field vector is perpendicular to the tangential vector $\boldsymbol{\tau}$ of the circuit's edges along $x_1 = 0$ and $x_1 = L$, these edges, where also PROBE 2 is located, do not contribute to the response (cf. Eq. (11.4)). On the other hand, with the FIT-based 'open-boundary model', also the neighborhood of the observation

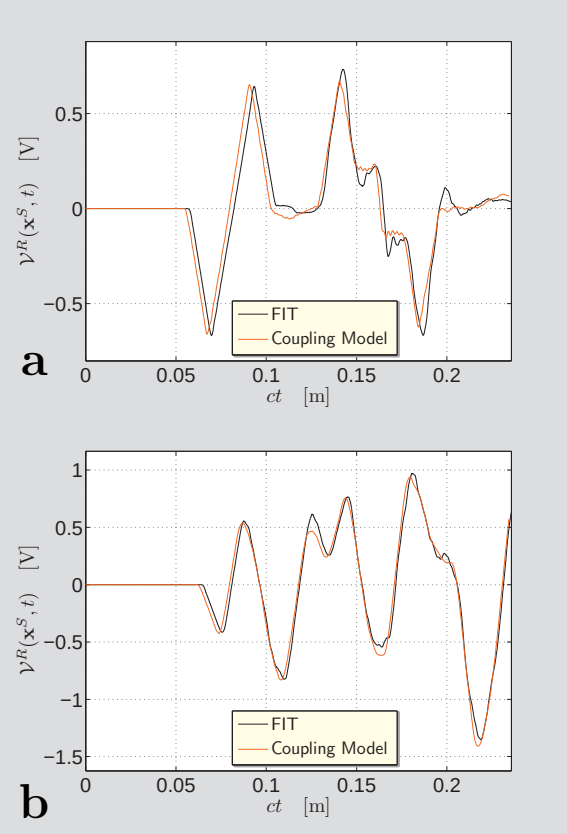

Figure 11.4: The pulsed voltage evaluated using the proposed coupling model and the referential FIT as observed at PROBE 2 of the irregularly-shaped circuit due to the plane wave (a) $\{\phi, \theta\} = \{\pi/2, \pi/4\}$ (PW 1); (b) $\{\phi, \theta\} = \{\pi/4, \pi/4\}$ (PW 2). From [111], adapted with permission from Taylor & Francis, © 2016 Taylor & Francis.

probe yields the (relatively weak) contribution with its arrival time at about $cT_{\text{arr}} = (2W/3)\sin(\pi/4)/\sqrt{\epsilon_{\text{r}}} \simeq 0.0167\,[\text{m}]$. The latter contribution observed at PROBE 2 obviously manifests itself earlier than the contributions from the edges along $x_2 = \{0, W\}$ that form the response of the analytical coupling model.

As the last example, the time evolution of the pulsed voltage distribution is illustrated. To this end, the TD response to the second plane $\{\phi, \theta\} = \{\pi/4, \pi/4\}$ (PW 2) is evaluated for a set of field points on Ω^R. The results for the consecutive (scaled) observation times $ct = \{\sqrt{2}/30, \sqrt{2}/20, \sqrt{2}/15\}\,[\text{m}]$ are given in Fig. 11.7. Such analysis may help to localize 'hot spots' when assessing the vulnerability of PCBs to an external pulsed EM disturbance.

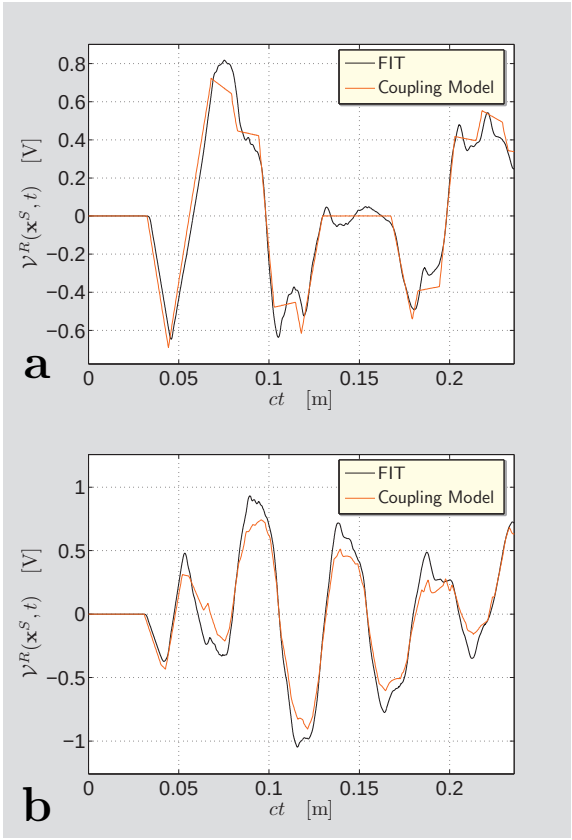

Figure 11.5: The pulsed voltage evaluated using the proposed coupling model and the referential FIT as observed at PROBE 1 of the rectangular circuit due to the plane wave (a) $\{\phi, \theta\} = \{\pi/2, \pi/4\}$ (PW 1); (b) $\{\phi, \theta\} = \{\pi/4, \pi/4\}$ (PW 2). From [111], adapted with permission from Taylor & Francis, © 2016 Taylor & Francis.

Moreover, thanks to the fact that the pulsed voltage response has been expressed in the closed form whose evaluation is computationally very efficient, the result can find its application in solving optimization problems (e.g. [46]), which mostly necessitates (time-consuming) repeated calculations of the objective function.

11.3 Conclusions

The closed-form expressions for the efficient TD radiated susceptibility analysis of a planar circuit have been derived using the concept of reciprocity. From them it is immediately clear that a planar circuit can be in its receiving

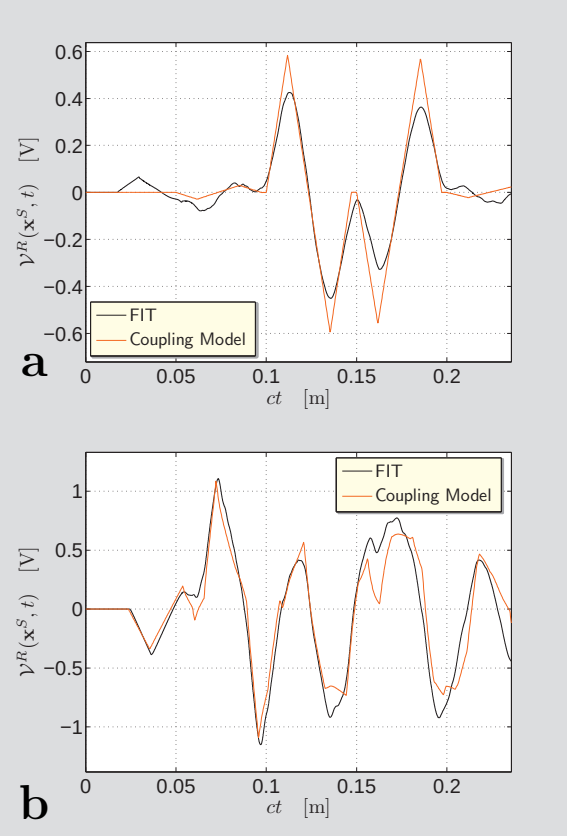

Figure 11.6: The pulsed voltage evaluated using the proposed coupling model and the referential FIT as observed at PROBE 2 of the rectangular circuit due to the plane wave (a) $\{\phi, \theta\} = \{\pi/2, \pi/4\}$ (PW 1); (b) $\{\phi, \theta\} = \{\pi/4, \pi/4\}$ (PW 2). From [111], adapted with permission from Taylor & Francis, © 2016 Taylor & Francis.

state viewed as to be excited along the circuit periphery via the tangential component of an incident magnetic field.

The derived relations express the pulsed voltage response of a planar structure to an impulsive EM plane wave via the one-dimensional contour integral. It has been demonstrated that the presented approach is well suited for its combination with TD-CIM and the relevant TD 'ray-type' Green's function representation. In addition to the high computational efficiency of the presented methodology, the derived TD integral representations provide physical insights into the dominant (space-time) EM-coupling mechanism of planar structures. All the derived integral representations have been validated using (three-dimensional) FIT.

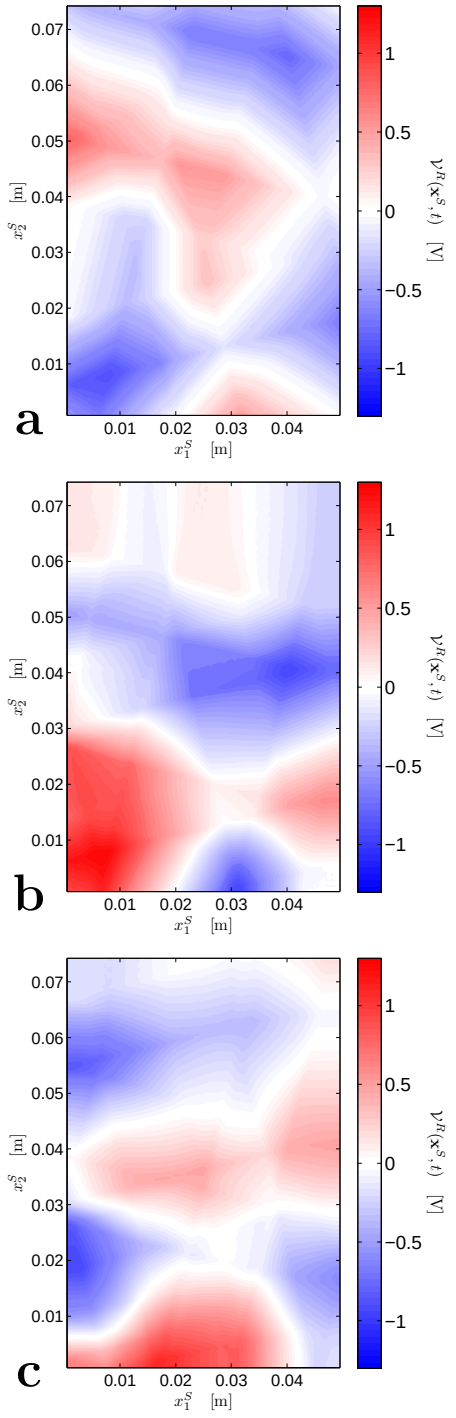

Figure 11.7: Time evolution of the voltage distribution at (a) $ct = \sqrt{2}/30$ [m]; (b) $ct = \sqrt{2}/20$ [m]; (c) $ct = \sqrt{2}/15$ [m]. From [111], adapted with permission from Taylor & Francis, © 2016 Taylor & Francis.

Appendix A

Integrals of the logarithmic function

The two-dimensional Green's function that appears in CIM shows the logarithmic singularity that must be integrated over a line segment of the boundary contour. On this account, let us consider the following integral

$$I = \int_{\boldsymbol{x}\in\Omega^{AB}} \ln[r(\boldsymbol{x}|\boldsymbol{x}^C)]\mathrm{d}l(\boldsymbol{x}) \tag{A.1}$$

where Ω^{AB} is the line segment determined by points A and B, $r(\boldsymbol{x}|\boldsymbol{x}^C)$ denotes the Eucledian distance between a point on Ω^{AB} and point C lying off the segment. The position of each pointis specified by the position vector $\boldsymbol{x}$ (see Sec. 1.2).

Upon introducing the parametrization for $\boldsymbol{x} \in \Omega^{AB}$

$$\boldsymbol{x} = \boldsymbol{x}^A + \lambda(\boldsymbol{x}^B - \boldsymbol{x}^A) \quad \text{for}\, \lambda \in (0,1) \tag{A.2}$$

we arrive at the one-dimensional integral that can be solved analytically. In this way we end up with

$$\begin{aligned} I = R^{CP}\Big\{ &\tan(\psi^{BC})\left[\ln(R^{BC}) - 1\right] \\ &- \tan(\psi^{AC})\left[\ln(R^{AC}) - 1\right] + \psi^{BC} - \psi^{AC}\Big\} \end{aligned} \tag{A.3}$$

where ψ^{AC} and ψ^{BC} are *oriented* angles between the perpendicular line from point C to segment Ω^{AB} and the lines of points C with A and C with B, respectively (see Fig. A.1).

If point C lies on the same line as points A and B then the integral is easily found via the limiting process. Note that for such a case the derivative

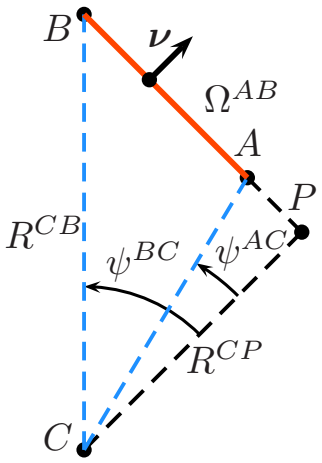

Figure A.1: Integration along the line segment.

of the logarithmic function along the direction parallel to the normal vector $\boldsymbol{\nu}$

$$\partial_\nu \ln[r(\boldsymbol{x}|\boldsymbol{x}^C)] = \boldsymbol{\nu} \cdot (\boldsymbol{x} - \boldsymbol{x}^C)/r^2(\boldsymbol{x}|\boldsymbol{x}^C) \tag{A.4}$$

is zero.

Appendix B

Implementation of TD-CIM

In this section, a demo implementation of TD-CIM in MATLAB® is described. For the sake of simplicity, we shall limit ourselves to the description of a code capable of analyzing an instantaneously-reacting planar circuit (see Chapter 3) that is activated by a simple vertical circular port whose singularity-free model is described in Sec. 2.1.4.

B.1 Geometry of the circuit pattern

At first, the circuit's contour in a plane must be defined. This can be done, for example, by giving two 1D arrays that specify the polygon's vertices in the (x_1, x_2)-plane with respect to the chosen origin. The corners of the circuit shown in Fig. B.1 can be arranged in the following way

```
x = [0 0.10 0.10 0];
y = [0 0 0.15 0.15];
```

along the x_1- and x_2-direction, respectively. Once the vertices are specified, the circuit rim is divided into `N` straight-line sections. As a rule of thumb, the maximum length of the sections should be shorter than a tenth of the spatial support of the excitation pulse. Nevertheless, it has been demonstrated that even when this rule is violated, it may well be that the results are accurate enough. The line segments and the dividing points are numbered in counterclockwise direction as illustrated in Fig. B.1b. The co-ordinates of the dividing nodes of the sample circuit from Fig. B.1a then read

```
X = [0 0.025 0.050 0.075 0.100 0.100 0.100 0.100 0.100 0.075 0.050
     0.050 0.050 0.025 0 0 0 0 0];
Y = [0 0 0 0 0 0.025 0.050 0.075 0.100 0.100 0.100 0.125 0.150
    0.150 0.150 0.120 0.090 0.060 0.030];
```

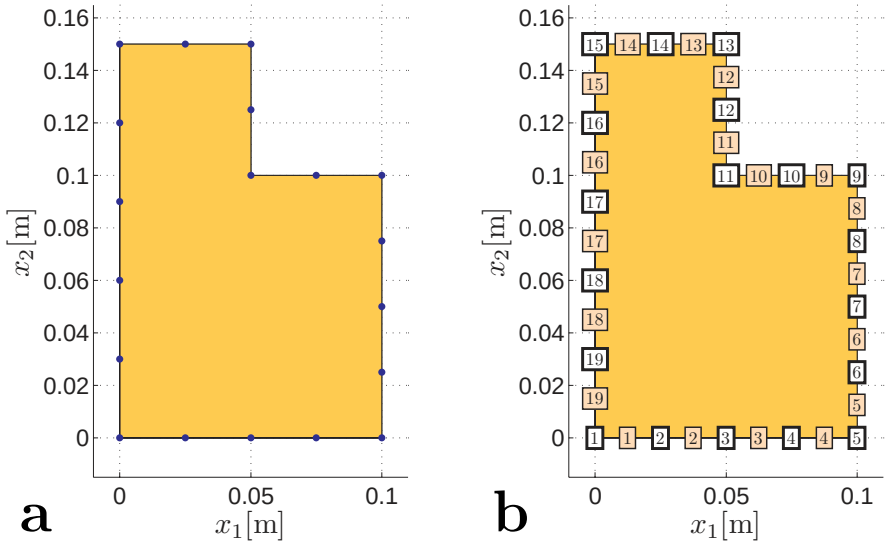

Figure B.1: The sample circuit pattern. (a) The dividing points along the circuit periphery; (b) the numbering of the line segments and the nodal points.

For possibly multiply connected circuit patterns, it is convenient to define an auxiliary variable, say `IND`, that assigns to each line segment the number of its bounding nodes. It is straightforward to find the elements of such a variable automatically for a general circuit geometry. Concerning the example from Fig. B.1, this information can be stored in the following way

```
IND.' =
[1 2 3 4 5 6 7 8 9 10 11 12 13 14 15 16 17 18 19;
 2 3 4 5 6 7 8 9 10 11 12 13 14 15 16 17 18 19 1]
```

Then, for example, `IND(19,1)` and `IND(19,2)` return `19` and `1`, respectively, which are the numbers of the discretization points bounding segment `19` (cf. Fig. B.1a). Furthermore, it is also useful to define another variable, say `SEG`, that assigns to each dividing node the number of its adjacent segments. For the sample circuit given in Fig. B.1 it may have the following form

```
SEG.' =
[19 1 2 3 4 5 6 7 8 9 10 11 12 13 14 15 16 17 18;
 1 2 3 4 5 6 7 8 9 10 11 12 13 14 15 16 17 18 19]
```

For instance, for the first node at the origin we get `SEG(1,1) = 19` and `SEG(1,2) = 1` (cf. Fig. B.1b). With the auxiliary variable at hand, we may further evaluate the sine and cosine functions of the angle that is found

between the tangent to the n-th line segment (recall the contour orientation) and the x_1-axis, i.e.

```
for n = 1 : N
 COSW(n) = (X(IND(n,2)) - X(IND(n,1)))/W(n);
 SINW(n) = (Y(IND(n,2)) - Y(IND(n,1)))/W(n);
end
```

where `W(n)` is length of the n-th segment. Regarding the sample geometry, this leads to

```
COSW = [1.0 1.0 1.0 1.0 0 0 0 0 -1.0 -1.0 0 0 -1.0 -1.0 0 0 0 0
    0];
```

for the array of segment's lengths (cf. Fig. B.1a)

```
W = [0.025 0.025 0.025 0.025 0.025 0.025 0.025 0.025 0.025 0.025
    0.025 0.025 0.025 0.025 0.030 0.030 0.030 0.030 0.030];
```

For example, `find(COSW == -1) = [9 10 13 14]` are then linked to the numbers of those line segments whose tangent vectors have the opposite orientation with respect to the x_1-axis (see Fig. B.1b). Arrays `COSW` and `SINW` will be used to evaluate $\cos(\theta)$ that appears in the elements of $\boldsymbol{Q}$ matrix (see Eq. (3.10)).

B.2 Numerical integration

Since evaluation of $\boldsymbol{Q}$ matrix and $\boldsymbol{F}$ vector requires computation of line integrals, it is convenient to specify the position on the k-th line segment in terms of parameter `lambda` whose values range from `0` to `1`, i.e.

```
XS = @(lambda,k) X(IND(k,1)) + lambda*(X(IND(k,2)) - X(IND(k,1)));
YS = @(lambda,k) Y(IND(k,1)) + lambda*(Y(IND(k,2)) - Y(IND(k,1)));
```

where we have used the concept of anonymous functions with two arguments `lambda` and `k`. In the implementation that follows, the former argument represents the abscissas of the Gauss-Legendre quadrature. Other numerical integration routines may serve the purpose as well. For example, we may use the 6-point quadrature [1, p. 921], i.e.

```
WINT.' = [0.0856622462 0.1803807865 0.2339569673 0.2339569673
    0.1803807865 0.0856622462];
LINT.' = [0.0337652429 0.1693953068 0.3806904070 0.6193095930
    0.8306046932 0.9662347571];
```

and define the following 6×6 matrices

```
NI = 6;
LINT1 = repmat(LINT,[1 NI]);
LINT2 = LINT1.';
```

These auxiliary vectors and matrices will be used in the following sections.

B.3 Computation of excitation vector $\boldsymbol{F}$

The simplified excitation model evaluates the elements of excitation vector $\boldsymbol{F}$ using Eq. (2.49). In this relation, the position of the excitation port is specified by the position vector $\boldsymbol{x}^C$. The probe must be placed inside the polygon specified by `x` and `y` arrays and hence we may take

```
XC = 0.10/4; YC = 0.15/4;
```

In the next step, the electric-current pulse shape is chosen. For example, let us implement the unipolar triangular pulse signature described by Eq. (5.24) (see Fig. 5.2). For such a choice, the relevant Laplace-transform inversion can be carried out analytically, viz

$$\mathcal{L}^{-1}[s\hat{I}(s)\mathrm{K}_0(sr/c)] = (2A/t_\mathrm{w})[\zeta(r,t) - 2\zeta(r,t-t_\mathrm{w}/2) + \zeta(r,t-t_\mathrm{w})] \quad \text{(B.1)}$$

where $\zeta(r,t)$ is defined as $\ln[ct/r + (c^2t^2/r^2 - 1)^{1/2}]\mathrm{H}(t-r/c)$. After creating the zero excitation vector

```
F = zeros(N,NT);
```

and defining the time axis, e.g.

```
cT = linspace(0, 3.0, NT);
```

in which `NT` is its length, the excitation vector's elements may be evaluated for each dividing node in a loop, viz

```
for m = 1 : N
    % ascending +
    R = sqrt((XC - XS(LINT,SEG(m,1))).^2 ...
          + (YC - YS(LINT,SEG(m,1))).^2);
    HLP = repmat(LINT,[1 NT]) .* ETA(R,cT);
    F(m,:) = F(m,:) - (mu/pi)*W(SEG(m,1))*WINT.'*HLP;
    % descending -
    R = sqrt((XC - XS(LINT,SEG(m,2))).^2 ...
          + (YC - YS(LINT,SEG(m,2))).^2);
    HLP = repmat(1-LINT,[1 NT]) .* ETA(R,cT);
```

```
    F(m,:) = F(m,:) - (mu/pi)*W(SEG(m,2))*WINT.'*HLP;
end
```

Apparently, the procedure consists of two similar parts depending whether we are 'testing' on the 'ascending' or on the 'descending' half of the triangular testing function $T^{[S]}(\boldsymbol{x}^T)$. The latter is here represented by `LINT` and by `1-LINT` in auxiliary variable `HLP`. Next, `R` is a `NI`×`1` 1D array that represents $r(\boldsymbol{x}^C|\boldsymbol{x}^T)$ (viz Eq. (2.48)), i.e. the array of the Eucledian distances from the circular excitation port to 'testing' points along the relevant line segment. Finally, `ETA(R,cT)` is a `NI`×`NT` 2D array that represents the space-time function given in Eq. (B.1) evaluated for each distance stored in `R` and each instant stored in `cT`. This can be most efficiently done using vectorization.

B.4 Computation of system matrix $\boldsymbol{Q}$

This section describes a simple implementation of the time-dependent system matrix $\boldsymbol{Q}$ whose elements will be next calculated according to Eq. (3.10). The demo implementation starts by initializing a zero 3D array, i.e.

```
Q = zeros(N,N,NT);
```

The matrix elements may be evaluated in two nested loops that each runs over all the dividing points. Similarly to the previous section, the calculation procedure can be divided into similar parts. Owing to the double integration in Eq. (3.10), we now have four similar blocks. For the sake of brevity, we closely describe only the part that refers to the case when both the 'testing' and 'expansion' take place on the 'ascending' halves of the triangular testing and expansion functions $T^{[S]}(\boldsymbol{x}^T)$ and $T^{[m]}(\boldsymbol{x}^T)$, respectively. Implementation of the remaining combinations is then straightforward. Hence, the procedure may run along the following lines

```
for m = 1 : N
    for n = 1 : N
      % ascending/ascending +/+
      if (m ~= n)
          R = sqrt((XS(LINT1,SEG(n,1)) - XS(LINT2,SEG(m,1))).^2 ...
            + (YS(LINT1,SEG(n,1)) - YS(LINT2,SEG(m,1))).^2);
          COS = ((XS(LINT1,SEG(n,1)) - XS(LINT2,SEG(m,1)))./R) ...
              * SINW(SEG(n,1)) ...
              - ((YS(LINT1,SEG(n,1)) - YS(LINT2,SEG(m,1)))./R) ...
              * COSW(SEG(n,1));
          HLP = repmat(LINT2.*LINT1.*COS,[1 1 NT]).*PSI(R,cT);
          Q(m,n,:) = squeeze(Q(m,n,:)) ...
```

```
                    + W(SEG(n,1))*W(SEG(m,1))*(1/pi/cdT) ...
                    *(reshape(WINT.'*HLP(:,:),[NI NT])).'*WINT;
        end
        %
        % + next similar blocks ...
        %
    end
end
```

in which `cdT` is the time step. In order to exclude the 'self-coupling' overlapping terms, it is noted that the matrix-element calculation is carried out in the relevant `if`-block. In contrast to the previous section, `R` is now a `NI`×`NI` 2D array that represents $r(\boldsymbol{x}|\boldsymbol{x}^T)$ (viz Eq. (3.10)), i.e. the array of the Eucledian distances from 'actual-field-expansion' points to 'testing-field' points along the relevant line segments. Variable `COS` calculated on the following line is, again, a `NI`×`NI` 2D array and represents a discrete form $\cos[\theta(\boldsymbol{x}|\boldsymbol{x}^T)]$ appearing in Eq. (3.10). The integrand of the latter equation is consequently stored in the auxiliary variable `HLP`. The latter is composed from the product of (the 'ascending' parts of) the expansion and testing spatial functions `LINT1` and `LINT2`, respectively, of 2D array `COS` and a `NI`×`NI`×`NT` 3D array named `PSI`. This 3D array is a representative of the space-time function $\Psi(r,t)$ (viz Eq. (3.12)) being evaluated for each distance from `R` and each instant from `cT`. Again, its evaluation is most efficiently done using vectorization.

B.5 Step-by-step updating procedure

With the excitation vector $\boldsymbol{F}$ and system matrix $\boldsymbol{Q}$ at our disposal, we may proceed with searching for the unknown field vector $\boldsymbol{E}$ by solving Eq. (3.8) in a step-by-step manner. To this end, we begin with the three-diagonal square matrix $\boldsymbol{I}$. Starting with its initialization, i.e.

```
I = zeros(N,N);
```

its filling can be done according to Eq. (3.9), viz

```
for m = 1 : N
    for n = 1 : N
        if (n == m)
            I(m,n) = (W(SEG(m,1)) + W(SEG(m,2)))/3;
        elseif (SEG(m,1) == SEG(n,2))
            I(m,n) = W(SEG(m,1))/6;
        elseif (SEG(m,2) == SEG(n,1))
            I(m,n) = W(SEG(m,2))/6;
```

```
        end
    end
end
```

After inverting the matrix on the left-hand side of Eq. (3.8), i.e.

```
M = inv(I - Q(:,:,2));
```

and initializing the N×NT 2D array allocated for the unknown field distribution

```
E = zeros(N,NT);
E(:,2) = M * F(:,2);
```

we may launch the step-by-step updating procedure. Its implementation may look as follows (cf. Eq. (3.8))

```
for p = 3 : NT
    SUM = zeros(N,1);
    for m = 3 : p
        SUM = SUM + Q(:,:,m) * E(:,p-m+2);
    end
    E(:,p) = M*(F(:,p) + SUM);
end
```

Once the procedure is terminated, E-array contains the desired electric-field (space-time) distribution at the dividing points along the circuit periphery and at time points along the time axis.

Appendix C

Implementation of FD-CIM

In this section, demo implementations of the classic FD-CIM in MATLAB® are described. The given description follows Chapter 4, where two CIM-based numerical procedures are derived from the complex-FD reciprocity relation (3.1).

Since the spatial aspects of the problem remain the same as in TD-CIM, the variables defined in Secs. B.1 and B.2 are applicable to the implementation of FD-CIM as well. The difference starts by defining the frequency axis `F` along which the resulting $\boldsymbol{U}$ and $\boldsymbol{H}$ matrices are evaluated. For the frequency range $\{50 \leq f = \omega/2\pi \leq 2000\}$ [MHz], this can be done as follows

```
F = linspace(50,2000,NF)*1e+6;
```

in which `NF` is the number of frequency points. The calculations are then carried out in a loop at each frequency point of `F` vector, i.e.

```
for k = 1 : NF
    om = 2*pi*F(k);
    t = sqrt(2/(om*mu0*sigma));
    k1 = om/c; k2 = (k1/2)*(tand + t/d);
    KWN = k1 - 1i*k2;
    % to be continued
end
```

in which `om` stands for the angular frequency ω, `sigma` is electrical conductivity σ of the plates, `t` is their skin depth, `tand` corresponds to $\tan(\delta)$ and finally `KWN` is the complex-valued wave number k (see Eq. (4.17)).

C.1 Computation of $\boldsymbol{U}$ and $\boldsymbol{H}$ matrices

In the first step, we allocate 2D arrays

```
U = zeros(N+NP,N+NP);
H = zeros(N+NP,N+NP);
```

that correspond to $\boldsymbol{U}$ and $\boldsymbol{H}$, respectively. As has been demonstrated in Chapter 4, computation of the elements of $\boldsymbol{U}$ and $\boldsymbol{H}$ matrices (see Eq. (4.3)) depends on the choice of the testing electric-current surface density $\partial\hat{J}_3^B$ used in the starting reciprocity relation (3.1). Accordingly, this section is divided in two parts.

C.1.1 Point-matching solution

In this section we evaluate the matrix elements according to Eq. (4.5)–(4.8). Having defined the wave number `KWN`, the elements of $\boldsymbol{U}$ and $\boldsymbol{H}$ can be evaluated as follows

```
for k = 1 : NF
    % ...
    % U-matrix and H-matrix
    for m = 1 : N+NP
      for n = 1 : N+NP
        R = sqrt((XS(0.5,m) - XS(0.5,n))^2 ...
              + (YS(0.5,m) - YS(0.5,n))^2);
        COS = ((XS(0.5,n) - XS(0.5,m))*SINW(n) ...
             - (YS(0.5,n) - YS(0.5,m))*COSW(n))/R;
        U(m,n) = -(KWN/2/1i)*COS*besselh(1,2,KWN*R)*W(n);
        H(m,n) = (om*mu0*d/2)*besselh(0,2,KWN*R);
      end
    end
    U(logical(eye(size(U)))) = 1;
    H(logical(eye(size(H)))) = (om*mu0*d/2)*(1-(2*1i/pi) ...
                              *(log(KWN*W/4) - 1 + GAMMA));
    % to be continued
end
```

where the nested loops run over the line segments. In them, `R` is the distance between the centers of the m-th and n-th segments and `XS`, `YS`, `W` with `SINW` and `COSW` have been specified in Secs. B.1 and B.2. The diagonal elements corresponding to the overlapping segments (`m = n`) are subsequently evaluated in line with Eqs. (4.7) and (4.8), where Euler's constant is represented by `GAMMA = 0.577215664901532`. Once $\boldsymbol{U}$ and $\boldsymbol{H}$ matrices are known, we can evaluate the impedance matrix $\boldsymbol{Z}$ and the input impedance corresponding to the excitation port, i.e.

```
for k = 1 : NF
    % ...
    % Z-matrix
    Z = U \ H;
    Z11(k) = sum(sum(Z(1:NP,1:NP)))/NP^2;
end
```

where the 'matrix-reduction approach' introduced in [115, Sec. III] is applied to obtain the input impedance `Z11` of a port consisting of `NP` uniformly-excited line segments.

C.1.2 Pulse-matching solution

The use of the rectangular-pulse testing current density results in the matrix elements specified in terms of the double integration taken along the actual and the testing line segments (see Eqs. (4.11) and (4.12)). These integrals are handled using the Gauss-Lengendre quadrature as described in Sec. B.2. Along these lines, the input impedance can be evaluated as follows

```
for k = 1 : NF
    om = 2*pi*F(k);
    t = sqrt(2/(om*mu0*sigma));
    k1 = om/c; k2 = (k1/2)*(tand + t/d);
    KWN = k1 - 1i*k2;
    % U-matrix and H-matrix
    for m = 1 : N+NP
      for n = 1 : N+NP
        R = sqrt((XS(LINT1,n) - XS(LINT2,m)).^2 ...
          + (YS(LINT1,n) - YS(LINT2,m)).^2);
        COS = ((XS(LINT1,n) - XS(LINT2,m))./R)*SINW(n) ...
            - ((YS(LINT1,n) - YS(LINT2,m))./R)*COSW(n);
        U(m,n) = -(KWN/2/1i)*W(n)*WINT.' ...
                 *((COS.*besselh(1,2,KWN*R))*WINT);
        H(m,n) = (om*mu0*d/2) * WINT.'*(besselh(0,2,KWN*R)*WINT);
      end
    end
        U(logical(eye(size(U)))) = 1;
        H(logical(eye(size(H)))) = (om*mu0*d/2)*(1-(2*1i/pi)
                                   *(log(KWN*W/2) - 3/2 + GAMMA));
    % Z-matrix
    Z = U \ H;
    Z11(k) = sum(sum(Z(1:NP,1:NP)))/NP^2;
end
```

Here, `R` corresponds to $r[\boldsymbol{x}(\lambda)|\boldsymbol{x}^T(\lambda^T)]$ that appears in Eqs. (4.11) and (4.12), `COS` stands for $\cos\left\{\theta[\boldsymbol{x}(\lambda)|\boldsymbol{x}^T(\lambda^T)]\right\}$ and the diagonal terms are calculated via Eqs. (4.15) and (4.16). The final input impedance is at each frequency from 1D-array `F` calculated using the procedure from [115, Sec. III], again.

Appendix D

The bell-shaped pulse

In this section we derive the expression for the excitation pulse signature that is frequently used throughout the book. In general, a *unipolar* pulse can defined by its amplitude A, pulse time width $t_{\rm w}$, pulse rise time $t_{\rm r}$ and if applicable, by its pulse fall time $t_{\rm f}$. The pulse time width of the pulse $\mathcal{I}(t)$ is defined as

$$t_{\rm w} = \int_{t=0}^{\infty} \mathcal{I}(t){\rm d}t/A \tag{D.1}$$

and the pulse rise time is defined as the time instant where the pulse reaches its maximum $\mathcal{I}(t_{\rm r}) = A$. A detailed description of practical waveforms is given by Quak [80].

The *bell-shaped source signature* can be viewed as to be generated by the time convolution of the rectangular function and the triangular function. The basic building block is the rectangular function of the finite duration $\triangle t > 0$ that is defined as

$$\mathrm{R}(t, \triangle t) = \mathrm{H}(t) - \mathrm{H}(t - \triangle t) \tag{D.2}$$

where $\mathrm{H}(t)$ is the Heaviside function defined as

$$\mathrm{H}(t) = \begin{cases} 0 & \text{if } t < 0 \\ 1/2 & \text{if } t = 0 \\ 1 & \text{if } t > 0 \end{cases} \tag{D.3}$$

Consequently, the triangular function of the duration $\triangle t$ can be found from the time convolution of two rectangular functions, i.e.

$$\mathrm{T}(t, \triangle t) = \mathrm{R}(t, \triangle t/2) * \mathrm{R}(t, \triangle t/2) \tag{D.4}$$

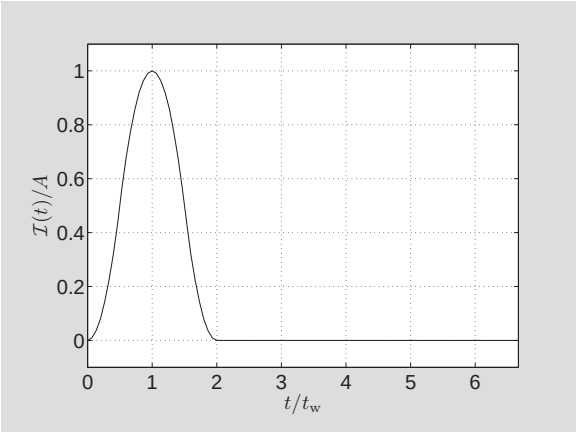

Figure D.1: Time signature of the bell-shaped pulse.

and finally, the bell-shaped function $\mathrm{B}(t, \triangle t)$ follows from the time convolution of the triangular function with the rectangular function, i.e.

$$\begin{aligned} \mathrm{B}(t, \triangle t) &= \mathrm{T}(t, \triangle t/2) * \mathrm{R}(t, \triangle t/2) \\ &= \mathrm{R}(t, \triangle t/4) * \mathrm{R}(t, \triangle t/4) * \mathrm{R}(t, \triangle t/2) \end{aligned} \tag{D.5}$$

In this manner, we may arrive at the electric current bell-shaped waveform

$$\begin{aligned} \mathcal{I}(t) = A \Bigg[& 2 \left(\frac{t}{t_{\mathrm{w}}} \right)^2 \mathrm{H}(t) - 4 \left(\frac{t}{t_{\mathrm{w}}} - \frac{1}{2} \right)^2 \mathrm{H} \left(\frac{t}{t_{\mathrm{w}}} - \frac{1}{2} \right) \\ & + 4 \left(\frac{t}{t_{\mathrm{w}}} - \frac{3}{2} \right)^2 \mathrm{H} \left(\frac{t}{t_{\mathrm{w}}} - \frac{3}{2} \right) - 2 \left(\frac{t}{t_{\mathrm{w}}} - 2 \right)^2 \mathrm{H} \left(\frac{t}{t_{\mathrm{w}}} - 2 \right) \Bigg] \end{aligned} \tag{D.6}$$

that is for illustration shown in Fig. D.1. Obviously, the bell-shaped pulse is continuously differentiable, its rise time is equal to the pulse time width and has a finite support, which is suitable for modeling causal phenomena.

Appendix E

Expansion functions

In this section we describe expansion functions $\{T_{[k]}, B_{[k]}, Q_{[k]}\}(t)$ used in the main text for the temporal expansion of the unknown field quantity. To this end, let us consider a temporal function $U(t)$ that is approximated by a set of expansion functions $F_{[k]}(t)$ according to

$$U(t) \simeq \sum_{k=1}^{NT} c_{[k]} F_{[k]}(t) \tag{E.1}$$

where $c_{[k]}$ are coefficients and $F_{[k]}(t)$ can stand for $\{T_{[k]}, B_{[k]}, Q_{[k]}\}(t)$. All these expansion functions have a finite support extending over two time steps $\text{supp}(F_{[k]}) = 2\triangle t$, $\triangle t > 0$, they have value one at one of the discrete time points $F_{[k]}(k\triangle t) = 1$ and zero in the neighboring points $F_{[k]}[(k \pm 1)\triangle t] = 0$ and differ in their differentiability class.

E.1 Linear expansion functions

The linear expansion function (also called as triangular or hat function) can be described as

$$\begin{aligned} T_{[k]}(t) = \big[&(t - t_{k-1})\mathrm{H}(t - t_{k-1}) - 2(t - t_k)\mathrm{H}(t - t_k) \\ &+ (t - t_{k+1})\mathrm{H}(t - t_{k+1})\big]/\triangle t \end{aligned} \tag{E.2}$$

where $\mathrm{H}(t)$ is the Heaviside function (see Eq. (D.3)), $t_k = k\triangle t$ and $k = \{1, ..., NT\}$. The sequence of shifted linear expansion functions and their sum are shown in Fig. E.1. Upon taking the Laplace transform (see Eq. (1.2)) of Eq. (E.2) we arrive at

$$\hat{T}_{[k]}(s) = \big[\exp(-st_{k-1}) - 2\exp(-st_k) + \exp(-st_{k+1})\big]/s^2\triangle t \tag{E.3}$$

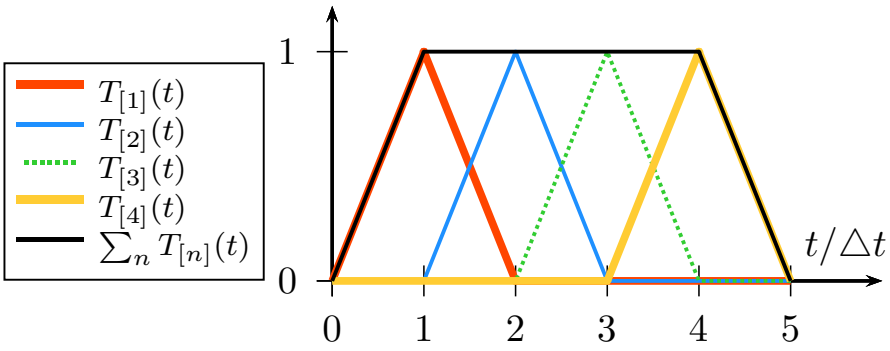

Figure E.1: Linear expansion functions.

A function expanded using the set of $\{T_{[k]}(t), k = 1, 2, ...\}$ is continuous but its first derivative shows jumps at a finite number of time instants, i.e. the function is of class C^0.

E.2 Quadratic expansion functions

The quadratic expansion function can be described as

$$B_{[k]}(t) = 2\big[(t - t_{k-1})^2 \mathrm{H}(t - t_{k-1}) - 2(t - t_{k-1/2})^2 \mathrm{H}(t - t_{k-1/2}) + 2(t - t_{k+1/2})^2 \mathrm{H}(t - t_{k+1/2}) - (t - t_{k+1})^2 \mathrm{H}(t - t_{k+1})\big]/(\triangle t)^2 \quad \text{(E.4)}$$

where $\mathrm{H}(t)$ is the Heaviside function (see Eq. D.3), $t_k = k\triangle t$ and $k = \{1, ..., NT\}$. The sequence of shifted quadratic expansion functions and their sum are shown in Fig. E.2. Upon taking the Laplace transform (see Eq. (1.2))

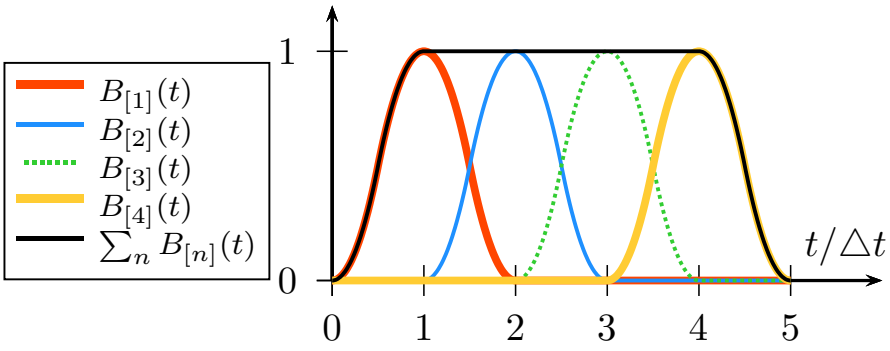

Figure E.2: Quadratic expansion functions.

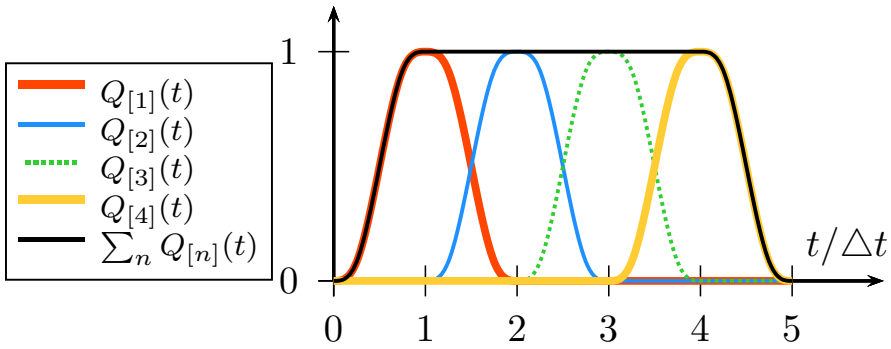

Figure E.3: Cubic expansion functions.

of Eq. (E.4) we arrive at

$$\hat{B}_{[k]}(s) = 4\big[\exp(-st_{k-1}) - 2\exp(-st_{k-1/2}) + 2\exp(-st_{k+1/2}) - \exp(-st_{k+1})\big]/s^3(\triangle t)^2 \quad \text{(E.5)}$$

A function expanded using the set of $\{B_{[k]}(t), k = 1, 2, ...\}$ is continuously differentiable, i.e. the function is of class C^1.

E.3 Cubic expansion functions

The cubic expansion function can be described as

$$\begin{aligned} Q_{[k]}(t) = 16\big[&(t-t_{k-1})^3\mathrm{H}(t-t_{k-1}) - 2(t-t_{k-3/4})^3\mathrm{H}(t-t_{k-3/4}) \\ &+2(t-t_{k-1/4})^3\mathrm{H}(t-t_{k-1/4}) - 2(t-t_k)^3\mathrm{H}(t-t_k) \\ &+2(t-t_{k+1/4})^3\mathrm{H}(t-t_{k+1/4}) - 2(t-t_{k+3/4})^3\mathrm{H}(t-t_{k+3/4}) \\ &+(t-t_{k+1})^3\mathrm{H}(t-t_{k+1})\big]/3(\triangle t)^3 \end{aligned} \quad \text{(E.6)}$$

where $\mathrm{H}(t)$ is the Heaviside function (see Eq. (D.3)), $t_k = k\triangle t$ and $k = \{1, ..., NT\}$. The sequence of shifted cubic expansion functions and their sum are shown in Fig. E.3. Upon taking the Laplace transform (see Eq. (1.2)) of Eq. (E.6) we arrive at

$$\begin{aligned} \hat{Q}_{[k]}(s) = 32\big[&\exp(-st_{k-1}) - 2\exp(-st_{k-3/4}) + 2\exp(-st_{k-1/4}) \\ &- 2\exp(-st_k) + 2\exp(-st_{k+1/4}) - 2\exp(-st_{k+3/4}) \\ &+ \exp(-st_{k+1})\big]/s^4(\triangle t)^3 \end{aligned} \quad \text{(E.7)}$$

A function expanded using the set of $\{Q_{[k]}(t), k = 1, 2, ...\}$ is continuous including its second derivative, i.e. the function is of class C^2.

Appendix F

Green's function of the dissipative scalar 2D wave equation

In this section we derive the causal solution $G_\infty = G_\infty(\boldsymbol{x}, t)$ of the two-dimensional dissipative wave equation

$$(\partial_1^2 + \partial_2^2)G_\infty - c^{-2}(\partial_t^2 + 2\alpha\partial_t)G_\infty = -\delta(\boldsymbol{x}, t) \tag{F.1}$$

with the zero-value initial conditions $G_\infty(\boldsymbol{x}, 0) = 0$ and $\partial_t G_\infty(\boldsymbol{x}, 0) = 0$ for all $\boldsymbol{x} \in \mathbb{R}^2$. Here, c is the wave speed (a positive and real-valued constant) and α is a real non-negative real constant accounting for conductive (diffusive) losses.

The dissipative wave equation (F.1) is solved with the aid of a modification of the Cagniard-DeHoop method [16]. To this end, the one-sided Laplace transformation (1.2) is combined with the dissipative-wave slowness field representation either along x_1- or x_2-direction. For the former direction we take

$$\hat{G}_\infty(x_1, x_2, s) = \frac{\hat{L}(s)}{2\pi\mathrm{i}} \int_{p=-\mathrm{i}\infty}^{\mathrm{i}\infty} \exp\left[-\hat{L}(s)px_1\right] \tilde{G}_\infty(p, x_2, s)\mathrm{d}p \tag{F.2}$$

where $\hat{L}(s) = [s(s + 2\alpha)]^{1/2}$ and ∂_1 is transformed to $\tilde{\partial}_1 = -\hat{L}(s)p$. The square-root expression shows two algebraic branch points at $s = \{-2\alpha, 0\}$ in the complex s-plane. The corresponding branch cuts are chosen such that $\mathrm{Re}(s^{1/2}) > 0$ and $\mathrm{Re}[(s + 2\alpha)^{1/2}] > 0$ for all $s \in \mathbb{C}$, which introduces two overlapping branch cuts running along the negative real axis $\{s \in \mathbb{C}; -\infty < \mathrm{Re}(s) < 0, \mathrm{Im}(s) = 0\}$ and $\{s \in \mathbb{C}; -\infty < \mathrm{Re}(s) < -2\alpha, \mathrm{Im}(s) = 0\}$, respectively. The choice of the branch cuts then implies an asymptotic expansion $\hat{L}(s) = s + \mathcal{O}(1)$ as $|s| \to \infty$.

Owing to the slowness representation (F.2) the transform-domain dissipative wave equation transforms to

$$\partial_2^2 \tilde{G}_\infty - \hat{L}^2(s)\gamma^2(p)\tilde{G}_\infty = -\delta(x_2) \tag{F.3}$$

where $\gamma(p)$ is the propagation coefficient

$$\gamma(p) = (1/c^2 - p^2)^{1/2} \quad \text{with} \quad \mathrm{Re}(.)^{1/2} > 0 \tag{F.4}$$

The bounded transform-domain solution of (F.3) is then substituted in (F.2), which finally yields

$$\hat{G}_\infty(x_1, x_2, s) = \frac{1}{2\pi\mathrm{i}} \int_{p=-\mathrm{i}\infty}^{\mathrm{i}\infty} \exp\left\{-\hat{L}(s)\left[px_1 + \gamma(p)|x_2|\right]\right\} \frac{\mathrm{d}p}{2\gamma(p)} \tag{F.5}$$

A few next steps follow the classical procedure of the Cagniard-DeHoop method. The original contour in the complex p-plane is deformed into the Cagniard-DeHoop contour defined as

$$px_1 + \gamma(p)|x_2| = \tau \tag{F.6}$$

where $\{\tau \in \mathbb{R}; r/c \leq \tau < \infty\}$ and $r = (x_1^2 + x_2^2)^{1/2} > 0$. The deformation is admissible by virtue of Cauchy's theorem and Jordan's lemma. After the mapping of the variable of integration from the complex p-plane to the real τ-axis we find

$$\hat{G}_\infty(x_1, x_2, s) = \frac{1}{2\pi} \int_{\tau=r/c}^{\infty} \exp\left[-\hat{L}(s)\tau\right] \frac{\mathrm{d}\tau}{(\tau^2 - r^2/c^2)^{1/2}} \tag{F.7}$$

Note that Eq. (F.7) formally resembles the result of the standard Cagniard-DeHoop method [16, Eq. (2.18)] for the loss-free wave motion when $\hat{L}(s)$ is equal to s. Now, however, we use [1, (29.3.96)] and Eq. (F.7) is transformed into TD

$$\begin{aligned} G_\infty(x_1, x_2, t) = (\alpha/2\pi) &\int_{\tau=r/c}^{t} \tau \mathrm{I}_1\left[\alpha(t^2 - \tau^2)^{1/2}\right] \exp(-\alpha t) \\ &(t^2 - \tau^2)^{-1/2}(\tau^2 - r^2/c^2)^{-1/2}\mathrm{d}\tau \\ &+ (1/2\pi)(t^2 - r^2/c^2)^{-1/2}\mathrm{H}(t - r/c)\exp(-\alpha t) \end{aligned} \tag{F.8}$$

where $\mathrm{I}_1(.)$ is the modified Bessel function of the first kind and the first order. Note that the integral in Eq. (F.8) shows the inverse square-root singularities in the both upper and lower limits of the integration that can be extracted through the following substitution

$$\tau^2 = (r/c)^2 \cos(\psi) + t^2 \sin^2(\psi) \quad \text{for} \quad 0 \leq \psi \leq \pi/2 \tag{F.9}$$

With the aid of Eq. (F.9) we then arrive at

$$G_\infty(x_1, x_2, t) = (\alpha/2\pi)\exp(-\alpha t)\mathrm{H}(t - r/c) \int_{\psi=0}^{\pi/2} \mathrm{I}_1\left[\alpha(t^2 - r^2/c^2)^{1/2}\cos(\psi)\right] \mathrm{d}\psi + (1/2\pi)(t^2 - r^2/c^2)^{-1/2}\mathrm{H}(t - r/c)\exp(-\alpha t) \tag{F.10}$$

The integral in (F.10) can be carried out in closed form, viz

$$\int_{\psi=0}^{\pi/2} \mathrm{I}_1\left[\beta\cos(\psi)\right] \mathrm{d}\psi = 2\sinh^2(\beta/2)/\beta \tag{F.11}$$

with $\{\beta \in \mathbb{R}; \beta > 0\}$, which finally leads to

$$G_\infty(x_1, x_2, t) = (1/2\pi)(t^2 - r^2/c^2)^{-1/2}\mathrm{H}(t - r/c) \left\{1 + 2\sinh^2[(\alpha/2)(t^2 - r^2/c^2)^{1/2}]\right\}\exp(-\alpha t) \tag{F.12}$$

An alternative way to obtain (F.12) is to start with the corresponding three-dimensional solution [20, Sec. 26.5] and apply Hadamard's method of descent [13, III - §4.4].

Appendix G

Numerical inversion of the Laplace transformation

In order to account for relaxation behavior of planar circuits, a numerical inversion of the Laplace transformation is employed in the main text. This inversion is based on the Bromwich integral

$$f(t) = \frac{1}{2\pi \mathrm{i}} \int_{s \in \mathcal{B}} \exp(st) \hat{F}(s) \mathrm{d}s \tag{G.1}$$

for $t > 0$, where $\mathcal{B}$ is the Bromwich integration contour that runs to the right of all singularities of $\hat{F}(s)$. The Bromwich integration contour may be deformed into an equivalent contour $\Gamma \cup \Gamma^*$ (* denotes complex conjugate) provided that $|\hat{F}(s)| \to 0$ in $\mathrm{Re}(s) < 0$ as $|s| \to \infty$ and a new integration contour encloses all singularities of $\hat{F}(s)$ in view of Jordan's lemma and Cauchy's theorem, respectively. A promising candidate is the hyperbolic integration contour defined according to

$$\Gamma = \{s(v) = \sigma_0 - \sigma \cosh(v) + \mathrm{i}\nu \sinh(v)\} \tag{G.2}$$

for $\{v \in \mathbb{R}; 0 \leq v \leq v_\infty\}$, where $\sigma_0 \in \mathbb{R}$, $\{\sigma, \nu \in \mathbb{R}; \sigma > 0, \nu > 0\}$, $v_\infty = \mathrm{acosh}[(\sigma_0 + \sigma_\infty)/\sigma]$ with $\mathrm{Re}[s(v_\infty)] = -\sigma_\infty$. Upon combining the upper and lower integration contours we arrive at

$$f(t) = \frac{1}{\pi} \mathrm{Im} \int_{v=0}^{v_\infty} \exp[s(v)t] \hat{F}[s(v)] \frac{\mathrm{d}s}{\mathrm{d}v} \mathrm{d}v \tag{G.3}$$

where the relevant Jacobian reads

$$\mathrm{d}s/\mathrm{d}v = -\sigma \sinh(v) + \mathrm{i}\nu \cosh(v) \tag{G.4}$$

An efficient way to solve (G.3) is the trapezoidal rule that leads to the following approximation

$$f(t) \simeq \frac{1}{\pi}\frac{v_\infty}{2N}\mathrm{Im}\left\{\hat{G}[s(0)] + 2\sum_{k=1}^{N-1}\hat{G}[s(v_k)] + \hat{G}[s(v_\infty)]\right\} \tag{G.5}$$

where

$$\hat{G}[s(v)] = \exp[s(v)t]\hat{F}[s(v)][\mathrm{d}s(v)/\mathrm{d}v] \tag{G.6}$$

and $v_k = kv_\infty/N$ for $k = \{0, ..., N\}$.

Appendix H

Green's function of the scalar 2D wave equation with relaxation

Consider the following wave equation

$$(\partial_1^2 + \partial_2^2)G_\infty - c^{-2}\partial_t^2(G_\infty + \chi * G_\infty) = -\delta(\boldsymbol{x}, t) \tag{H.1}$$

with the zero-value initial conditions $G_\infty(\boldsymbol{x}, 0) = 0$ and $\partial_t G_\infty(\boldsymbol{x}, 0) = 0$ for all $\boldsymbol{x} \in \mathbb{R}^2$. Here, c is the wave speed (a positive and real-valued constant) and $\chi = \chi(t)$ is the (causal) relaxation function, i.e. $\chi(t) = 0$ for all $t < 0$.

The wave equation (H.1) is solved with the aid of a modification of the Cagniard-DeHoop method [16]. To this end, the one-sided Laplace transformation (1.2) is combined with the dispersive-wave slowness field representation either along x_1- or x_2-direction. For the former direction we take

$$\hat{G}_\infty(x_1, x_2, s) = \left[s(1+\hat{\chi})^{1/2}\right]/2\pi\mathrm{i} \int_{p=-\mathrm{i}\infty}^{\mathrm{i}\infty} \exp\left[-s(1+\hat{\chi})^{1/2} p x_1\right] \tilde{G}_\infty(p, x_2, s)\mathrm{d}p \tag{H.2}$$

where $\hat{\chi} = \hat{\chi}(s)$ is real and positive for real and positive values of s and monotonically decreases toward zero as $s \to \infty$. As a consequence of the slowness representation, ∂_1 is transformed to $\tilde{\partial}_1 = -s(1+\hat{\chi})p$ and the transform-domain wave equation reads

$$\partial_2^2 \tilde{G}_\infty - s^2(1+\hat{\chi})\gamma^2(p)\tilde{G}_\infty = -\delta(x_2) \tag{H.3}$$

where $\gamma(p)$ is the propagation coefficient

$$\gamma(p) = (1/c^2 - p^2)^{1/2} \quad \text{with} \quad \mathrm{Re}(.)^{1/2} > 0 \tag{H.4}$$

The bounded transform-domain solution of (H.3) is then substituted in (H.2), which finally yields

$$\hat{G}_\infty(x_1, x_2, s) = (1/2\pi\mathrm{i}) \int_{p=-\mathrm{i}\infty}^{\mathrm{i}\infty} \exp\left\{-s(1+\hat{\chi})^{1/2}\left[px_1 + \gamma(p)|x_2|\right]\right\} \mathrm{d}p/2\gamma(p) \tag{H.5}$$

A few next steps follow the classical procedure of the Cagniard-DeHoop method. The original contour in the complex p-plane is deformed into the Cagniard-DeHoop contour defined as

$$px_1 + \gamma(p)|x_2| = \tau \tag{H.6}$$

where $\{\tau \in \mathbb{R}; r/c \leq \tau < \infty\}$ and $r = (x_1^2 + x_2^2)^{1/2} > 0$. The deformation is admissible by virtue of Cauchy's theorem and Jordan's lemma. After the mapping of the variable of integration from the complex p-plane to the real τ-axis we find

$$\hat{G}_\infty(x_1, x_2, s) = \frac{1}{2\pi} \int_{\tau=r/c}^{\infty} \exp\left[-s(1+\hat{\chi})^{1/2}\tau\right] \frac{\mathrm{d}\tau}{(\tau^2 - r^2/c^2)^{1/2}} \tag{H.7}$$

Note that up to this point, the described procedure is similar to the one for the dissipative wave equation from Appendix F. Now, however, we assume a general relaxation behavior, for which the exponential kernel does not have a closed form Laplace-transform inversion. For such a case we start with the Bromwich inversion integral and write

$$E(t, \tau) = \frac{1}{2\pi\mathrm{i}} \int_{s\in\mathcal{B}} \exp(st) \exp\left[-\hat{L}(s)\tau\right] \mathrm{d}s \tag{H.8}$$

where $\hat{L}(s) = s(1+\hat{\chi})^{1/2}$ as used in Appendix F and $\mathcal{B}$ is the Bromwich contour. The Bromwich contour is parallel with $\mathrm{Re}(s) = 0$ and is shifted to the right of all singularities in the complex s-plane. For standard relaxation models $\hat{L}(s)$ shows algebraic branch points due to square roots for which we choose $\mathrm{Re}[(.)^{1/2}] > 0$ for all $s \in \mathbb{C}$. This implies the (overlapping) branch cuts along the negative real axis in the complex s-plane. Then, the following asymptotic expansion holds

$$\hat{L}(s) = \hat{L}_\infty(s) + \mathcal{O}(s^{-1}) \tag{H.9}$$

as $|s| \to \infty$, where $\hat{L}_\infty(s) = s + \omega$, $\{\omega \in \mathbb{R}; \omega \geq 0\}$. In virtue of Jordan's lemma we therefore rewrite (H.8) as

$$\begin{aligned} E(t, \tau) = {} & \frac{1}{2\pi\mathrm{i}} \int_{s\in\mathcal{B}} \exp(st) \left\{\exp\left[-\hat{L}(s)\tau\right] - \exp\left[-\hat{L}_\infty(s)\tau\right]\right\} \mathrm{d}s \\ & + \frac{1}{2\pi\mathrm{i}} \int_{s\in\mathcal{B}} \exp(st) \exp\left[-\hat{L}_\infty(s)\tau\right] \mathrm{d}s \end{aligned} \tag{H.10}$$

Obviously, the second term in Eq. (H.10) represents the (attenuated) Dirac delta distribution

$$\frac{1}{2\pi\mathrm{i}}\int_{s\in\mathcal{B}}\exp(st)\exp\left[-\hat{L}_\infty(s)\tau\right]\mathrm{d}s=\delta(t-\tau)\exp(-\omega\tau) \tag{H.11}$$

while the first term can be handled numerically along the lines described in Appendix G. In this process, the Bromwich contour is for $t>\tau$ closed to the right by supplementing it with a semi-circle of radius $\Delta\to\infty$ and the resulting contour is in view of Cauchy's theorem contracted into the hyperbolic contour $\Gamma\cup\Gamma^*$ provided that all singularities are enclosed. Once the numerical integration is carried out, we arrive at

$$E(t,\tau)=F(t,\tau)\mathrm{H}(t-\tau)+\delta(t-\tau)\exp(-\omega\tau) \tag{H.12}$$

Upon substituting Eq. (H.12) into the TD counterpart of (H.7) we end up with

$$\begin{aligned}G_\infty(x_1,x_2,t)&=(1/2\pi)(t^2-r^2/c^2)^{-1/2}\mathrm{H}(t-r/c)\exp(-\omega t)\\&\quad+(1/2\pi)\int_{\tau=r/c}^{t}(\tau^2-r^2/c^2)^{-1/2}F(t,\tau)\mathrm{d}\tau\end{aligned} \tag{H.13}$$

where we have used the sifting property of the Dirac distribution. The first part in Eq. (H.13) is the (attenuated) fundamental solution of the two-dimensional wave equation, while the second one represents the effect of (Boltzmann-type) relaxation. The latter is negligible close to the wavefront as $t\downarrow r/c$, which is a general feature of dispersive phenomena [31]. Finally note that the dissipative wave equation solved in Appendix F is a special case of Eq. (H.1) for $\chi(t)=2\alpha\mathrm{H}(t)$.

Bibliography

[1] M. Abramowitz and I. A. Stegun. *Handbook of Mathematical Functions*. New York, NY: Dover Publications, 1972.

[2] R. Achar and M. S. Nakhla. Simulation of high-speed interconnects. *Proceedings IEEE*, 89(5):693–727, May 2001.

[3] G. Antonini. A low-frequency accurate cavity model for transient analysis of power-ground structures. *IEEE Transactions on Electromagnetic Compatibility*, 50(1):138–148, February 2008.

[4] C. A. Balanis. *Antenna Theory, 3rd Ed.* Hoboken, NJ: John Wiley & Sons, Inc., 2005.

[5] C. E. Baum. General properties of antennas. Sensor and Simulation Notes - Note 330, Philips Lab., Kirkland AFB, NM, July 1991.

[6] C. E. Baum. General properties of antennas. *IEEE Transactions on Electromagnetic Compatibility*, 44(1):18–24, February 2002.

[7] C. L. Bennett and W. L. Weeks. Transient scattering from conducting cylinders. *IEEE Transactions on Antennas and Propagation*, 18(5):627–633, September 1970.

[8] P. Bernardi and R. Cicchetti. Response of a planar microstrip line excited by an external electromagnetic field. *IEEE Transactions on Electromagnetic Compatibility*, 32(2):98–105, May 1990.

[9] M. Bonnet, G. Maier, and C. Polizzotto. Symmetric Galerkin boundary element method. *Applied Mechanics Reviews*, 51:669–704, 1998.

[10] A. C. Cangellaris and R. Lee. Finite element analysis of electromagnetic scattering from inhomogeneous cylinders at oblique incidence. *IEEE Transactions on Antennas and Propagation*, 39(5):645–650, May 1991.

[11] M.-C. F. Chang, V. P. Roychowdhury, L. Zhang, H. Shin, and Y. Qian. RF/Wireless for inter- and intra-chip communications. *Proceedings IEEE*, 89(4):456–466, April 2001.

[12] R. E. Collin. *Antennas and Radiowave Propagation*. New York, NY: McGraw-Hill, 1985.

[13] R. Courant and D. Hilbert. *Methods of Mathematical Physics*, volume 2. New York, NY: John Wiley & Sons, 1966.

[14] T. A. Cruse. A direct formulation and numerical solution of the general transient elastodynamic problem. (ii). *Journal of Mathematical Analysis and Applications*, 22:341–355, 1968.

[15] T. A. Cruse and F. J. Rizzo. A direct formulation and numerical solution of the general transient elastodynamic problem. (i). *Journal of Mathematical Analysis and Applications*, 22:244–259, 1968.

[16] A. T. de Hoop. A modification of Cagniard's method for solving seismic pulse problems. *Applied Scientific Research*, B(8):349–356, 1960.

[17] A. T. de Hoop. A reciprocity relation between the transmitting and the receiving properties of an antenna. *Applied Scientific Research*, 19(1):90–96, June 1968.

[18] A. T. de Hoop. Time-domain reciprocity theorems for electromagnetic fields in dispersive media. *Radio Science*, 22(7):1171–1178, December 1987.

[19] A. T. de Hoop. Reciprocity, discretization, and the numerical solution of direct and inverse electromagnetic radiation and scattering problems. *Proceedings IEEE*, 79(10):1421–1430, October 1991.

[20] A. T. de Hoop. *Handbook of Radiation and Scattering of Waves*. London, UK: Academic Press, 1995.

[21] A. T. de Hoop. Reflection and transmission of a transient, elastic line-source excited sh-wave by a planar, elastic bounding surface in a solid. *International Journal of Solids and Structures*, 39:5379–5391, 2002.

[22] A. T. de Hoop. A time-domain uniqueness theorem for electromagnetic wavefield modeling in dispersive, anisotropic media. *Radio Science Bulletin*, 305:17–21, June 2003.

[23] A. T. de Hoop and G. de Jong. Power reciprocity in antenna theory. *Proceedings of the Institution of Electrical Engineers*, 121(10):594–605, October 1974.

[24] A. T. de Hoop, I. E. Lager, and V. Tomassetti. The pulsed-field multiport antenna system reciprocity relation and its applications – a time-domain approach. *IEEE Transactions on Antennas and Propagation*, 57(3):594–605, March 2009.

[25] A. T. de Hoop, M. Stoopman, W. A. Serdijn, and I. E. Lager. Equivalent Thévenin and Norton Kirchhoff circuits of a receiving antenna. *IEEE Antennas and Wireless Propagation Letters*, 12:1627–1629, 2013.

[26] A. Deutsch, R. S. Krabbenhoft, K. L. Melde, C. W. Surovic, G. A. Katopis, G. V. Kopcsay, Z. Zhou, Z. Chen, Y. H. Kwark, T.-M. Winkel, X. Gu, and T. E. Standaert. Application of the short-pulse propagation technique for broadband characterization of PCB and other interconnect technologies. *IEEE Transactions on Electromagnetic Compatibility*, 52(2):266–287, May 2010.

[27] J. Dominguez. *Boundary Elements in Dynamics*. Southampton, UK: Computational Mechanics Publications, 1993.

[28] X. Duan, R. Rimolo-Donadio, H.-D. Brüns, and C. Schuster. A combined method for fast analysis of signal propagation, ground noise, and radiated emission of multilayer printed circuit boards. *IEEE Transactions on Electromagnetic Compatibility*, 52(2):487–495, May 2010.

[29] D. G. Duffy. *Transform Methods for Solving Partial Differential Equations*. Boca Raton, FL: Chapman & Hall/CRC, 2nd edition edition, 2004.

[30] M. A. Elmansouri and D. S. Filipovic. Pulse distortion and mitigation thereof in spiral antenna-based UWB communication systems. *IEEE Transactions on Antennas and Propagation*, 59(10):3863–3871, October 2011.

[31] L. B. Felsen. Propagation and diffraction of transient fields in nondispersive and dispersive media. In Felsen L. B., editor, *Transient Electromagnetic Fields*, chapter 1, pages 1–72. Berlin, Germany: Springer - Verlag, 1976.

[32] M. B. Friedman and R. Shaw. Diffraction of pulse by cylindrical obstacles of arbitrary cross section. *Journal of Applied Mechanics*, 29:40–46, 1962.

[33] F. Gardiol. Open question to time-domain experts. *IEEE Antennas and Propagation Society Newsletter*, 31(4):48, October 1988.

[34] R. Garg, P. Bhartia, I. Bahl, and A. Ittipiboon. *Microstrip Antenna Design Handbook*. Norwood, MA: Artech House, 2001.

[35] K. C. Gupta. Multiport network approach for modelling and analysis of microstrip patch antennas and arrays. In J. R. James and P. S. Hall, editors, *Handbook of Microstrip Antennas*, volume 28 of *IEE Electromagnetic Waves*. Peter Peregrinus Ltd., 1989.

[36] R. F. Harrington. *Field Computation by Method of Moments*. Piscataway, NJ: IEEE Press, 2003.

[37] R. F. Harrington, K. Pontoppidan, P. Abrahamsen, and N. C. Albertsen. Computation of Laplacian potentials by an equivalent source method. *Proceedings IEEE*, 116(10):1715–1720, October 1969.

[38] J. D. Hoffman. *Numerical Methods for Engineers and Scientists*. New York, NY: Marcel Dekker, 2001.

[39] A. Ishimaru. *Electromagnetic Wave Propagation, Radiation and Scattering*. Englewood Cliffs, NJ: Prentice-Hall, Inc., 1991.

[40] D. R. Jackson, W. F. Richards, and A. Ali-Khan. Input impedance and mutual coupling of rectangular microstrip antennas. 37(3):269–274, March 1989.

[41] M. A. Jaswon. Integral equation methods in potential theory. (i). *Proceedings of the Royal Society of London*, 275:23–32, January 1963.

[42] M. Y. Koledintseva, J. L. Drewniak, D. J. Pommerenke, Orlandi A. Antonini, G., and K. N. Rozanov. Wide-band Lorentzian media in the FDTD algorithm. *IEEE Transactions on Electromagnetic Compatibility*, 47(2):392–399, May 2005.

[43] M. Koshiba and M. Suzuki. Application of the boundary-element method to waveguide discontinuities. *IEEE Transactions on Microwave Theory and Techniques*, 34(2):301–307, February 1986.

[44] I. E. Lager and A. T. de Hoop. Inter-chip and intra-chip pulsed signal transfer between transmitting and receiving loops in wireless interconnect configurations. In *Proc. 40th European Microwave Conference*, pages 577–580, Paris, France, September 2010.

[45] I. E. Lager, A. T. de Hoop, and T. Kikkawa. Pulsed-field wireless interconnects in digital integrated circuits – a time-domain signal transfer and electromagnetic emission analysis. In *Proc. 6th European Conference on Antennas and Propagation*, pages 1855–1859, Prague, The Czech Republic, March 2012.

[46] J.L. Lagos and F Fiori. Worst-case induced disturbances in digital and analog interchip interconnects by an external electromagnetic plane wave – part I: modeling and algorithm. *IEEE Transactions on Electromagnetic Compatibility*, 53(1):178–184, February 2011.

[47] G.-T. Lei. Examination, clarification, and optimization of the Greens function/z-matrix models and calculations for rectangular planar microwave circuits. *IEEE Transactions on Microwave Theory and Techniques*, 59(4):803–815, April 2011.

[48] G.-T. Lei, R. W. Techentin, and B. K. Gilbert. High-frequency characterization of power/ground-plane structures. *IEEE Transactions on Microwave Theory and Techniques*, 47(5):562–569, May 1999.

[49] M. Leone. The radiation of a rectangular power-bus structure at multiple cavity-mode resonances. *IEEE Transactions on Electromagnetic Compatibility*, 45(3):486–492, August 2003.

[50] M. Leone. Radiated susceptibility on the printed-circuit-board level: simulation and measurement. *IEEE Transactions on Electromagnetic Compatibility*, 47(3):471–478, August 2005.

[51] Y. T. Lo, D. Solomon, and W. F. Richards. Theory and experiment on microstrip antenna. *IEEE Transactions on Antennas and Propagation*, 27(2):137–145, March 1979.

[52] M. Malkomes. Mutual coupling between microstrip patch antennas. *Electronics Letters*, 18(12):520–522, June 1982.

[53] W. J. Mansur and C. A. Brebbia. Formulation of the boundary element method for transient problems governed by the scalar wave equation. *Applied Mathematical Modelling*, 6:307–311, August 1982.

[54] W. J. Mansur and C. A. Brebbia. Numerical implementation of the boundary element method for two dimensional transient scalar wave propagation problems. *Applied Mathematical Modelling*, 6:299–306, August 1982.

[55] R. Mittra and C. A. Klein. Stability and convergence of moment method solutions. In R. Mittra, editor, *Numerical and Asymptotic Techniques in Electromagnetics*. Berlin: Springer-Verlag, 1975.

[56] A. F. Molisch. Ultrawideband propagation channels – theory, measurement, and modeling. 54(5):1528–1545, September 2005.

[57] P. M. Morse and H. Feshbach. *Methods of Theoretical Physics, Part I.* McGraw-Hill, New York, 1953.

[58] P. M. Morse and H. Feshbach. *Methods of Theoretical Physics, Part II.* McGraw-Hill, New York, 1953.

[59] J. R. Mosig. Integral equation technique. In Itoh T., editor, *Numerical Techniques for Microwave and Millimeter-Wave Passive Structures*, chapter 3, pages 133–213. New York, NY: John Wiley & Sons, 1989.

[60] J. R. Mosig, R. C. Hall, and F. E. Gardiol. Numerical analysis of microstrip patch antennas. In J. R. James and P. S. Hall, editors, *Handbook of Microstrip Antennas*, volume 28 of *IEE Electromagnetic Waves*. Peter Peregrinus Ltd., 1989.

[61] T. Myioshi and S. Miyauchi. The design of planar circulators for wideband operation. *IEEE Transactions on Microwave Theory and Techniques*, 28(3):210–214, July 1977.

[62] T. Myioshi, S. Yamaguchi, and S. Goto. Ferrite planar circuits in microwave integrated circuits. *IEEE Transactions on Microwave Theory and Techniques*, 25(7):593–600, July 1977.

[63] E. H. Newman and D. Forrai. Scattering from a microstrip patch. *IEEE Transactions on Antennas and Propagation*, 35(3):245–251, March 1987.

[64] E. H. Newman, J. H. Richmond, and B. W. Kwan. Mutual impedance computation between microstrip antennas. *IEEE Transactions on Microwave Theory and Techniques*, 31(11):941–945, November 1983.

[65] J. Nitsch, S. V. Tkatchenko, and S. Potthast. Transient excitation of rectangular resonators through electrically small circular holes. *IEEE Transactions on Electromagnetic Compatibility*, 54(6):1252–1259, December 2012.

[66] Y. Niwa, S. Hirose, and M. Kitahara. Application of the boundary integral equation method to transient analysis of inclusions in a half space. *Wave Motion*, 8:77–91, January 1986.

[67] T. Okoshi. *Planar Circuits for Microwaves and Lightwaves*. Springer Series in Electrophysics. Berlin: Springer-Verlag, 1985.

[68] T. Okoshi and S. Kitazawa. Computer analysis of short-boundary planar circuits. *IEEE Transactions on Microwave Theory and Techniques*, 23(3):299–306, March 1975.

[69] T. Okoshi and T. Miyoshi. The planar circuit - an approach to microwave integrated circuitry. *IEEE Transactions on Microwave Theory and Techniques*, 20(4):887–892, April 1972.

[70] T. Okoshi, Y. Uehara, and T. Takeuchi. The segmentation method - an approach to the analysis of microwave planar circuits. *IEEE Transactions on Microwave Theory and Techniques*, 24(10):662–668, October 1976.

[71] J. C. Parker. Via coupling within parallel rectangular planes. *IEEE Transactions on Electromagnetic Compatibility*, 39(1):17–23, February 1997.

[72] C. A. Paul. *Introduction to Electromagnetic Compatibility*. New York, NY: John Wiley & Sons, Inc., 2nd edition edition, 2006.

[73] E. Penard and J.-P. Daniel. Mutual coupling between microstrip antennas. *Electronics Letters*, 18(14):605–607, July 1982.

[74] D. M. Pozar. Input impedance and mutual coupling of rectangular microstrip antennas. 30(6):1191–1196, November 1982.

[75] D. M. Pozar. Radiation and scattering from a microstrip patch on a uniaxial substrate. *IEEE Transactions on Antennas and Propagation*, 35(6):613–621, June 1987.

[76] D. M. Pozar. Closed-form approximations for link loss in a UWB radio system using small antennas. *IEEE Transactions on Antennas and Propagation*, 51(9):2346–2352, September 2003.

[77] D. M. Pozar. Waveform optimizations for ultrawideband radio systems. *IEEE Transactions on Antennas and Propagation*, 51(9):2335–2345, September 2003.

[78] D. M. Pozar. Scattered and absorbed powers in receiving antennas. *IEEE Antennas and Propagation Magazine*, 46(1):144–145, February 2004.

[79] A. J. Pray, N. V. Nair, and B. Shanker. Stability properties of the time domain electric field integral equation using a separable approximation for the convolution with the retarded potential. *IEEE Transactions on Antennas and Propagation*, 60(8):3772–3781, August 2012.

[80] D. Quak. Analysis of transient radiation of a (traveling) current pulse on a straight wire segment. In *Proc. 2001 IEEE EMC International Symposium*, pages 849–854, Montreal, Que., Canada, July 2001.

[81] P. J. Restle, A. E. Ruehli, S. G. Walker, and G Papadopoulos. Full-wave peec time-domain method for the modeling of on-chip interconnects. *IEEE Transactions on Computer-Aided Design of Integrated Circuits and Systems*, 20(7):877–886, July 2001.

[82] R. Rimolo-Donadio, X. Gu, Y. H. Kwark, M. B. Ritter, B. Archambeault, F. De Paulis, Y. Zhang, J. Fan, H.-D. Brüns, and C. Schuster. Physics-based via and trace models for efficient link simulation on multilayer structures up to 40 GHz. *IEEE Transactions on Microwave Theory and Techniques*, 57(8):2072–2083, August 2009.

[83] V. H. Rumsey. Reaction concept in electromagnetic theory. *Physical Review*, 94(6):1483–1491, June 1954.

[84] K. Sakai and M. Koshiba. Analysis of electromagnetic field distribution in tunnels by the boundary-element method. In *IEE Proceedings H, Microwaves, Antennas and Propagation*, volume 137, pages 202–208, August 1990.

[85] T. K. Sarkar and S. M. Rao. The application of the conjugate gradient method for the solution of electromagnetic scattering from arbitrarily oriented wire antennas. *IEEE Transactions on Antennas and Propagation*, 32(4):398–403, 1984.

[86] M. Schanz and H. Antes. Application of 'Operational Quadrature Methods' in time domain boundary element methods. *Meccanica*, 32:179–186, 1997.

[87] J. P. Schouten. A new theorem in operational calculus together with an application of it. *Physica*, 2:75–80, 1935.

[88] J. Shim, D. G. Kam, J. H. Kwon, and J. Kim. Circuital modeling and measurement of shielding effectiveness against oblique incident plane wave on apertures in multiple sides of rectangular enclosure. *IEEE Transactions on Electromagnetic Compatibility*, 52(3):566–577, August 2010.

[89] A. Shlivinski, E. Heyman, and R. Kastner. Antenna characterization in the time domain. *IEEE Transactions on Antennas and Propagation*, 45(7):1140–1149, July 1997.

[90] J. C. Slater. *Microwave Electronics*. New York, NY: D. Van Nostrand Company, Inc., 1950.

[91] J. R. Solin. Formula for the field excited in a rectangular cavity with a small aperture. *IEEE Transactions on Electromagnetic Compatibility*, 53(1):82–90, February 2011.

[92] J. A. Stratton. *Electromagnetic Theory*. McGraw-Hill, New York, 1941.

[93] G. T. Symm. Integral equation methods in potential theory. (ii). *Proceedings of the Royal Society of London*, 275:33–46, January 1963.

[94] C. T. Tai. A critical study of the circuit relations of two distant antennas. *IEEE Antennas and Propagation Magazine*, 44(6):32–37, December 2002.

[95] M. Tanaka and T. Matsumoto. Transient elastodynamic boundary element formulations based on the time-stepping scheme. *International Journal of Pressure Vessels and Piping*, 42:317–332, February 1990.

[96] M. Tanaka, H. Tsuboi, F. Kobayashi, and T Misaki. Transient eddy current analysis by the boundary element method using fourier transforms. *IEEE Transactions on Magnetics*, 29(2):1722–1725, March 1993.

[97] F. M. Tesche, M. V. Ianoz, and T. Karlsson. *EMC Analysis Methods and Computational Models*. New York, NY: John Wiley & Sons, Inc., 1997.

[98] A. G. Tijhuis. *Electromagnetic Inverse Profiling: Theory and Numerical Implementation*. Utrecht, the Netherlands: VNU Science Press, 1987.

[99] A. G. Tijhuis. Iterative techniques for the solution of integral equations in transient electromagnetic scattering. *Progress In Electromagnetics Research*, 5:455–538, 1991.

[100] J. Trinkle and A. Cantoni. Impedance expressions for unloaded and loaded power ground planes. *IEEE Transactions on Electromagnetic Compatibility*, 50(2):390–398, May 2008.

[101] B. Van der Pol. A theorem on electrical networks with an application to filters. *Physica*, 1:521–530, 1934.

[102] V. Vahrenholt and M. Leone. Efficient Foster-type macromodels for rectangular planar interconnections. *IEEE Transactions on Electromagnetic Compatibility*, 2(10):1686–1695, October 2012.

[103] J. G. van Bladel. *Electromagnetic Fields*. John Wiley & Sons, Hoboken, NJ, 2nd ed. edition, 2007.

[104] P. M. van den Berg. Iterative computational techniques in scattering based upon the integrated square error criterion. *IEEE Transactions on Antennas and Propagation*, 32(10):1063–1071, 1984.

[105] M. Štumpf. An application of the Cagniard-DeHoop technique for solving initial-boundary value problems in bounded regions. *The Quarterly Journal of Mechanics and Applied Mathematics*, 66(2):185–197, 2013.

[106] M. Štumpf. Pulsed EM field radiation, mutual coupling and reciprocity of thin planar antennas. *IEEE Transactions on Antennas and Propagation*, 62(8):3943–3950, August 2014.

[107] M. Štumpf. Time-domain analysis of rectangular power-ground structures with relaxation. *IEEE Transactions on Electromagnetic Compatibility*, 56(5):1095–1102, October 2014.

[108] M. Štumpf. The time-domain contour integral method – an approach to the analysis of double-plane circuits. *IEEE Transactions on Electromagnetic Compatibility*, 56(2):367–374, April 2014.

[109] M. Štumpf. Time-domain mutual coupling between power-ground structures. In *Proc. 2014 IEEE EMC International Symposium*, pages 240–243, Raleigh, North Carolina, August 2014.

[110] M. Štumpf. Analysis of dispersive power-ground structures using the time-domain contour integral method. *IEEE Transactions on Electromagnetic Compatibility*, 57(2):224–231, April 2015.

[111] M. Štumpf. The pulsed EM plane-wave response of a thin planar antenna. *Journal of Electromagnetic Waves and Applications*, 30(9):1133–1146, 2016.

[112] M. Štumpf. The equivalent Thévenin-network representation of a pulse-excited power-ground structure. *IEEE Transactions on Electromagnetic Compatibility*, 59(1):249–255, February 2017.

[113] M. Štumpf. Modeling of electromagnetic fields in parallel-plane structures: a unified contour-integral approach. *Radioengineering*, April 2017. [**invited**].

[114] M. Štumpf and I. E. Lager. The time-domain optical theorem in antenna theory. *IEEE Antennas and Wireless Propagation Letters*, 14:895–897, 2015.

[115] M. Štumpf and M. Leone. Efficient 2-D integral equation approach for the analysis of power bus structures with arbitrary shape. *IEEE Transactions on Electromagnetic Compatibility*, 51(1):38–45, February 2009.

[116] M. Štumpf and Z. Raida. Pulsed electromagnetic waves between parallel plates: the modal-expansion and generalized-ray approaches. *IEEE Antennas and Propagation Magazine*, 56(6):90–101, December 2014.

[117] J.-S. Wang and R. Mittra. Finite element analysis of MMIC structures and electronic packages using absorbing boundary conditions. *IEEE Transactions on Microwave Theory and Techniques*, 42(3):441–449, March 1994.

[118] T.-K. Wang, S.-T. Chen, C.-W. Tsai, S.-M. Wu, J. L. Drewniak, and T.-L. Wu. Modeling noise coupling between package and PCB power/-ground planes with an efficient 2-D FDTD/lumped element method. *IEEE Transactions on Advanced Packaging*, 30(4):864–871, November 2007.

[119] X.-C. Wei, E.-P. Li, E.-X. Liu, and X. Cui. Efficient modeling of rerouted return currents in multilayered power-ground planes by using integral equation. *IEEE Transactions on Electromagnetic Compatibility*, 50(3):740–743, August 2008.

[120] D. Wilton, S. Rao, A. Glisson, D. Schaubert, O. Al-Bundak, and C. Butler. Potential integrals for uniform and linear source distributions on polygonal and polyhedral domains. *IEEE Transactions on Antennas and Propagation*, 32(3):276–281, March 1984.

[121] E. Zauderer. *Partial Differential Equations of Applied Mathematics, 2nd Ed.* New York, NY: John Wiley & Sons, Inc., 1989.

Index